This project has received funding from the European Union's Horizon 2020 research and innovation programme under grant agreement No 871813.

ICT Project No 871813

MUNDFAB

Modeling Unconventional Nanoscaled Device FABrication

D2.6: Final version of the models for heated implants, SPER and silicidation

S. Mundinar (Fraunhofer), A. Johnsson (Fraunhofer), P. Pichler (Fraunhofer), A. La Magna (CNR-IMM), M. Italia (CNR-IMM), I. Deretzis (CNR-IMM), G. Calogero (CNR-IMM), P. Michałowski (L-IMIF), R. Daubriac (CNRS), P.L. Julliard (STM/CNRS), A. Hemeryck (CNRS), F. Cristiano (CNRS), R. Monflier (CNRS), A. Jay (CNRS), D. Rideau (STM), B. Sklénard (LETI), S. Kerdiles (LETI), M. Opprecht (LETI)

2023/07/10

Quality management

This deliverable was reviewed by:

Nicolas GUITARD, STM

Dominic WALDHOER, TUW

Contents

Abbreviations 3
Abstract 4
1 Introduction 4
2 Si and SiGe films doped with heated implantation 5
2.1 Measurements of ultra-shallow depth profiles with the SIMS technique 5
2.2 SRP Measurements of as-implanted samples for high temperature implantation processes 7
2.3 Additional characterization for P implantation 8
2.3.1 Characterization methods 8
2.3.2 Crystallinity of the initial layers 8
2.3.3 Phosphorus implantation at room temperature (P10) 10
2.3.4 Phosphorus implantation at 150 °C (P11) 11
2.3.5 Phosphorus implantation at 500 °C (P12) 12
2.4 Arsenic-implanted silicon 16
2.4.1 Hybrid KMC-continuum modelling 16
2.4.2 Interstitials cluster calibration 17
2.5 Boron-implanted silicon and silicon-germanium 20
2.5.1 Model for boron implantation 21
2.5.2 Silicon 22
2.5.3 Silicon germanium 27
2.6 Phosphorous-implanted silicon 29
2.6.1 Model for phosphorus implantation and diffusion 29
2.6.2 Comparison between measurements and simulation 30
3 SPER model in Sentaurus Process KMC 36
3.1 SPER in undoped SiGe alloys 36
3.2 SPER in doped SiGe alloys 37
4 Silicidation 37
4.1 Silicide structures and thermodynamic phase diagram of the Si-X system, where X=Ni/Pt 37
4.2 Modified Pott model for silicide formation 39

4.2.1 From single-phase to multi-phases Pott-like models: role of the stoichiometry 39
4.2.2 Reactive boundaries, diffusing atoms and intermixing 42
4.3 Calibration from the *ab-initio* energetics and simulation results 45
4.3.1 Blanket systems 52
4.3.2 Nanowire systems 55
Conclusions 58
References 59

Abbreviations

4PP	4-Point Probe
DL	Dislocation Loop
HE	Hall Effect
KMC	Kinetic Monte Carlo
LKMC	Lattice Kinetic Monte Carlo
RT	Room Temperature
SIMS	Secondary Ion Mass Spectrometry
SMIC	Small Interstitial Cluster
SPER	Solid Phase Epitaxy Regrowth
SRP	Spreading Resistance Profiling
TEM	Transmission Electron Microscopy
TRR	Time-Resolved Reflectivity

Abstract

In this deliverable the final versions of kinetic Monte Carlo (KMC) models for the simulation of heated implants, Solid Phase Epitaxy Regrowth (SPER) and silicidation are presented. Each of these topics is handled in a dedicated part, describing the models in detail, and presenting newly found results. For heated implants simulations for arsenic, boron, and phosphorous implantations are shown. For silicidation results for Si-Ni and Si-Pt structures are presented. Corresponding to the two strategies adopted in the MUNDFAB project, KMC models that rely on the Sentaurus TCAD commercial software are employed for simulation of heated implants, while the model for the simulation of silicidation is implemented in the open-source software package MulSKIPS.

1 Introduction

The three main topics of work package 2 (WP2) within the MUNDFAB project are the simulation of damage accumulation and dopant activation during heated implants, SPER of SiGe layers, and silicide formation. Continuum approaches are inherently not suited to consider atomistic concepts, and their computational costs increase drastically with the number of defect types that are taken into account. KMC approaches on the other hand are designed to consider infrequent movements of some atoms, corresponding to diffusion or reactions between surrounding atoms and defects. This means that KMC methods allow the simulation of individual dopant-defect configurations and their evolution with time. To be able to do this, it is required to know about the probabilities of the different possible reactions, and it is necessary to tune the respective parameters via careful calibration to achieve a sufficient predictivity of these models.

For the simulation of damage accumulation, amorphization, and diffusion during heated implantation and non-melt laser annealing an off-lattice KMC (or object KMC, in the following referred to by just KMC) approach is used, which is available in the Sentaurus Process TCAD commercial software [1, 2]. This module is coupled with the continuum simulator of Sentaurus Process, to perform mechanical steps in a continuum model, e.g., calculating the strain fields which then influence the atomistic event rates, and to convert the particles into continuum fields or vice versa (`KMC2PDE` and `PDE2KMC` tcl routines). Implemented defect categories are:

- Substitutional impurities like B, As and P
- Point defects (interstitial (I) and vacancy (V)) in neutral and charged states
- Impurity-point defect pairs in neutral and charged states, which drive the dopant diffusion
- Amorphous pockets (I_nV_m clusters)
- Impurity clusters in neutral or charged states (e.g., B_nI_m)
- Extended defects ({311}, {111}, dislocation loops (DLs) or voids)

To each of these objects predefined events are assigned, with a rate following an Arrhenius law:

$$\nu_{\text{event}} = \nu_0 \, \mathrm{e}^{-\beta E_a},$$

where ν_0 is the attempt frequency, E_a is the activation energy of the event and $\beta = 1/k_{\mathrm{B}}T$ is the inverse thermal energy. The first two are to be changed during the calibration procedure, usually based on experimental data and *ab initio* simulation results. For a more detailed

overview of the off-lattice KMC implementation in Sentaurus Process, we refer to D2.3 as well as the Sentaurus Process User Guide [1]. This approach is then used in Section 2 to develop theories for doping via heated implantation for Si and SiGe films as targets. New complementary measurements for heated implantations are shown. First, ultra-shallow B-profiles are investigated via the Secondary Ion Mass Spectrometry (SIMS) technique. Afterwards, Spreading Resistance Profiling (SRP) measurements of as-implanted B and P in Si films are discussed. Finally, additional characterization work for P implantation is shown, including, time-resolved reflectivity (TRR), transmission electron microscopy (TEM), and Hall effect (HE) measurements. Simulations for As, B and P are discussed, showing that for all three dopants additional calibration is necessary, since the AdvancedCalibration from Sentaurus KMC is not sufficient in the area of low temperature implants. The results of these newly calibrated models are also shown.

In section 3 the models for SPER that are available in Sentaurus Process KMC are reviewed for undoped and doped SiGe alloys.

However, Sentaurus Process does currently not include a model that enables the simulation of silicide growth. Therefore, instead of Sentaurus Process the open-source software package MulSKIPS is used to implement a model for silicidation, based on a lattice KMC (LKMC) approach. An in-depth discussion of the modified Pott model that is used for simulating silicidation can be found in Section 4. In addition, the model is calibrated using *ab-initio* energetics and the calibrated model is then applied to both blanket systems and nanowire systems.

At the end, we conclude our work giving a summary and an outlook for further work.

2 Si and SiGe films doped with heated implantation

The KMC modeling and calibration work presented in sections 2.5 and 2.6 was done in cooperation with Nikolas Zographos of Synopsys. The additional SIMS measurements presented in section 2.1 as well as the additional calibration of P implantation in section 2.3 were not complete at the submission of the experimental deliverable D2.4. The SRP measurements of as-implanted samples shown in section 2.2 were specifically requested as points of reference for the simulations. As a result, these measurements are placed within this deliverable.

2.1 Measurements of ultra-shallow depth profiles with the SIMS technique

SIMS is widely considered to be a well-suited technique to obtain a realistic distribution of dopants in semiconductor materials, particularly due to its excellent sensitivity [3, 4]. Explicitly, analyses of distributions of boron in silicon have been performed for more than forty years [5, 6, 7, 8, 9, 10]. However, the application of low implantation energies results in very shallow profiles which require improvement of the depth resolution of the SIMS methodology. This includes not only modification of the SIMS instruments (achieving lower impact energies of primary ions which increases the depth resolution) but also better algorithms used for raw data calibrations [11, 12].

Most of these protocols, however, operate under the assumption that the sputtering rate depends only on the type of material. Thus, the depth calibration can be performed individually for each layer. However, the experimental analysis has revealed that for ultra-low impact energy experiments the presence (or absence) of defects may have a significant impact on the sputtering rate. Since hot implantations may change the concentration of defects, a straightforward depth calibration would result in unrealistic compaction of the obtained profiles.

A significant challenge is that a standard SIMS measurement does not allow to monitor the distribution of defects inside a sample. However, the CAMECA IMS SC Ultra instrument used in these experiments is equipped with two completely separate primary columns for two different primary ions, namely oxygen, and cesium. While the former is typically used to monitor the boron distribution, the latter can be used to register the changes in the oxygen signal which is incorporated into the sample during the analysis of boron distribution. Both primary sources can be used interchangeably during the experiment and thus the changes in the oxygen signal can be in situ monitored. It is reasonable to assume that more oxygen is incorporated in the sample at higher defect concentrations and thus the oxygen signal provides qualitative information about the defect distribution in a sample. Assuming that the sputtering rate scales linearly with the defect distribution it is possible to perform a better depth calibration.

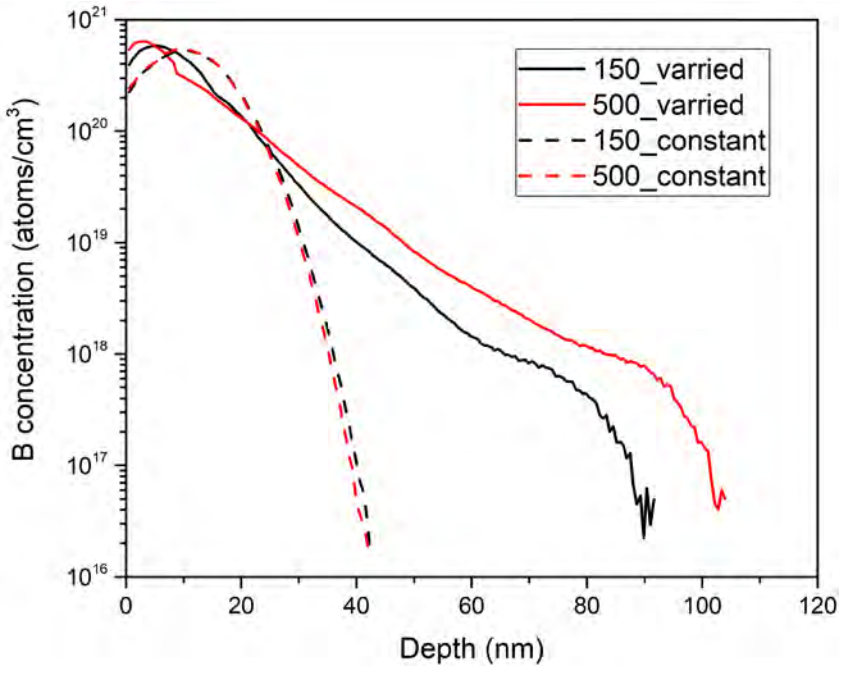

Figure 1: SIMS depth profiles of boron implanted at 150 °C and 500 °C substrate temperatures. Standard depth calibration with a constant sputtering rate (dashed lines) results in unrealistically compacted profiles, whereas a protocol that assumes varying sputtering rates (solid lines) recreates realistic distribution of boron dopant.

As presented in Fig. 1, standard calibration (constant sputtering rate) leads to compaction of hot implantation profiles, whereas the protocol with varied sputtering rate provides realistic distribution profiles.

2.2 SRP Measurements of as-implanted samples for high temperature implantation processes

Additional SRP measurements have been performed on samples implanted at high temperatures to characterize the “effective” activation as result of the thermal budget. We notice that the Spreading Resistance technique is based on resistance measurements calibrated with accurately prepared samples with controlled levels of “fully” activated dopants. Consequently, the distribution of dopant atoms in calibration samples could ideally be represented as well separated single (not-clustered) substitutional impurities embedded in the ideal lattice of the semiconductors.

Of course, this ideal scenario is barely achieved in as-implanted samples, since the emerging atomic structure in this case could be qualitatively described as a distribution of dopant atoms which only partially sit in substitutional positions and are embedded in a defective substrate where the implantation temperature should favor the increase of the substitutional component and the reduction of the damage. These considerations should justify the interpretation of the SRP measurements in as-implanted samples as “effective” local activation levels, where both substitutional impurity density and crystal damage (i.e., vacancies, interstitials, interstitial-impurities) are in some sense entangled in the measured level: SRP dopant densities will coincide with substitutional dopant densities only when the defectiveness has been substantially healed.

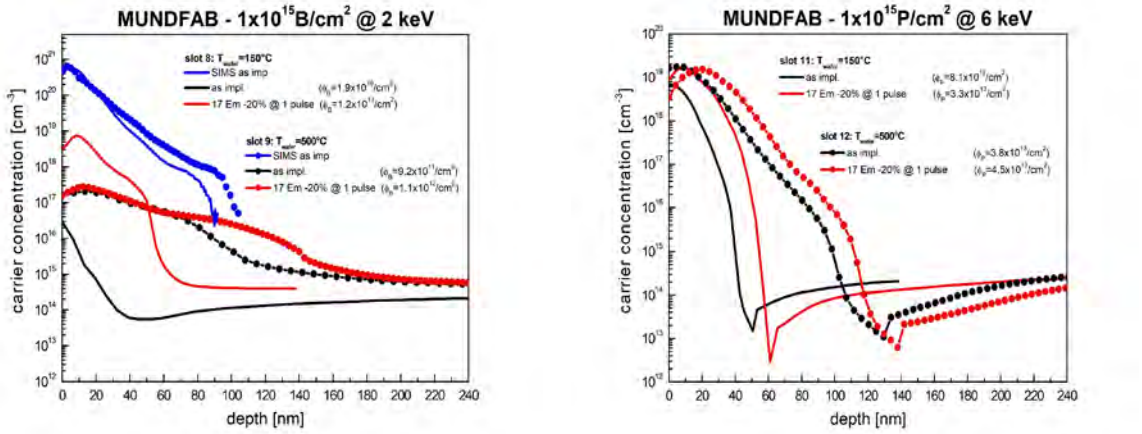

Figure 1: Comparison of as-implanted and laser annealed SRP profiles of (Left) B implanted samples (1x10^{15} cm^{-2} dose; 2 keV energy) compared with the laser annealed ones for the laser condition corresponding to the lowest pulsed thermal budged in the design of experiments (-20% fluence with respect to the melting threshold). Black dots (as-implanted) and red dots (annealed) are the profiles obtained for the 500 °C implantation case, while black line (as-implanted) and red line (annealed) are the profiles obtained for the 150 °C implantation case. (Right) same as before but of P implanted samples (1x10^{15} cm^{-2} dose; 6 keV energy). Black dots (as-implanted) and red dots (annealed) are the profiles obtained for the 500 °C implantation case, while black line (as-implanted) and red line (annealed) are the profiles obtained for the 150 °C implantation case. The blue line denotes the as-implanted SIMS profile at 150 °C, and the blue dots the as-implanted SIMS profile at 500 °C.

In Fig. 2 the SRP analyses of the B and P as-implanted samples in Si respectively are shown for the two different implantation temperatures. The effective active density is compared to the measurements of laser annealed ones for the laser condition corresponding to the lowest pulsed thermal budged in the design of experiments (-20% fluence with respect to the melting threshold).

The impact of the implantation temperature in the local effective activation level is clear in all the cases here presented where for the 500 °C implantation temperature the profiles are comparable to the laser annealed ones for both the B and P implantations. A strong difference is instead observed for the 150 °C implantation temperature between the B and P implanted profiles where the latter achieves a considerably larger active average level. In addition, we notice that a residual deactivation tail (common in the case of room temperature (RT) implantation) is present for the 150 °C B implant, while for all the P profiles the (process dependent) junction region can be individuated.

2.3 Additional characterization for P implantation

In this experiment, standard p-type silicon substrates were implanted with 6 keV phosphorus ions at a dose of $1x10^{15}$ cm^{-2} with various chuck temperatures: RT (P10), 150 °C (P11) and 500 °C (P12). Subsequent sub-melt laser anneals were performed to enhance the electrical properties of the implanted layers with a SCREEN-LT3100 system, equipped with a XeCl excimer laser (308 nm wavelength, ~145 ns FWHM pulse duration, 3% non-uniformity), while maintaining a constant flow of pure N_2 in the irradiated region (15x15 mm^2 areas). We chose four energy density conditions below the melt threshold for each wafer (Tab. 1). For each energy density, various pulse conditions were carried out: 1, 10, 100 and 1000 pulses, leading to a total of 16 laser conditions for each implanted wafer.

Table 1: Laser conditions performed on phosphorus-implanted wafers at RT (P10), 150 °C (P11) and 500 °C (P12). E_m denotes the melt threshold.

Energy density (J/cm^2)	P10	P11	P12
E_m	1.30	1.35	1.70
E1	**1.275** (E_m – 2%)	**1.325** (E_m – 2%)	**1.575** (E_m – 7.5%)
E2	**1.25** (E_m – 4%)	**1.275** (E_m – 5.5%)	**1.50** (E_m – 11.5%)
E3	**1.20** (E_m – 7.5%)	**1.25** (E_m – 7%)	**1.40** (E_m – 17.5%)
E4	**1.175** (E_m – 10%)	**1.225** (E_m – 9.5%)	**1.325** (E_m – 22%)

2.3.1 Characterization methods

Different characterization methods were used to study all the fabricated samples. The crystalline properties were investigated by TRR and TEM, by plan view and cross-section preparations. The surface morphology was examined by using haze measurements. Finally, the dopant activation and the electrical properties were measured by the 4-point probe (4PP) technique and by HE measurements, with different Van der Pauw structures (cross and squares). For Hall measurements analysis, the Hall scattering factor r_H will be considered equal to 0.95 for dopant concentrations around 10^{20} cm^{-3} [13].

2.3.2 Crystallinity of the initial layers

The initial crystalline quality of the as-implanted layers was deduced thanks to TRR measurements (equipped on the laser tool) and TEM observations on cross-section lamellas. While P10 cross-section TEM observation has been planned for the upcoming weeks, the first

priority for cross-section TEM observations was set for layers P11 and P12 as these two layers constitute the core of the study on heated implantations, for which the initial crystalline quality after the implantation process were not perfectly known. For the as-implanted P11 layer (Fig. 3 (a)), we observe a 17.5 nm continuous amorphous surface layer, with a slight roughness at amorphous/crystal interface, below which we can see a damaged area due to the implantation process (interstitials). For the as-implanted P12 layer (Fig. 3 (b)), the surface layer is crystalline thanks to the 500 °C thermal budget added during the implantation process. Around 15 nm below the surface, we notice a 5 nm width damaged band, which corresponds to the concentration peaks of phosphorus dopants and interstitials, which are close to each other, giving the implantation conditions.

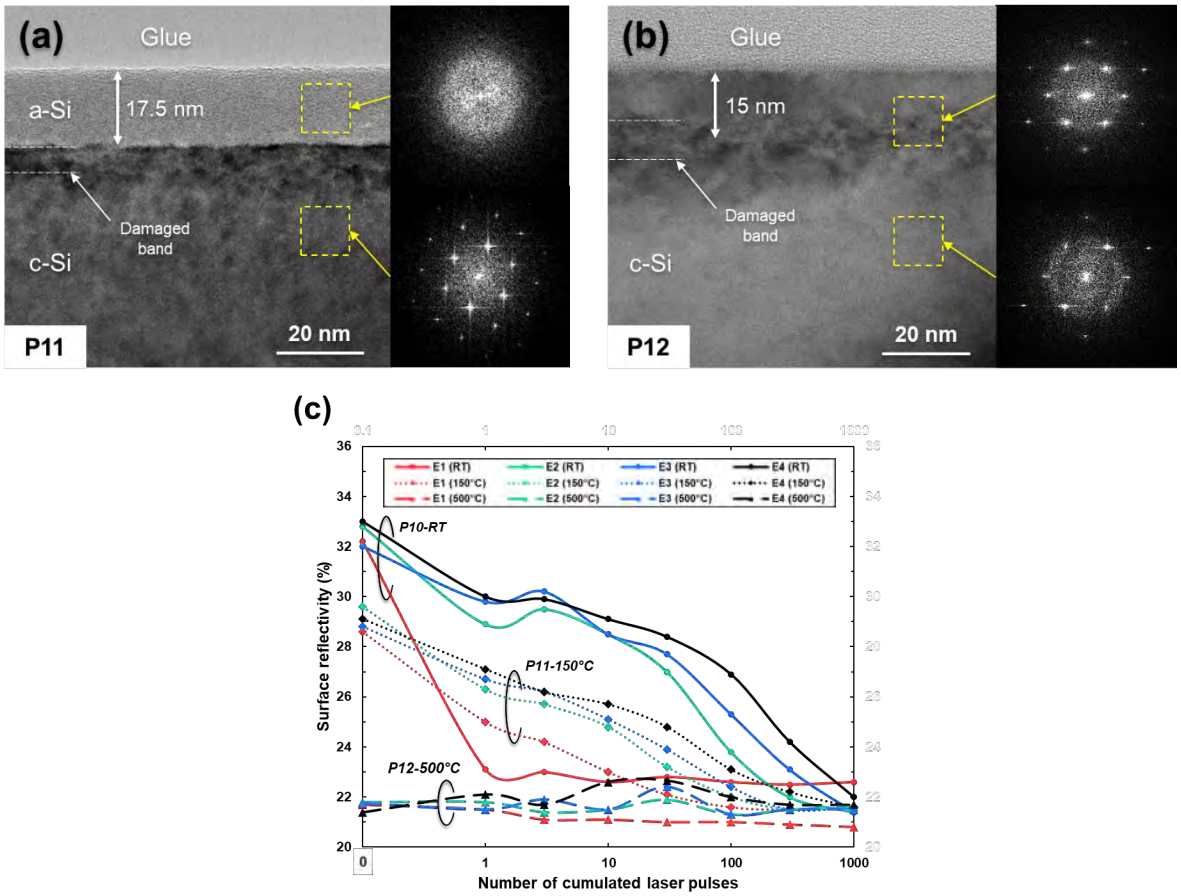

Figure 2: TEM image of as-implanted layers P11 (a) and P12 (b), maintained at 150 °C and 500 °C during implantation process, respectively. (c) TRR measurements performed during each laser annealing conditions, compared to their initial surface reflectivity (at 0 pulse). Lines are guide to the eyes only.

These results corroborate the TRR measurements made at 0 pulse (Fig. 3 (c)). The as-implanted P12 layer keeps the same surface reflectivity (~22%) between 0 and 1000 pulses, corresponding to a crystalline Si layer. For both as-implanted P10 and P11 layers, the implantation conditions lead to the formation of a thin a-Si layer. This amorphous continuous layer tends to recrystallize when increasing the number of laser pulses, evidenced by the reduction of surface reflectivity towards the c-Si reflectivity (~22%). At 0 pulse, the surface reflectivity of P10 (~32%) is slightly higher than the one of P11 (~29%), which means that the amorphous layer of P10 could be thicker or denser than P11 (soon to be confirmed). The initial conditions of each layer are summarized in Tab. 2.

Table 2: Initial crystalline state of the implanted layers P10, P11 and P12.

	P10	P11	P12
Implantation conditions Chuck temperature	6 keV / 1x10^{15} cm^{-2} RT	6 keV / 1x10^{15} cm^{-2} 150 °C	6 keV / 1x10^{15} cm^{-2} 500 °C
Amorphous layer	~20 nm (to be confirmed)	17.5 nm	No amorphous layer
Damaged region depth	15 to 20 nm (5 nm band)		

In the next sub-sections, we will first describe the most remarkable cases, starting with P10 and then, with P12, and finally discuss the intermediate case P11.

2.3.3 Phosphorus implantation at room temperature (P10)

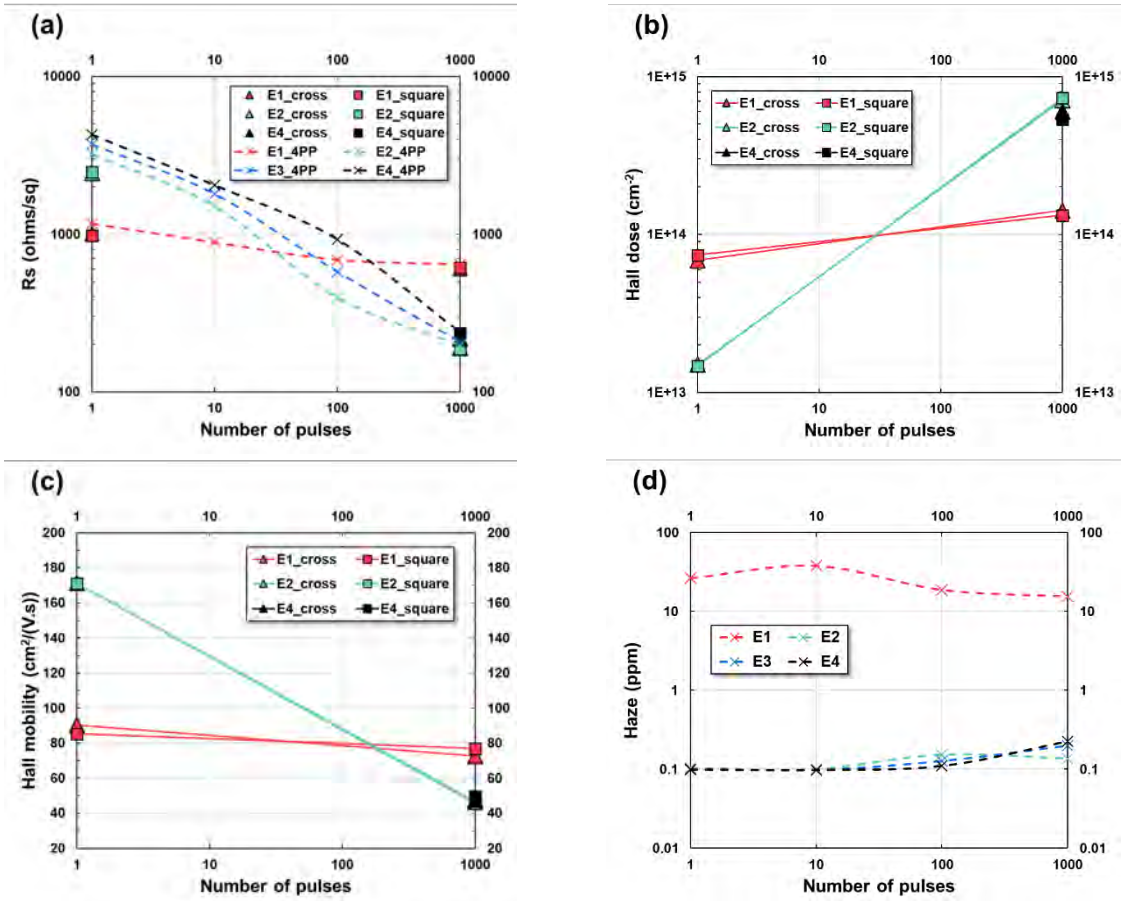

Figure 3: Electrical parameters measured on wafer P10 as function of the number of pulses for the 4 selected energy densities below melt threshold: sheet resistance R_S (a), Hall dose N_H (b) and Hall mobility μ_H (c). The sheet resistance has been measured using 4PP (CEA-LETI) and Van der Pauw (LAAS-CNRS) methods. Hall dose and mobility have been extracted by HE measurement (LAAS-CNRS). (d) Haze values (surface roughness) as function of the number of laser pulses. Lines are guide to the eye only.

In the case of wafer P10, we notice that all measurements from energy density E1 differs from E2, E3 and E4. In Fig. 3 (c), the reflectivity for E1 strongly decreases between 0 and 1 pulse, to stabilize around 23%, contrary to all the other energy densities, for which the reflectivity values are almost linearly decreasing to 22%. This is clear evidence of the explosive recrystallization phenomenon that transforms the amorphous silicon surface layer into a

polysilicon layer. The slight difference in reflectivity (1%) might be explained by, first, the significant surface roughness (Fig. 4 (d)) and, second, by the difference of crystallinity.

At 1 pulse, once the amorphous layer becomes polycrystalline, the electrical parameters do not vary considerably when increasing the number of pulses as the thermal budget brought by the laser acts like a short duration conventional furnace annealing (Fig. 4 (a-c)). Indeed, Hall doses measured by HE show a low impact of the number of laser pulses on the activation of phosphorus dopants: from ~6.8% to ~13% between 1 and 1000 pulses, corresponding to maximum concentrations of 2.2 – 4.5x10^{19} cm^{-3}, supposing a uniformly doped 30 nm thick layer.

For energy densities E2, E3 and E4, we observe the opposite results compared to E1. The linear decrease of reflectivity between 1 and 100 pulses indicates a SPER process, which promotes the dopant activation levels above the solid solubility (to be confirmed soon by TEM). In this case, the amorphous/solid interface moving towards the surface when increasing the number of laser pulses. At 1 pulse, a better activation is measured for E1 (~6.8%) compared to E2, E3, and E4 (<1.5%). The main benefit of SPER is highlighted at 1000 pulses, with an almost unchanged activation for E1 (~13%) and significantly improved activation for E2, E3, and E4 (between 51% and 69%). This process leads to beneficial advantages compared to regular annealing in terms of electrical properties and surface roughness (Fig. 4): strong sheet resistance lowering, high activation rates and low surface roughness. If we hypothetically consider a uniform doping concentration over 30 nm, the laser condition E2-1000p allows to reach concentration levels as high as 1.7 - 2.3x10^{20} cm^{-3}. As the TRR signals of E2-E4 laser conditions do not show a clear asymptotic behavior at 1000 pulses, the SPER process might not be complete. As so, extending the number of pulses on the actual design of experiments could lead to even more promising results.

To conclude this section, the presented results confirmed that SPER constitutes a relevant process to activate dopants without causing surface roughness degradation. In addition, depending on the device fabrication process requirements, the duration/temperature trade-off of this process can be easily done by tuning the number of pulses and the energy density.

2.3.4 Phosphorus implantation at 150 °C (P11)

Similar to wafer P10, P11 has an amorphized surface layer (~17.5 nm, Fig. 3 (a)) due to implantation conditions. Surprisingly, electrical results from E1 and the three other energy density conditions E2, E3 and E4 can be studied separately even if they all tend to very comparable results at 1000 pulses. Indeed, TRR measurements in Fig. 3 (c) exhibits a divergence between the reflectivity signal of E1 and E2, E3 and E4 from the first laser pulse. At 1000 pulses, the four surface reflectivities converge to the same value of 22% (c-Si), which suggest the complete recrystallisation of the layers. Same variations as TRR are observed for the sheet resistance, however the Rs value at 1000 pulses is higher for E1 than the other three energy densities. When analyzing the variations of Hall dose and Hall mobility, the described behavior is even more explicit. While Hall values of E1 appear to reach a saturation limit, the ones of E2, E3 and E4 follow a linear trend from 1 to 1000 pulses, with a slightly better activation at 1000 pulses (and so, a lower Hall mobility). Considering a uniformly doped layer of 30 nm (SPER), E2 – E4 allows to achieve 52% - 58% of maximum activation with maximum phosphorus concentrations of 1.7 – 1.9x10^{20} cm^{-3}. Despite the supposedly complete recrystallisation of the surface amorphous layer, the linear variations exhibited by the electrical parameters at energy densities E2, E3 and E4 suggest that an activation improvement could

be expected when extending the number of pulses. Also, interestingly, the surface roughness stays at low values (~0.1 ppm) independent of the number of pulses. To confirm the complete recrystallization of the layers and assess the presence of defects, we performed TEM plan view analysis on E1-1000 pulses and E2-1000 pulses.

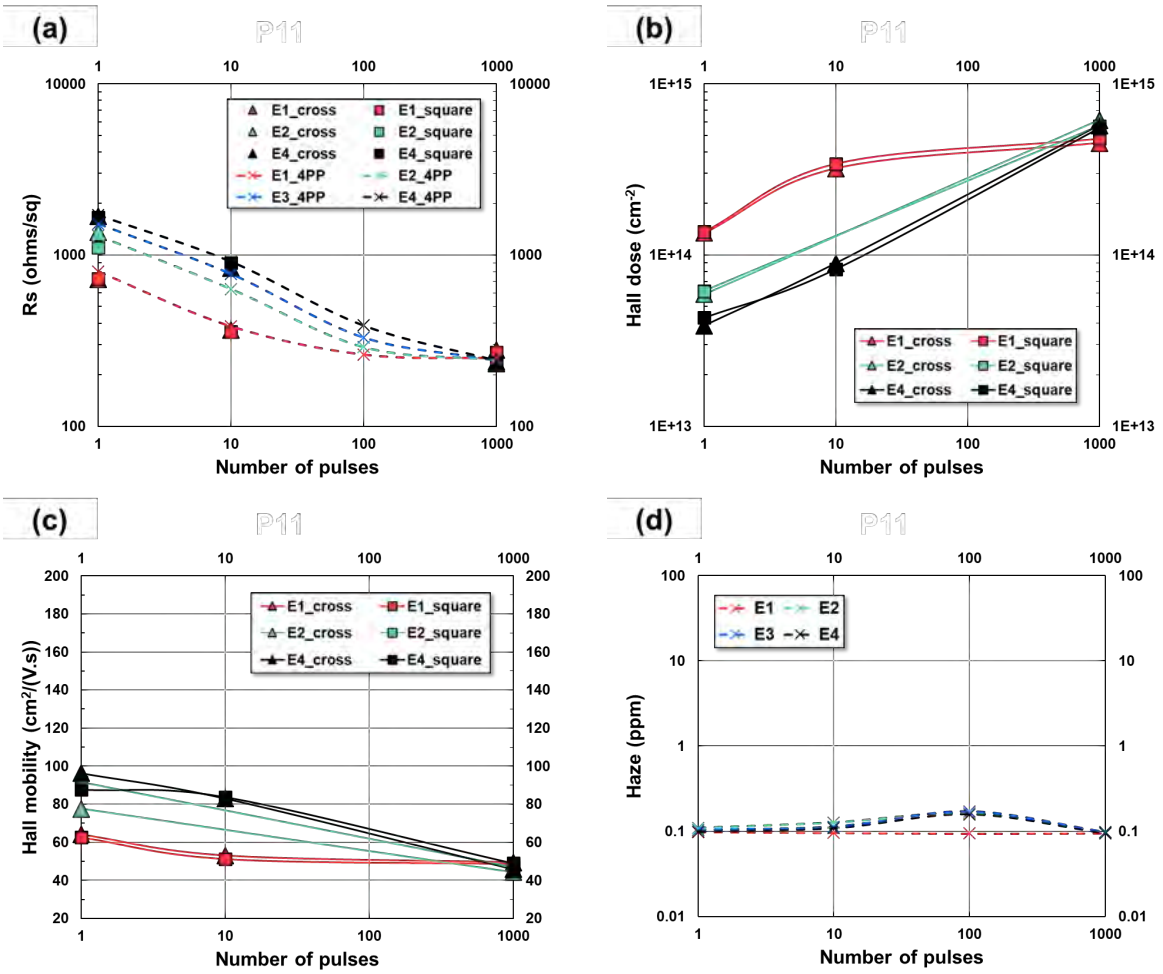

Figure 4: Electrical parameters measured on wafer P11 as function of the number of pulses for the four selected energy densities below melt threshold: sheet resistance R_S (a), Hall dose N_H (b) and Hall mobility μ_H (c). The sheet resistance has been measured using 4PP (CEA-LETI) and Van der Pauw (LAAS-CNRS) methods. Hall dose and mobility have been extracted by HE measurement (LAAS-CNRS). (d) Have values (surface roughness) as function of the number of laser pulses. Lines are guide to the eye only.

2.3.5 Phosphorus implantation at 500 °C (P12)

As mentioned previously, and contrary to wafer P10, the implantation conditions of wafer P12 prevent the layer from amorphizing (Fig. 3 (b)). The addition of thermal budget by laser annealing did not modify the crystal quality enough to involve variations in the measured TRR signal, remaining at 22% from 0 to 1000 pulses (Fig. 3 (c)). The possible expected drawback for having a crystalline layer after the implantation process is that the defects observable in the 5 nm band buried below the surface may not be healed by the subsequent laser annealing, contrary to SPER process. For this reason, the electrical measurements and surface morphology characterizations of the layers (Fig. 6) have been combined with further structural observations by TEM (weak beam dark-field microscopy) (Fig. 7).

The electrical parameters presented in Fig. 6 evolve with the same trend for all the selected energy densities. Increasing the number of pulses from 1 to 1000 improves the Hall doses (and so, the active doses and activation rates) (Tab. 3):

Table 3: Active doses values (calculated from Hall doses assuming $r_H \sim 1$ for phosphorus-doped silicon with high levels of concentrations) along with activation rates as function of the energy density (E1, E2 and E4) and the number of laser pulses (between 1 and 1000 pulses) for wafer P12 (implantation at 500 °C).

Active dose (cm^{-2}) *Activation (%)*		**Number of pulses**		
		1	**10**	**1000**
Energy density (J/cm^2)	**E1**	7.20×10^{13} *7.2%*	1.45×10^{14} *14.5%*	4.90×10^{14} *49%*
	E2	4.40×10^{13} *4.4%*	-	3.60×10^{14} *36%*
	E4	2.8×10^{13} *2.8%*	3.3×10^{13} *3.3%*	8.7×10^{13} *8.7%*

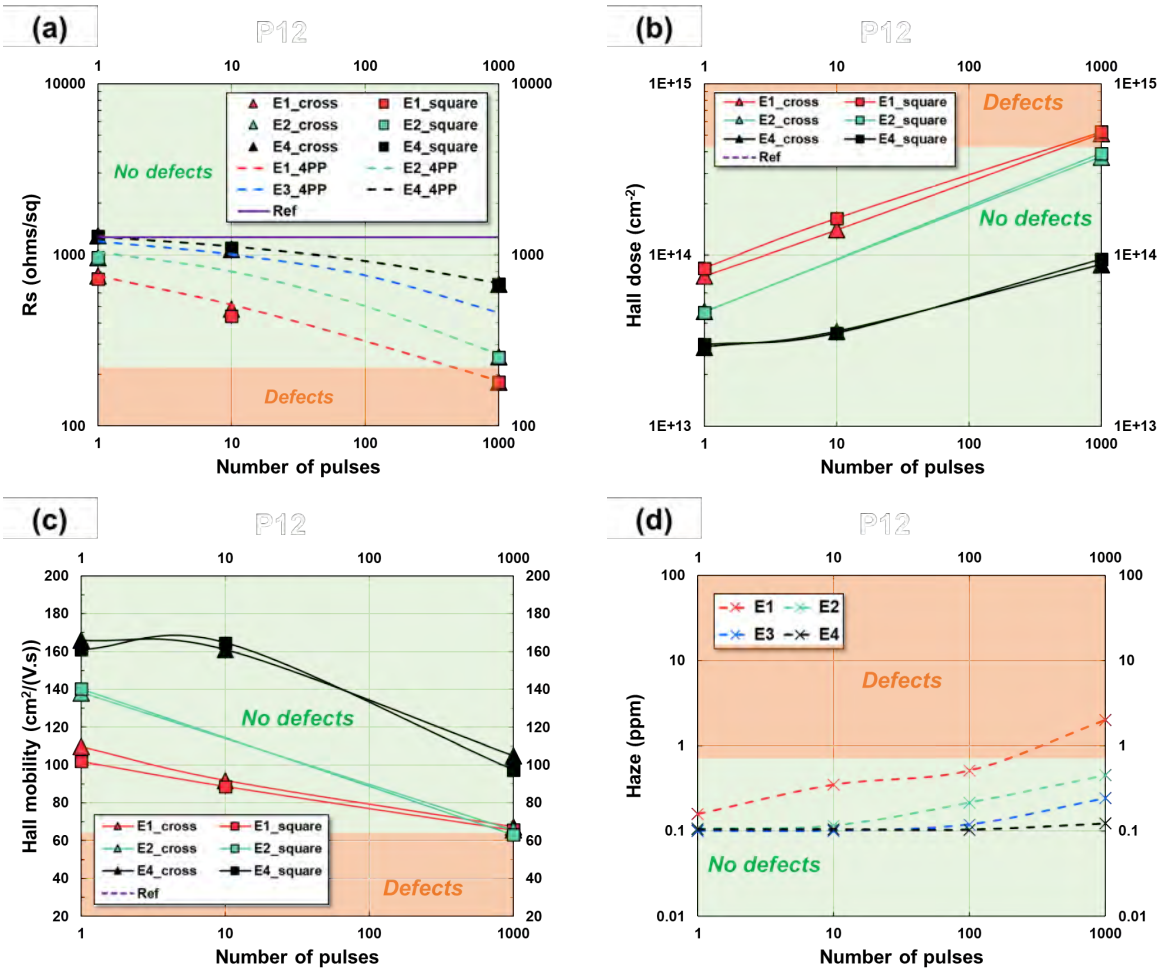

Figure 5: Electrical parameters measured on wafer P12 as function of the number of pulses for the four selected energy densities below melt threshold: sheet resistance R_S (a), Hall dose N_H (b) and Hall mobility μ_H (c). The sheet resistance has been measured using 4PP (CEA-LETI) and Van der Pauw (LAAS-CNRS) methods. Hall dose and mobility have been extracted by HE measurement (LAAS-CNRS). (d) Haze values (surface roughness) as function of the number of laser pulses. For all graphs, orange and green backgrounds specify the presence of observable defects, based on TEM observations. Lines are guide to the eye only.

Supposing a uniformly doped layer of 50 nm (according to TEM observations and not considering SPER), E1-1000 pulses enables reaching maximum concentrations between

$9.7x10^{19}$ – $1.0x10^{20}$ cm^{-3}. Interestingly, for a given number of pulses, the activation phenomenon is even enhanced when increasing the energy density. These results show that the activation depends not only on the number of pulses but also on the energy density. Both parameters are crucial to reach the highest thermal budget without exceeding the melt threshold, thus favorizing the introduction of dopants into substitutional positions.

Fig. 6 (d) shows the evolution of the surface roughness with the number of pulses. From these data, we observe the apparition of surface roughness at 1000 pulses for E3, at 100 pulses for E2 and at 1 pulse for E1. Once these thresholds are reached, the haze values keep increasing when increasing the number of laser pulses. Due to the specific fabrication conditions of P12 (heated ion implantation at 500 °C), one might expect that the degradation of the surface roughness could be caused by mechanical stress, coming either from dopants or interstitials clustering into crystal defects. Based on data from Fig. 6 (d), we explored different laser conditions by TEM plan views and cross-sections, as presented in Tab. 4. Low cumulated thermal budget conditions (including as-implanted layer), with insufficient maximum temperature (i.e., low energy densities) and/or number of pulses, as E1-1pulse, E4-1pulse and E4-1000 pulse, do not exhibit crystal defects, in agreement with associated low haze values (Fig. 6 (d)).

Table 4: Summary table of TEM observations on wafer P12 as function of laser conditions (energy density and number of pulses). Two types of observations have been conducted: plan views (PV) and cross-sections (CS). Blue and red denominations designate done and planed observations, respectively. Also, orange, and green backgrounds specify the presence or absence of observable defects.

P12		Number of pulses				
		0	1	10	100	1000
Energy Density (J/cm²)	E1		PV		PV	PV / CS
	E2					PV
	E3					
	E4		PV			PV
	0	PV / CS				

For high thermal budget conditions, E1-100 pulse shows no difference to low thermal budget conditions with no observable defects. The E2-1000 pulse laser condition shows signs of surface texture that were not precisely identifiable, but which might suggest the early stages of defects formation. When reaching the highest cumulated thermal budget E1-1000 pulse, we can clearly observe micrometer-long line-shaped defects oriented along [010] and [100] axis with bracket-like tips oriented along [110] and [1-10] axis (Fig. 7 (a)). In order to identify the nature of these defects through Burgers vectors, 220 and 400 TEM weak-beam bright (BF) and dark field (DF) imaging mode was used in g/2g condition (Fig. 7 (b-d)). The presented DF images did not show clear signal intensity variations, indicating an uncommon Burgers vector. Further TEM weak beam observations are required in additional directions to assess the defects' nature. Based on the TEM observations, a threshold correlated to the presence of defects can be added to Fig. 6 for the electrical parameters analysis. The defects depicted in Fig. 7 appears when reaching an activation rate between 36% (E2-1000 pulses) and 49% (E1-1000 pulses).

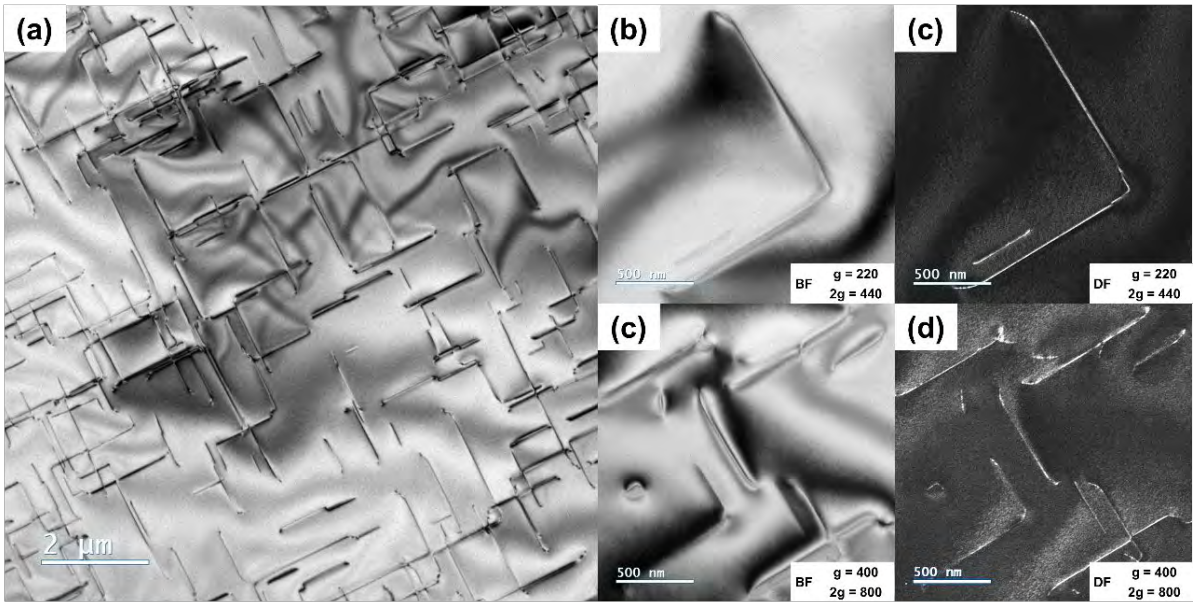

Figure 6: TEM observations conducted on P12 layer annealed with laser condition E1 with 1000 pulses. Two different modes have been used: standard TEM mode (a) and weak-beam bright field (BF) and dark field (DF) mode (b-d). For weak-beam mode, two different directions with g/2g condition have been selected: 220 and 400.

Giving the sheet resistance and Hall dose trends as function of the number of laser pulses, the activation might not have reached a saturation regime, which suggest that the micrometer bracket-shaped defects could originate from interstitials segregation during the laser annealing process. To confirm this hypothesis, laser annealing conditions with higher thermal budgets compared to this design of experiment should be conducted, for example by extending the actual number of pulses to 2000 or even 5000. By doing so, the evolution of the found defects could be monitored as function of the transmitted thermal budget. Several experiments have been planned to push the study of the laser-annealed 500 °C-implanted Si:P layers forward. These experiments have been summarized in Tab. 5.

Table 5: Summary of planned future experiments for laser-annealed wafer P12.

Planned experiments	Objectives
TEM	Further TEM plan views and cross-sections weak-beam observations **to identify Burgers vector**
AFM	Morphology analysis of laser condition P12-E1-1000 pulses **to quantitatively understand corresponding measured haze values**
Hall	Hall measurement as function of temperature on P12-ref and P12-E1-1000 pulses **to evaluate the impact of the defects formed after laser annealing on electrical properties (scattering phenomena)**
SIMS	SIMS chemical profiling measurement **to assess phosphorus dopants diffusion with laser annealing**

Heated implantation at 500 °C prevents silicon from amorphizing while allowing a small quantity of phosphorus dopants (<3%) to incorporate in substitutional position. Subsequent sub-melt laser anneals give access to acceptable levels of activation (50%) with appropriate laser conditions. However, contrary to the SPER process, due to the absence of amorphized layer, the damaged crystal cannot heal in a comparable way. As a consequence, when reaching an activation threshold of around 40%, micrometer-long defects form inside the layer, which might give rise to significant scattering phenomena.

2.4 Arsenic-implanted silicon

In D2.4, the simulation results of several heated implantations have been presented. The predictions of the KMC simulations regarding as-implanted amorphization were compared to TEM cross-section images and demonstrated the reliability of KMC in this case. The type of defects after annealing predicted by KMC could also be compared with TEM images. The KMC predictions were reliable for the room-temperature (RT) and 150 °C implantations, for which DLs are observed in TEM and simulated in KMC, but not for the 500 °C implantation. The defects observed in TEM after the annealing following the 500 °C implantation were {311} defects while KMC predicts DLs. This problem will be discussed in section 2.4.2 on the calibration of interstitial clusters in KMC. Another problem encountered was the computational time required to simulate the annealing. A possible solution to this problem is to use KMC to simulate the implantation and continuous methods to simulate the annealing. This method allows to take advantage of the KMC approach to take into account the implantation temperature and of the efficiency of the continuous method to simulate the evolution of defects during annealing.

2.4.1 Hybrid KMC-continuum modelling

To be able to simulate the implantation in KMC and annealing with the continuous model it is necessary to correctly transfer discrete data from the KMC into continuous data fields to initialize the annealing simulation. The transition between the KMC and the continuous model is integrated in the Sentaurus Process solver in a Tcl procedure called `UnsetAtomistic`. In the KMC interstitials are stored in different types of defects: DLs, {311} defects, small interstitial clusters (SMICs), impurity clusters and amorphous pockets. The `UnsetAtomistic` procedure converts the excess interstitials in these different defects into a continuous field with the help of an internal mesh. Amorphous pockets are clusters containing both interstitial and vacancies and is the defect kind where the most interstitials are trapped following a RT implantation. During annealing the interstitials and vacancies in an amorphous I_nV_m pocket recombine between themselves until only one type of defect remains (I or V). The `UnsetAtomistic` procedure calculates the $n-m$ difference for each amorphous pocket I_nV_m and if the result is positive, converts this amount into excess interstitial. For other types of defects containing interstitials, no recombination takes place, and the excess interstitials are therefore equal to the number of interstitials in the defect.

Table 6: Interstitial density trapped in DLs. The TEM count is compared to the method using the default `UnsetAtomistic` to transfer KMC data to continuum (initial `UnsetAtomistic`) and to this work procedure (New `UnsetAtomistic`)

Interstitial in DLs (cm^{-2})	TEM	Initial `UnsetAtomistic`	New `UnsetAtomistic`
RT	1.4×10^{14}	2.1×10^{15}	9.4×10^{13}
150 °C	1.6×10^{14}	3.1×10^{15}	3.9×10^{14}

In a first test the `UnsetAtomistic` procedure was used, and the interstitials were stored in the I_2 continuous field (corresponding to the di-interstitial concentration). The model presented in [14] was then used to simulate the evolution of defects during annealing. This procedure allows to simulate DLs, but the density of trapped interstitials (Initial `UnsetAtomistic` column in Tab. 6) is one order of magnitude higher than the one counted in the TEM images in D2.4.

To solve this issue the `UnsetAtomistic` procedure has been changed. One of the problems was that only excess interstitials in amorphous pockets were counted but not excess vacancies. During the annealing process a certain amount of recombination between interstitials and vacancies emitted from vacancy clusters took place, reducing the interstitial concentration. The excess vacancies in the amorphous pockets are therefore stored in the new procedure in a continuous field. A model taking into account the vacancy clusters in the annealing is then run to simulate the annealing. The evolution of interstitial clusters, {311} defect and DLs is still done with the model of [14]. In order to better simulate the recombination at the beginning of the annealing, the first annealing ramp is also simulated in KMC.

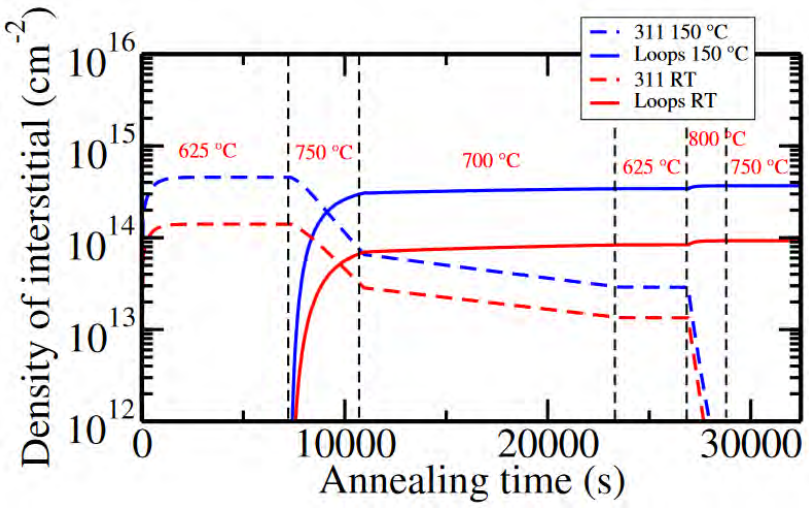

Figure 7: Number of I trapped in DLs and {311} defects using the hybrid approach combining KMC and continuum model after implantation at RT (red) and at 150 °C (blue).

This change in the `UnsetAtomistic` procedure results in a better agreement between simulations and TEM count (see New `UnsetAtomistic` column in Tab. 6). The densities of interstitials trapped in DLs in the 150 °C case is still larger than the experimental value. This method allows to speed up the calculation by a factor 8 for the 150 nm x 150 nm KMC surface.

2.4.2 Interstitials cluster calibration

The KMC simulation does not match the experimental trends for the 500 °C implantation. To recalibrate the model, it is necessary to know which parameters to calibrate. The difference between the as-implanted interstitial and vacancy profiles is shown in Fig. 9 for RT, 150 °C and 500 °C implantations. It can be seen that the interstitials-vacancies difference is similar in the 150 °C and 500 °C cases. The same number of excess interstitials can therefore be expected after the interstitial-vacancies recombination. Since the annealing sequence is the same after the 150 °C and 500 °C implantations, the parameter to be changed must be related to the types of defects in which the as-implanted interstitials are trapped.

As-implanted at 500 °C, interstitials are mostly found in SMICs. In the following, the SMICs will be described by the number of interstitials they contain, a SMIC containing n interstitials being noted I_n. The calibration of SMICs is based on a retro-engineering method detailed in [15] and has been shown to be effective in simulating defects after RT implantation processes and annealing sequences [16]. The calibration of SMICs for heated implantation has not yet been shown to be robust. In a first approach, the different kind of SMICs found in ab initio studies have been reviewed. Two types of SMICs are generally found in *ab initio* calculations: the

compact types and the chain types. The SMICs of compact type have structures with very low formation energies for an interstitial number being a multiple of $4n$. Their structures are close to the one found by Arai [17]. Chain-like SMICs have a linear structure elongated in the <110> direction.

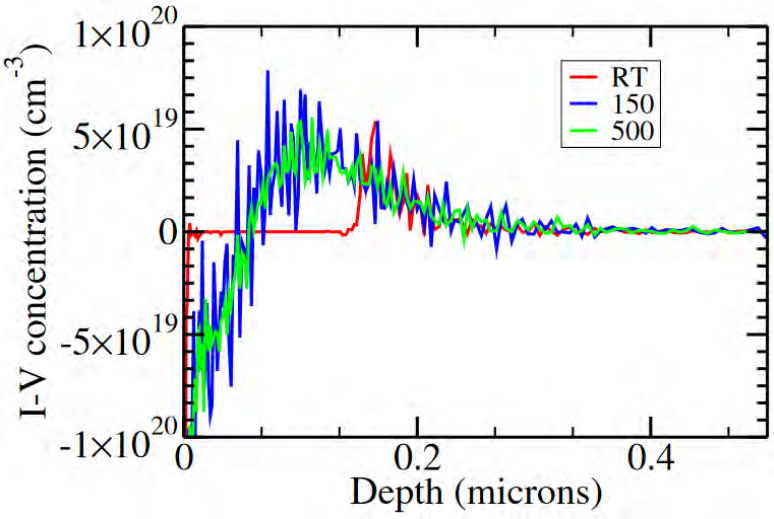

Figure 8 : Difference between interstitials and vacancies as implanted in RT, 150 °C and 500 °C As implantations.

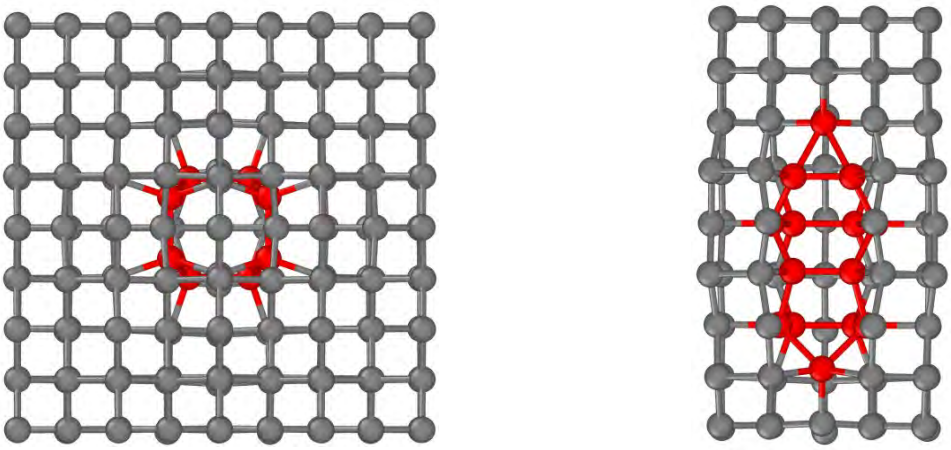

Figure 9: (Left) Compact I_4 cluster (red atoms are the Si-atoms out of their lattice position) (Right) Chain-like I_4 cluster (red atoms are the Si-atoms out of their lattice position).

The evolution of SMICs in KMC simulation depends on the activation energies for the emission of an interstitial from the SMIC. From the data of Ref. [18] it is possible to estimate SMICs emission energies for compact-type and chain-like SMICs. Using the formation energies calculated, emission energies can be estimated in the following way:

$$E_{emi}(I_n) = E_f(I_{n-1}) - E_f(I_n) + E_f(I) + E_m(I) \quad (1)$$

With $E_f(I_n)$ the formation energy of I_n, $E_m(I)$ the migration energy of an interstitial and $E_f(I)$ the formation energy of an interstitial. Different values of interstitial migration energy and interstitial formation energy can be found in the literature [15, 18]. In this work the sum $E_m(I) + E_f(I)$ has been assumed to be 4.52 eV [15].

For a small number of interstitials, the most stable structures for SMICs are the compact-like I_{4n}. In the case of implantation at 500 °C, it is possible that between two ions implanted at the same location, the clusters generated by the first collision evolve into the most stable forms of SMICs. The KMC was then calibrated by trying emissions energies for SMICs with the same trends as those observed in the calculations for compact-like SMICs: the energy differences were increased between the I_{4n} and the other SMICs. This calibration has the effect of slowing down the growth of defects during the annealing process following implantation at 500 °C. The calibration used predicted {311} defects at the end of annealing in the 500 °C case, as observed experimentally.

It is also possible to refine the calibration to use the same activation energies for the three implantation temperatures and to predict the correct type of defect in all 3 situations: DLs for the RT and 150 °C implantations and {311} defects for the 500 °C implantation case (Fig. 11 right). However, this calibration is very sensitive and is dependent on the simulation surface used. Moreover, it is not robust for other types of simulations, e.g., for supersaturation experiments [15].

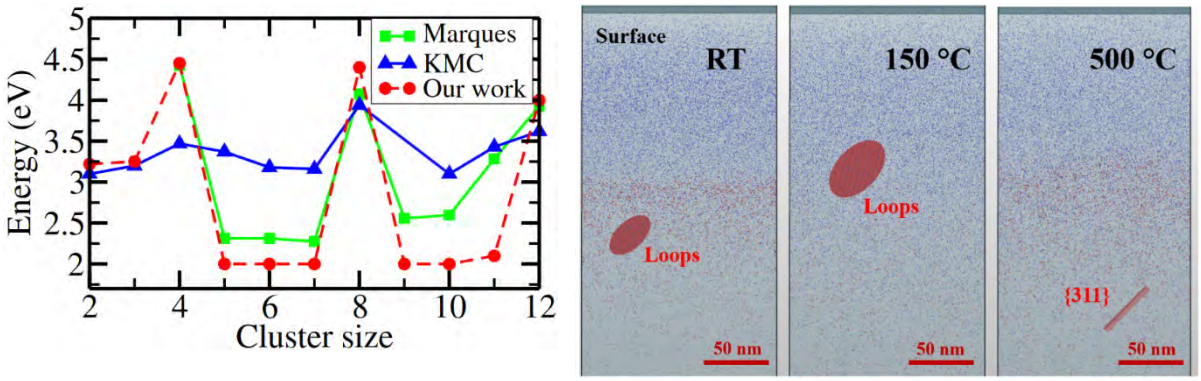

Figure 10: (Left) SMICs emission energy estimated from compact clusters formation energies of Marques, in our calibration and in the KMC initial calibration (Right) Simulation of extended defects using the calibration presented in this work for As heated implantations and annealing.

The estimation made in formula (1) should also be discussed. The estimation of the emission energies does not take into account any additional barriers. The structure of the compact I_5 seems to be a single interstitial bounded to a compact I_4. In the I_4 configuration, all silicon atoms are four bonded, which reduces the energy. The emission of an interstitial from the I_4 cluster is therefore likely to pass through high energy atomic configurations to break these bonds. In the case of I_5, the interstitial attached to the I_4 cluster seems freer to migrate away from the cluster. Fig. 12 represents the energy barriers calculated in DFT for the emission of an interstitial from compact I_4 and I_5 (the structures are identical to those of Ref. [18]). The energy differences between the emission of an interstitial from an I_4 and an I_5 are similar to those used in the calibration on the left of Fig. 11 (~2.3 eV). To temper this result, the I_3 structure used here is not the ground state found in DFT [19] and other emission paths can perhaps be found. The hypothesis of intermediate high energy configurations for the emission of an interstitial from an I_4 remains however probable.

To explain the difficulty of finding a valid calibration for both the evolution of the extended defects after the 500 °C As implantation followed by annealing and for the experiment in [15], a hypothesis would be that the types of SMICs formed during implantation depend on the implantation temperature. For RT implantation the SMICs formed after interstitial-vacancy

recombinations could be a mix of compact-like and chain-like for the larger SMICs. The presence of chain-like SMICs would allow an evolution of defects following an Ostwald maturation mechanism and is correctly described by the calibration in [15]. For implantation temperatures of 500 °C the SMICs formed would evolve during the implantation into compact-like SMICs and would slow down the growth of the extended defects. In this case it would be difficult to find a calibration of the SMICs that is both correct for the heated implantation and the RT implantation.

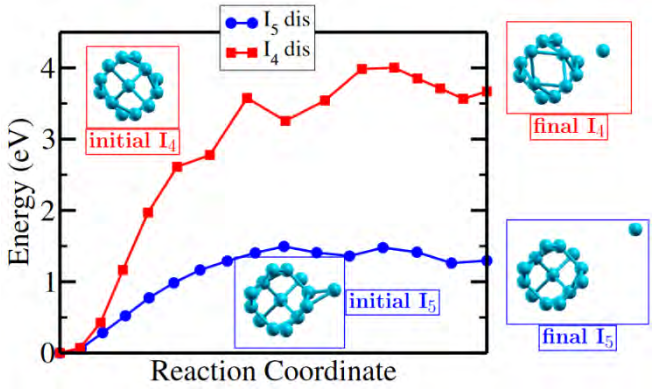

Figure 11: Minimum energy path between the I_5 configuration and a configuration with an I_4 and an additional interstitial (blue) and minimum energy path between I_4 configuration and configuration with an I_3 and an additional interstitial (red).

2.5 Boron-implanted silicon and silicon-germanium

We consider boron implantation with an implant energy of 2 keV and a dose of 1×10^{15} cm^{-2} at implant temperatures 150 °C and 500 °C. After implantation, the samples undergo non-melt laser annealing, where we consider annealing energies E1 to E4 (given by E_m – 5% / 10% / 15% / 20%) and the number of pulses varies between 1 and 1000. With the additional measurements described above, the following experimental SRP results are available for B implanted Si:

Table 7: Wf 08 Si:B – SRP measurements for implant temperature 150 °C.

Pulses ED	x0	x1	x10	x100	x1000
None	X				
E1 (E_m – 5%)					X
E2 (E_m – 10%)					
E3 (E_m – 15%)					
E4 (E_m – 20%)		X			

Table 8: Wf 09 Si:B – SRP measurements for implant temperature 500 °C.

Pulses ED	x0	x1	x10	x100	x1000
None	X				
E1 (E_m – 5%)		X	X	X	X
E2 (E_m – 10%)				X	
E3 (E_m – 15%)				X	
E4 (E_m – 20%)		X		X	

And the following experimental SRP results are available for B implanted SiGe:

Table 9: Wf 03 SiGe(20%):B – SRP measurements for implant temperature 500 °C.

Pulses ED	x0	x1	x10	x100	x1000
None					
E1 (E_m – 5%)					X
E2 (E_m – 10%)					
E3 (E_m – 15%)					
E4 (E_m – 20%)		X			

Note, that for SiGe there is only the spreading resistance available, not the active B concentration. Finally, SIMS measurements are available for as-implanted samples of Si:B, SiGe(20%):B, and SiGe(40%):B at temperatures 150 °C and 500 °C each.

In D2.3, experimental results for B-implanted Si and SiGe were shown and compared to KMC results obtained with Sentaurus Process using AdvancedCalibration KMC. This comparison revealed that the simulations drastically overestimated the depth of the B concentration. Within this section we demonstrate how to improve the calibration for KMC to better reflect the measured results demonstrated in the two previous sections. For this we first introduce possible paths of improvement, then we show a calibration for silicon based on experimental data, and finally apply this calibration to SiGe to demonstrate the effects for such a target.

2.5.1 Model for boron implantation

Ion implantation is based on Sentaurus MC in full-cascade mode. Ions lose energy via elastic nuclear scattering, which can be described by the Binary Collision Theory, and by inelastic interaction of the ion with electrons of the target. The cascades are then used by Sentaurus Process KMC, and dynamic annealing during implantation is simulated via Sentaurus Process KMC.

After implantation, it is assumed that B can be in a substitutional state, where it is immobile and electrically active, or it can itself be interstitial or pair with an interstitial. Both cases are treated equally and are referred to as B_i which are mobile during their lifetime. Since pairs of B and vacancies are energetically unfavorable during diffusion, they are not taken into account. The diffusion on the microscopical level is based on the kick-out mechanism. It is important to

distinguish this microscopically, instant diffusivity from the effective, macroscopic diffusivity that is measured in experiment. The latter describes a large number of microscopic diffusion steps over a long time and is given by [20]

$$D(B) = D(B_i^-)\frac{[B_i^-]}{[B^-]} + D(B_i^0)\frac{[B_i^0]}{[B^-]} + D(B_i^+)\frac{[B_i^+]}{[B^-]}, \quad (2)$$

where $D(B_i^j)$ are the diffusivities of the different charge states of B_i and $[B_i^j]$ are their concentrations. Finally, $[B^-]$ denotes the substitutional B concentration. The three addends depend each on the respective jump frequency $\nu_m(B_i^j)$ as well as the break-up frequency $\nu_{bk}(B_i^-)$, which describe the microscopic diffusion processes.

The parameters available for calibration are the B_i binding energy $E_b(B_i)$, the migration energy $E_m(B_i)$, as well as the ionization energy of the charge states $e_0(B_i^{+/-})$. Further parameters can be the B_i emission prefactor from boron-interstitial clusters (BICs), and the potential energies of the different BICs. Note, that these parameters have to be changed in a concerted manner to remain in accordance with the effective, macroscopical diffusivity.

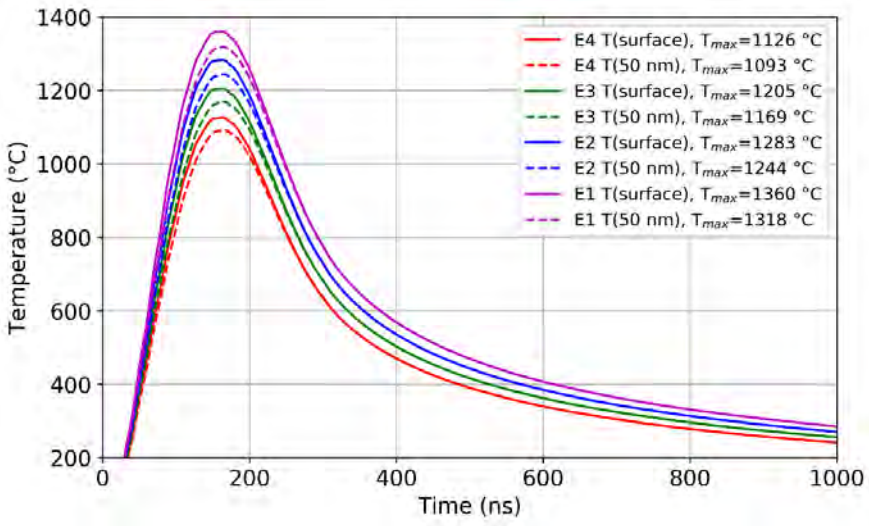

Figure 12: Temperature vs. Time of one pulse for the different fluences. The temperatures at the surface are plotted in solid lines and the temperatures 50 nm below the surface are plotted with dashed lines.

For the simulations of the laser annealing, temperature vs. time profiles of the pulses corresponding to the different fluences were provided by CNR from simulations of the laser annealing process. For the simulations here, it is assumed that the temperature is constant throughout the topmost silicon layer with the dopant profile. The profiles are shown in Fig. 13. Note that the minimum diffusion temperature is set to 400 °C during simulations, meaning that below 400 °C only the system's mechanics and not diffusion and reaction equations are solved.

2.5.2 Silicon

In Fig. 14, the comparison of experimental results and KMC simulations (with AdvancedCalibration) of as-implanted B-concentration profiles is shown. In blue the total B concentration is shown, and in orange the electrically active B concentration. Full lines denote experimental results (SIMS and SRP, respectively) and dashed lines denote the KMC results. On the left the implantation temperature is set to 150 °C, while on the right it is 500 °C.

Two discrepancies become obvious: Firstly, for both implant temperatures simulation predicts an active concentration that is drastically higher than the active concentration observed by SRP measurements. Secondly, especially at 500 °C, the simulation strongly overestimates the depth of the profiles. Both SIMS and SRP measurements suggest that the concentration profile terminates after 100 nm – 150 nm. Note that the detection limit of SIMS is around 10^{16} cm^{-3}, thus data below that threshold is not reliable, explaining in part the disparity between SRP and SIMS profiles between 100 nm – 150 nm. KMC simulations, however, predict tails in depths significantly exceeding 400 nm (not shown).

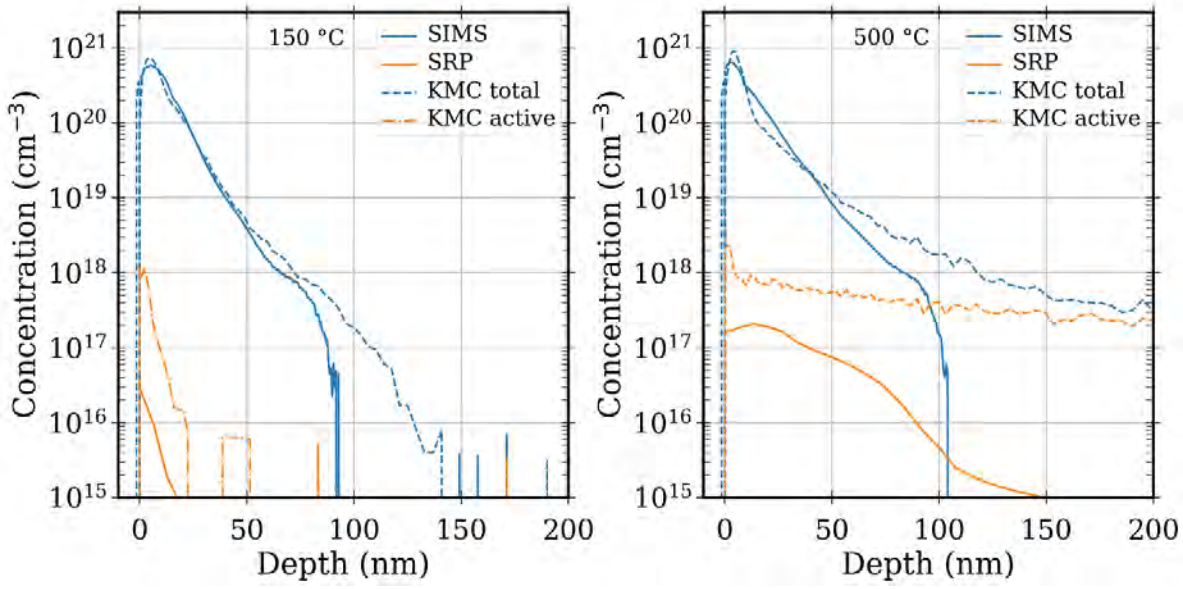

Figure 13: Comparison between experimental results and KMC simulations for the as-implanted B-concentration in Si samples for samples with implant temperatures 150 °C (left) and 500 °C (right).

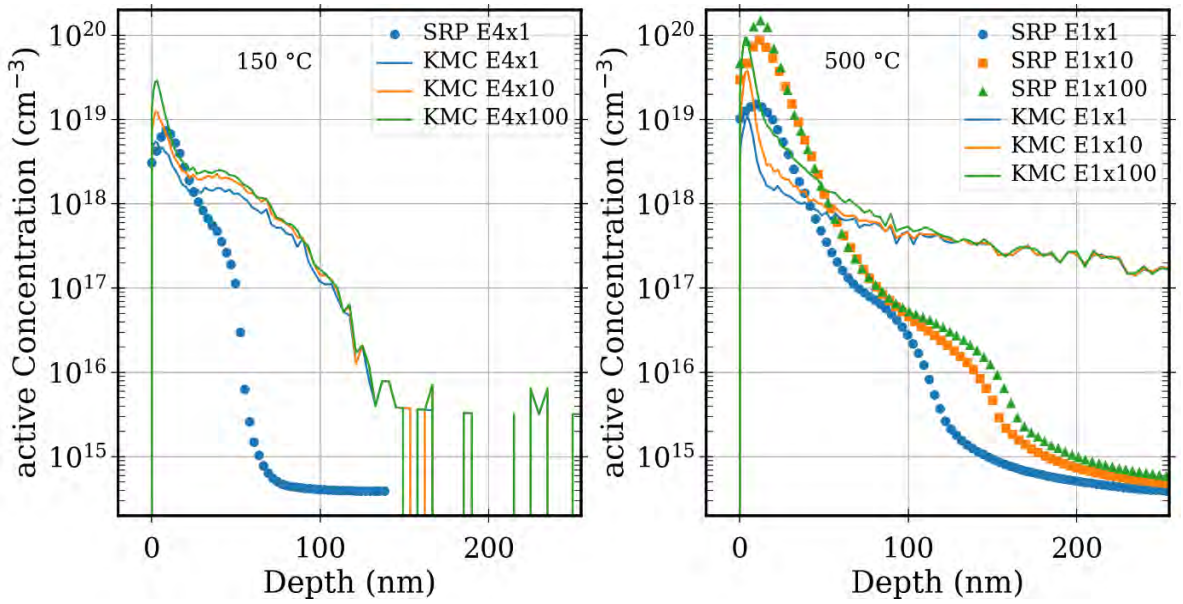

Figure 14: Comparison between SRP measurements and KMC simulations for the sub-melt laser annealing of B profiles in Si samples at different implant temperatures and fluences: (left) 150 °C and E4 (right) 500 °C and E1.

In addition, in Fig. 15 we compare KMC simulations with AdvancedCalibration for 1, 10, and 100 laser pulses with SRP data of the active B concentration after one pulse of non-melt laser

annealing with laser fluence E4 for an implant temperature 150 °C (left) and with 1, 10, and 100 pulse of non-melting laser annealing with fluence E1 for an implant temperature of 500 °C (right). SRP measurements are given by the symbols, while KMC data is given by lines. For both implant temperatures the simulations show significantly deeper profiles, just as before. Note that in both cases a single pulse is sufficient to lead to a drastic change of the SRP activation profile compared to the as-implanted profiles (see Fig. 14): for both implant temperatures the profile maximum increases more than 2 orders of magnitude after only one laser pulse.

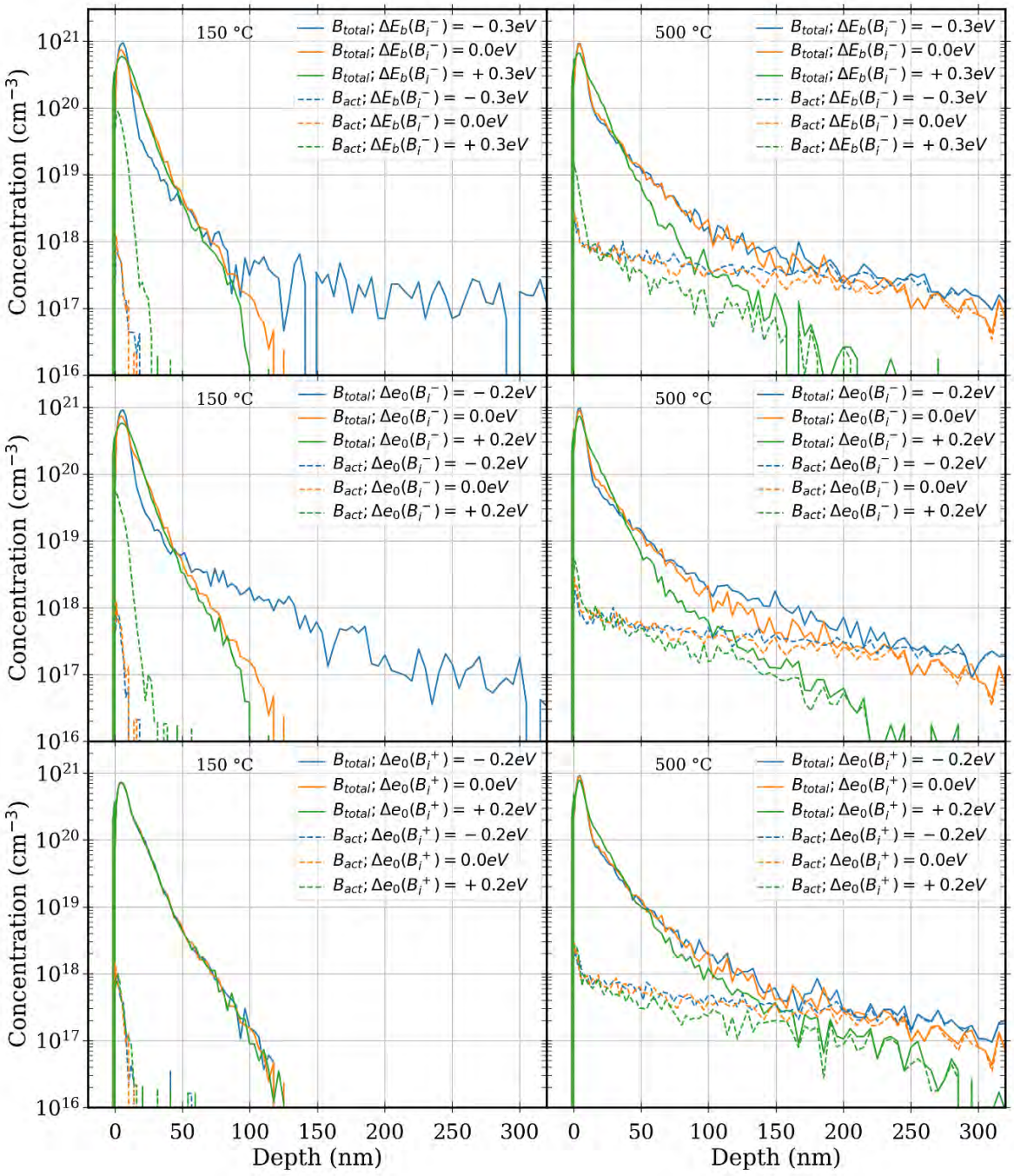

Figure 15: Variations of the as-implanted B profiles at implantation temperatures 150 °C (left) and 500 °C (right) for different energy parameters: (top) $E_b(B_i^-)$, (middle) $e_0(B_i^-)$, and (bottom) $\Delta e_0(B_i^+)$.

We find that simulation always slightly underestimates the maxima of the profiles of the annealed samples, but the general trend of increasing maximum with number of laser pulses is reproduced quite well.

The main goal of the calibration work performed was to decrease the depth of the simulated B profiles, especially for the case of implantation temperature being 500 °C, and to a lesser degree for 150 °C. There are several approaches to achieve this: either reducing the ionization energy of the B_i charge states or adapting their binding energy. In both cases the migration energies of the different B_i charge states must be adapted too in order to preserve the correct value of the effective diffusivity. From the equations of the $D(B_i^j)$ we can derive the following three constraints

$$\Delta E_m(B_i^-) = \Delta E_b(B_i^-),$$

$$\Delta E_m(B_i^0) = \Delta E_b(B_i^-) + \Delta e_0(B_i^-),$$

$$\Delta E_m(B_i^+) = \Delta E_b(B_i^-) + \Delta e_0(B_i^-) + \Delta e_0(B_i^+),$$

where Δ denotes a change in the respective energy. This means, changing the binding energy of B_i^- requires a change of the migration energies of all charge states, while changing the ionization energy of one of the charge states affects only the migration energy of two or even one charge state.

We demonstrate the effects of changing the binding energy as well as the ionization energies on the total and active concentration in Fig. 16 for both 150 °C and 500 °C. Shown are both the total B concentration as a function of depth (solid lines) and the active B concentration (dashed lines). In the top the binding energy is changed together with the migration energies of the different charge states of B_i. It is clear that increasing the binding energy drastically decreases the tails at 500 °C, while also reproducing the total concentration profile at 150 °C, the active concentration increases up to two orders of magnitude at the maximum, which is not compatible with experimental observations.

In the middle, the ionization energy $e_0(B_i^-)$ is changed and with it the migration energy of the neutral and the positively charged B_i. The results are very similar to changing the binding energy, small differences are mostly due to slightly smaller variations of the energies of 0.2 eV.

Finally, at the bottom the ionization energy $e_0(B_i^+)$ is varied and only the migration energy of the positively charged B_i must also be adapted. Here, there is a significant difference to the two other cases: at implantation temperature 150 °C there is almost no impact on the profiles. For 500 °C however, there is an impact that is less severe than for the two other cases, but when decreasing $e_0(B_i^+)$ the total and active profiles' depths decrease without the active profile's maximum increasing.

We focus on adjusting the binding energy, together with the ionization energy $e_0(B_i^+)$ and use the cluster emission prefactor $D_0(B_i)$ for fine tuning. The best fit to the total profiles was found with the following parameters:

Table 10: Parameters for the new calibration that deviate from AdvancedCalibration.

Parameter	Value
$E_b(B_i^-)$	0.95 eV
$e_0(B_i^+)$	1.14 eV
$E_m(B_i^-)$	0.514 eV
$E_m(B_i^0)$	0.857 eV
$E_m(B_i^+)$	2.162 eV
$D_0(B_i)$	487.5

The results with above parameters are shown in Fig. 17, together with the results from AdvancedCalibration and experimental results. As can be seen for the total B concentration at 150 °C implant temperature the SIMS measurements are perfectly reproduced. For an implant temperature of 500 °C the total concentration profiles of simulation and SIMS coincide up to 100 nm, however, at depths > 100 nm the SIMS data shows a drastic decrease of the concentration, while KMC simulations predict a more continuous decrease, leading again to deeper tails of the simulated profile. Nonetheless, the new calibration leads to significantly improved predictions for the total B concentration profile, compared to AdvancedCalibration.

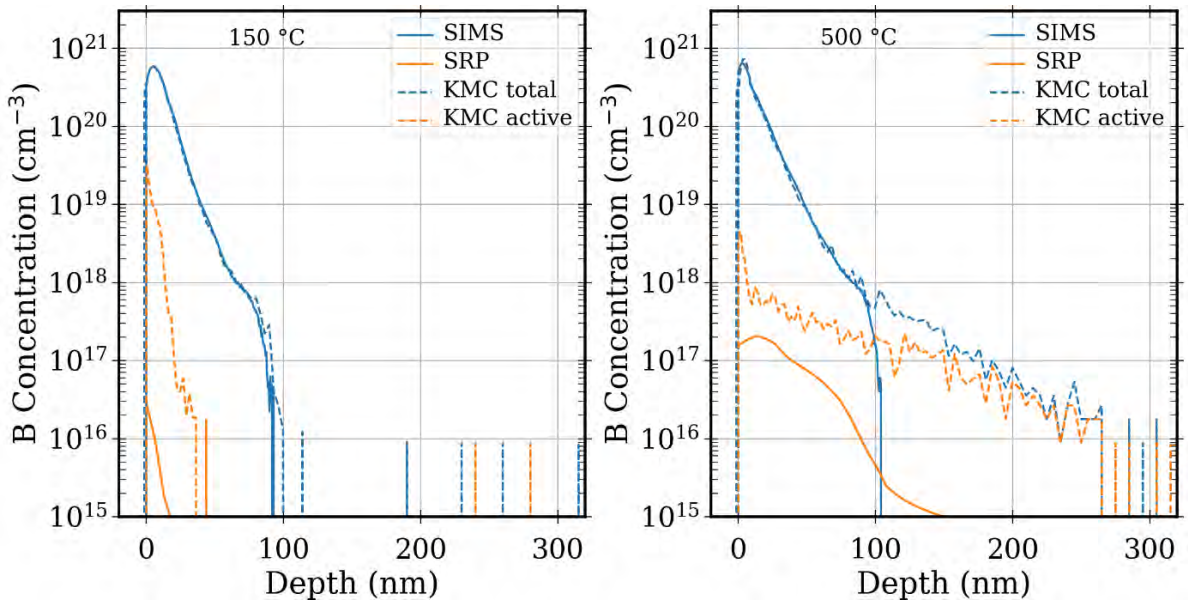

Figure 16: Comparison between experimental data from SIMS and SRP measurements with data from KMC simulations with the new calibration from Tab. 10. Shown are the total and active B concentration profiles as a function of depth for implant temperature (left) 150 °C and (right) 500 °C.

Still, even though the total profile can be fitted very well, the active concentration remains significantly above the results measured via SRP measurements. In Ref. [21] it has been shown that SRP measurements for a low number of sub-melt laser pulses (or even for as-implanted samples) underestimate the active concentration by one order of magnitude or more. This can be understood by keeping in mind that during implantation the crystal is severely damaged and that the SRP technique accounts only for mobile charge during the measurement of the active concentration. However, mobility will probably be severely reduced

due to the crystal damage. In addition, it is possible that the substitutional boron is not completely activated. As a result, SRP measurements are probably not a fully reliable resource to obtain the active concentration in this regime. Additionally, it is possible that the KMC model is not sufficiently accurate: it might be that additional processes like B-vacancy pairs and clusters have to be taken into account. This will be investigated in future work.

2.5.3 Silicon germanium

SiGe as an alloy is implemented quasi-atomistically in the KMC module of Sentaurus Process, meaning that the Ge particles are not created as particles but are implemented as a field that produces a local concentration. Of course, including Ge as an alloy makes the bandgap narrower. As a consequence, the level positions within the bandgap need also adjustment. This is achieved by an interpolation scheme, where not only the bandgap, but also diffusion-, emission-, and activation-related processes are interpolated based on the activation energies within the respective Arrhenius expressions.

For SiGe two mole fractions were studied: 20% and 40%. No SRP measurements are available for as-implanted samples, but we can use SIMS measurements as a point of reference for the total B-concentration profile. This comparison between experiment and KMC simulations with AdvancedCalibration can be seen in Fig. 18, where at the top samples with a Ge-fraction of 20% and at the bottom with a Ge-fraction of 40% are shown, to the left, the implant temperature is 150 °C and to the right it is 500 °C. Total concentration profiles are shown in blue, while active concentration profiles are orange. SIMS measurements are denoted by full lines and KMC simulation results are given by dashed lines.

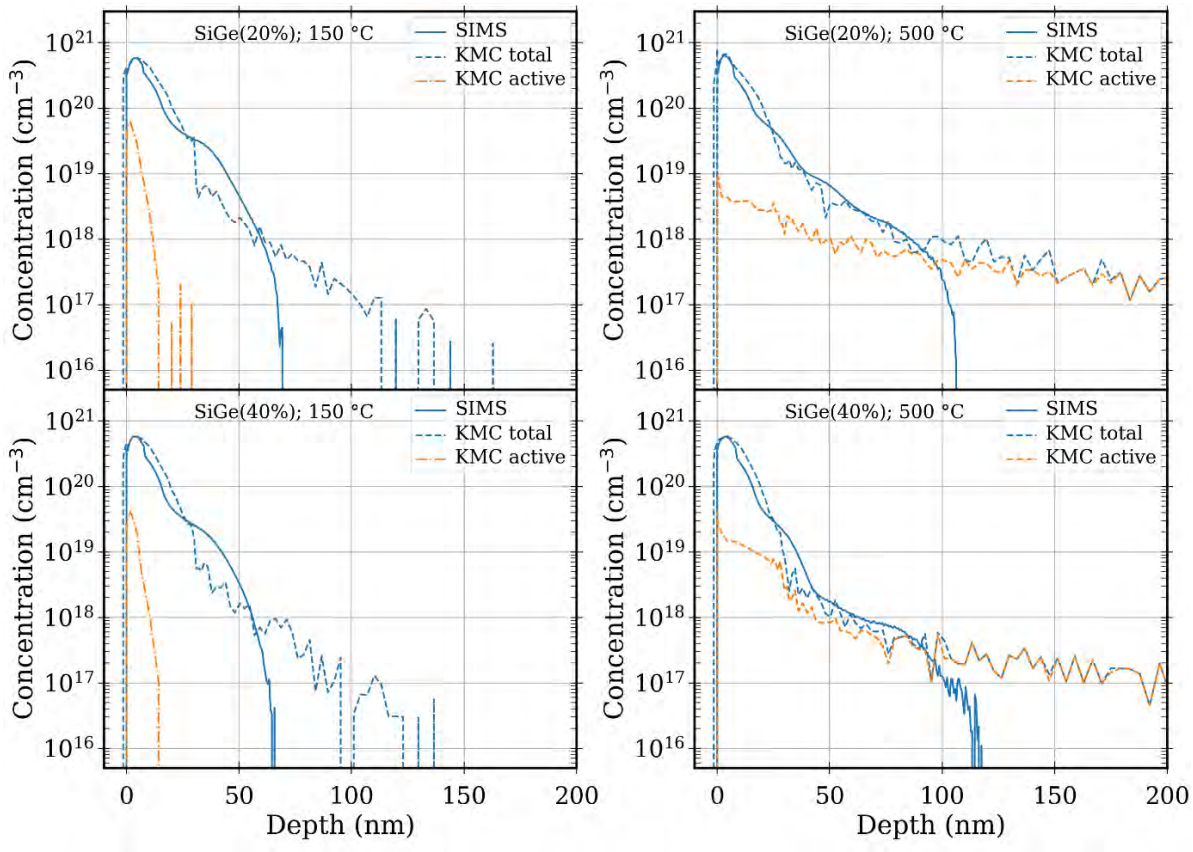

Figure 17: Comparison between experimental results and KMC simulations for the as-implanted B-concentration in SiGe samples for implant temperatures 150 °C (left) and 500 °C (right) and mole fraction 20% (top) and 40% (bottom).

Just as for Si targets, we find that the profile depths are overestimated in simulation, especially in the case of an implantation temperature of 500 °C, but also at 150 °C, but not as severe. However, apart from that KMC simulations capture the general trends very well: The maximum of the concentration profile is reproduced both in position and height perfectly, and especially at 500 °C implant temperature the slope of the curve is very well reproduced for depths up to 100 nm. This is both true for SiGe(20%) and SiGe(40%).

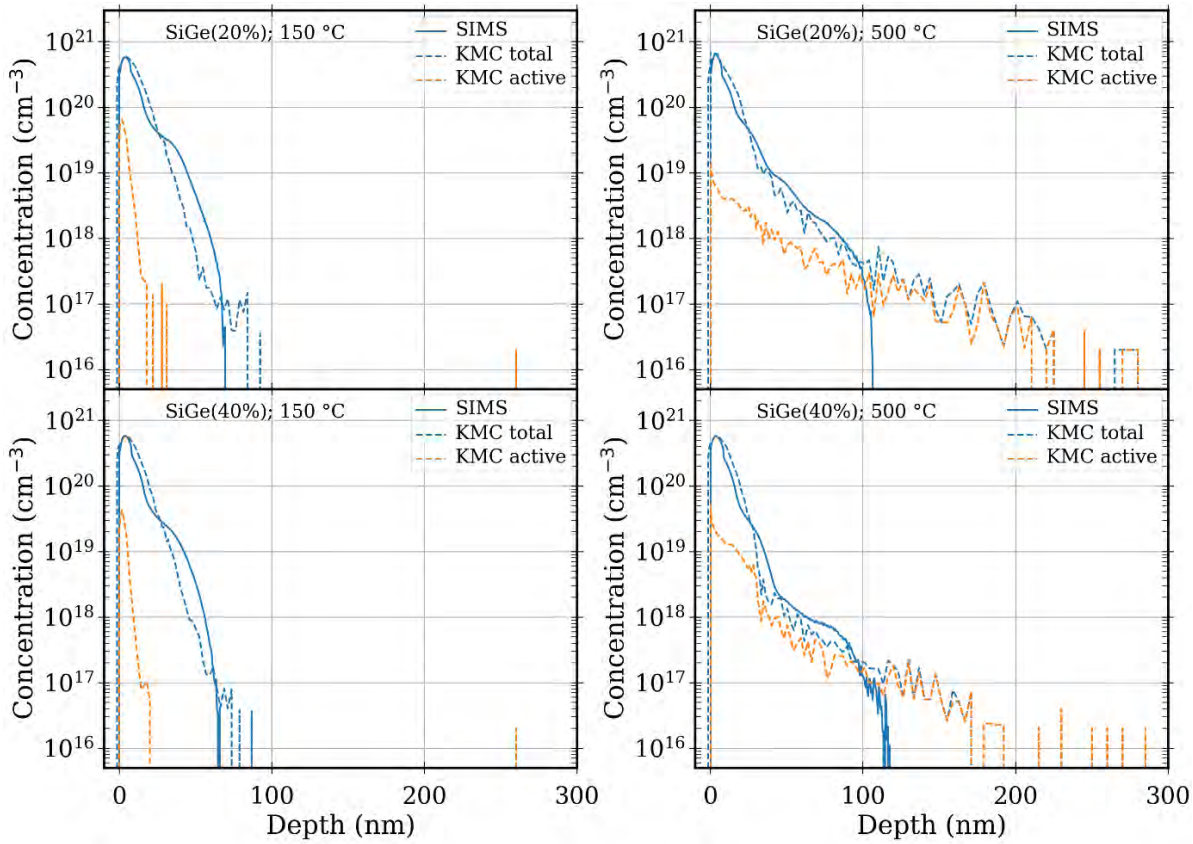

Figure 18: Comparison between experimental results and KMC simulations with the new calibration from Tab. 4 for the as-implanted B-concentration in SiGe samples for implant temperatures 150 °C (left) and 500 °C (right) and mole fraction 20% (top) and 40% (bottom).

The overestimation of the profiles' depths can be mitigated by employing the same calibration as for Si, see Tab. 10. The results are demonstrated in Fig. 19, which is the same as Fig. 18, but the simulation results were obtained not via AdvancedCalibration, but with our new calibration. As can be seen, the new calibration also improves the case of SiGe for both mole fractions. The depth of the profiles at an implant temperature of 150 °C are very well reproduced. The same is true for the position of the profiles' maxima. However, the small hump that is visible in SIMS data at about 30 nm depth is not resolved within KMC data. For an implant temperature of 500 °C we find that similarly to the case of Si as implantation target the total B concentration profiles obtained by KMC reproduce the SIMS measurements very well up to a depth of 100 nm. For higher depths SIMS measurements show a steep decrease of the concentration, while KMC simulations predict a slower decrease, leading to deeper profiles of up to approximately 300 nm. Still, this is a vast improvement over the results obtained via AdvancedCalibration. Finally, we note, that for SiGe the new calibration does not have the same detrimental effect on the active concentration as it was the case for Si. For SiGe

AdvancedCalibration and our new calibration led to similar heights of the maxima of the active B concentration profiles.

2.6 Phosphorous-implanted silicon

We consider P implantation with an implant energy of 6 keV and a dose of 1×10^{15} cm^{-2} at implant temperatures 150 °C and 500 °C. The substrate B concentration is given by 1×10^{15} cm^{-3}. After implantation, the samples undergo non-melt laser annealing, where we consider annealing energies E1 to E4 (given by E_m – 5% / 10% / 15% / 20%) and the number of pulses varies between 1 and 1000. With the additional measurements for as-implanted samples, the following experimental SRP results are available for B implanted Si:

Table 11: Wf 11 Si:P – SRP measurements for implant temperature 150 °C

Pulses ED	x0	x1	x10	x100	x1000
None	X				
E1 (E_m – 5%)					X
E2 (E_m – 10%)					
E3 (E_m – 15%)					
E4 (E_m – 20%)		X			

Table 12: Wf 12 Si:P – SRP measurements for implant temperature 500 °C

Pulses ED	x0	x1	x10	x100	x1000
None	X				
E1 (E_m – 5%)					X
E2 (E_m – 10%)					
E3 (E_m – 15%)					
E4 (E_m – 20%)		X			

No SIMS data based on the method described above is available for P-implanted Si. However, since the Si:P samples are the only ones with a pn-junction they are also the only ones where Hall measurements are available for meaningful characterization. These measurements are introduced in what follows.

2.6.1 Model for phosphorus implantation and diffusion

For P implantation and its diffusion, a similar model is employed as for B, however, with significant changes to account for differences in the diffusion physics of P. Substitutional P is immobile and electrically active, however, for P not only pairings with interstitials P_i are mobile, but P can also pair with vacancies leading to mobile P-V pairs, denoted P_v in the following. The effective diffusion is given by:

$$D(P) = D(P_i^+)\frac{[P_i^+]}{[P^+]} + D(P_i^0)\frac{[P_i^0]}{[P^+]} + D(P_v^+)\frac{[P_v^+]}{[P^+]} + D(P_v^0)\frac{[P_v^0]}{[P^+]} + D(P_v^-)\frac{[P_v^-]}{[P^+]}. \quad (3)$$

Note that two charge states of the interstitial pairs are considered instead of three for B diffusion, however, three additional terms are added due to the existence of P-V pairs. The square brackets again denote concentrations.

The parameters available for calibration are the B_i binding energies $E_b(P_i^+)$ and $E_b(P_v^+)$, the migration energies $E_m(P_i)$ and $E_m(P_v)$, as well as the ionization energies of the charge states $e_0(P_i^+)$ and $e_0(P_v^{+/-})$. Further parameters can be the B_i emission prefactor from boron-interstitial clusters (BICs), and the potential energies of the different BICs. Note, that these have to be changed in a concerted manner to remain in accordance with the effective, macroscopical diffusivity. In addition, to account for amorphization due to the implantation, the dose rate can be tuned, as well as the proportionality factor casc.amo for the switching probability between amorphous and crystalline model. At the beginning the dose rate is set to 6×10^{13} $cm^{-2}s^{-1}$, so no amorphous layer is present, which is what SRP data suggests.

For the simulations of the laser annealing of P profiles, the same temperature vs. time profiles of the pulses were used as for the annealing of B profiles, see Fig. 13.

2.6.2 Comparison between measurements and simulation

For the P implantation in Si targets no reliable SIMS measurements are available. However, SRP data from as-implanted samples can be used as point of reference for the active P-concentration profiles, see Fig. 20. There, the comparison between SRP data and KMC simulations with AdvancedCalibration is depicted for the implant temperatures 150 °C (left) and 500 °C (right). Total concentration profiles are shown in blue, while active concentration profiles are orange. SRP measurements are denoted by full lines and KMC simulation results are given by dashed lines.

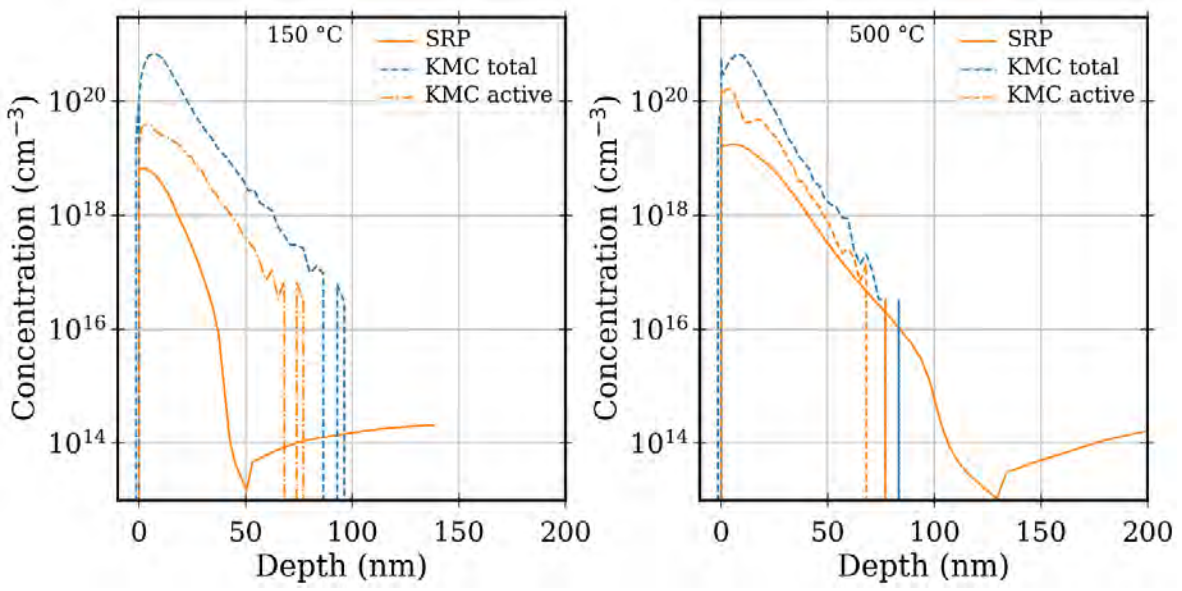

Figure 19: Comparison between experimental results and KMC simulations for the as-implanted P-concentration in Si samples for implant temperatures 150 °C (left) and 500 °C (right).

The pn-junctions are clearly visible in the SRP data as a kink in the profile at ~50 nm (150 °C) and ~130 nm (500 °C). As was discussed for B-implantation before, the as-implanted SRP

measurements may show too low activation. The depth of the pn-junction should be clearly resolved, nonetheless. As a result, simulations show a higher active P concentration, as expected, but especially in the case of 150 °C implant temperature, the depth of the profile is overestimated. In addition, KMC predicts a deeper penetration of P for 150 °C than for 500 °C which is at least unintuitive. The lower depth at higher implant temperatures should be due to lattice vibrations that prohibit effective channeling. It should be also noted that the active P profile at 500 °C shows a local minimum at ~15 nm depth, a feature that is not visible in measurements.

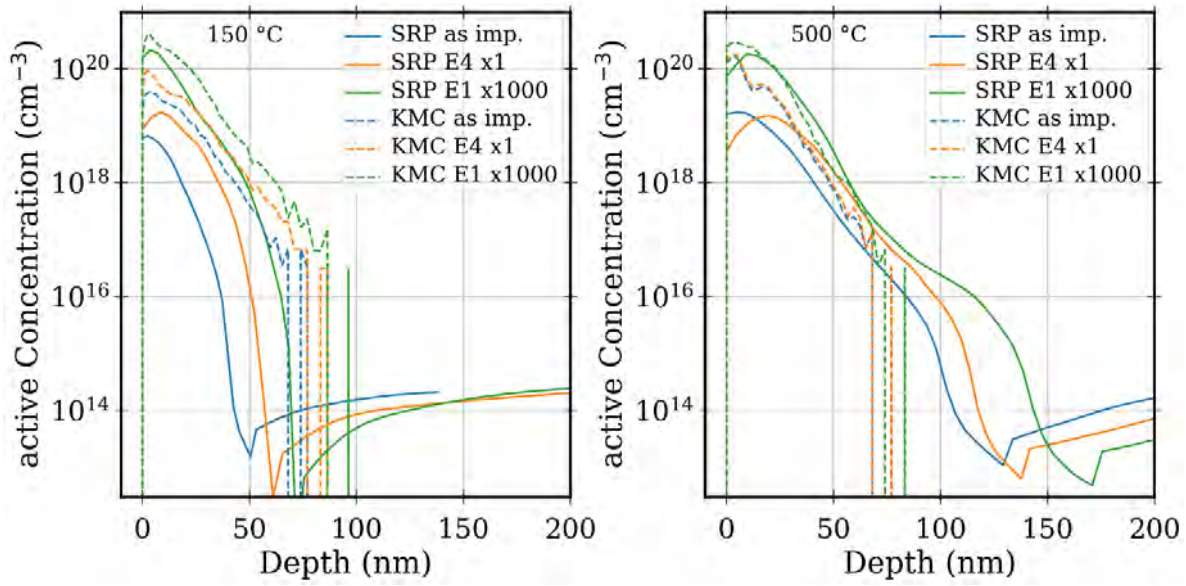

Figure 20: Comparison between SRP results and KMC simulations for the P-concentration during laser annealing in Si samples for implant temperatures 150 °C (left) and 500 °C (right).

In Fig. 21, a comparison between SRP measurements and KMC simulations is shown depicting the annealing process of the active P concentration as a function of depth for the two different implant temperatures. Shown are the as-implanted state (blue), the state after one laser pulse at the lowest energy E4 (orange) and after 1000 laser pulses hat the highest energy E1 (red). At 150 °C implant temperature the profile depths are overestimated in the simulation. Again, a higher active concentration is predicted than is actually found by SRP measurements. For 500 °C implant temperature, the as-implanted profile is still higher in simulation than in SRP measurements. However, already after 1000 laser pulses with fluence E1 we find that KMC can reproduce SRP measurements quite well.

Finally, the existence of a pn-junction in the P implanted samples allows comparisons between KMC simulations and results from Hall measurements together with SRP measurements.

This comparison can be seen in Fig. 22, where we show the active P dose as a function of annealing laser pulses from Hall measurements (Cross and Square van der Pauw structures, depicted by circles and squares respectively), SRP measurements (triangles) and KMC simulations (lines) for implantation temperatures 150 °C (left) and 500 °C (right) and for laser fluences E1 (blue) and E4 (orange). It is obvious that simulations suggest an active dose that is significantly higher than measurements. These only converge for high number of pulses, especially in the case of 150 °C, where after 1000 pulses experimental data is reproduced quite well. For 500 °C with fluence E1 this still holds, but for fluence E4, experiment shows a significantly lower activation compared to the simulation. The general trends, however, are well

captured, which can be seen from the fact, that the general forms of the experimental data sets are well reproduced but starting at a higher active dose in the as-implanted case.

Finally, we note that in TEM images for the sample at 150 °C implant temperature there is a 17.5 nm thick amorphous layer after implantation which is not present after implantation at 500 °C (see Fig. 3 (a) and (b)). In KMC simulations no continuous amorphous layer emerges at 150 °C. Only for the case of implantation at RT does KMC simulation find an amorphous layer that is about 20 nm thick.

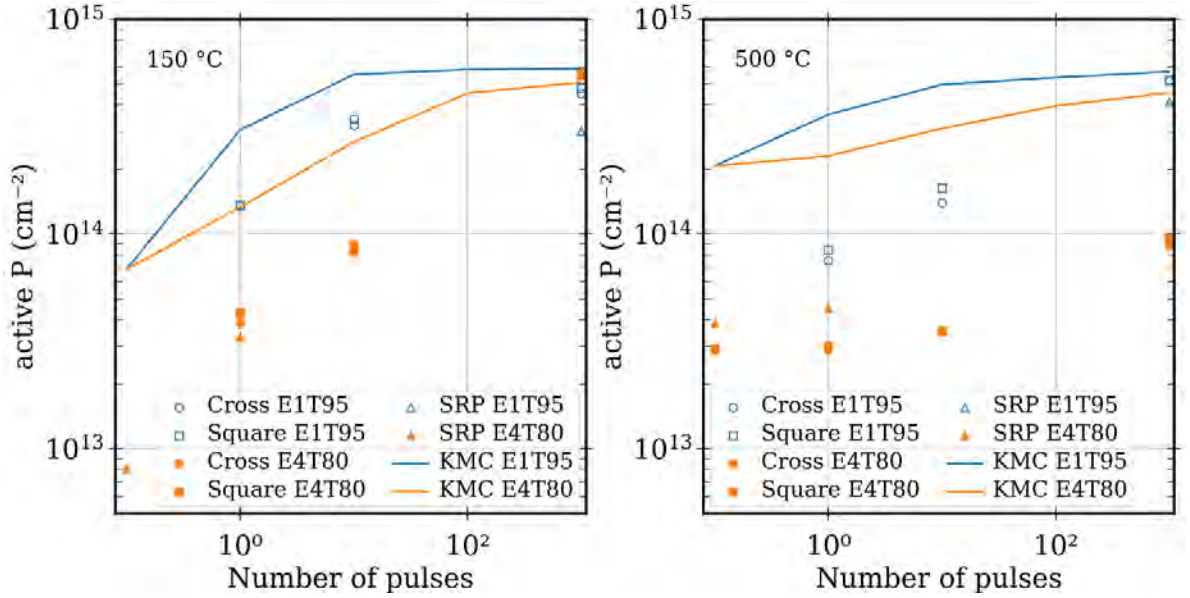

Figure 21: Active P dose as a function of annealing laser pulses for different implant temperatures, and at different laser fluences. Comparison between Hall measurements (Square and Cross van der Pauw structures), SRP measurements, and KMC simulations.

For calibration, the effective diffusivity must remain fixed, similarly as for the case of B implantation. However, since P diffuses not only via P_i but also via P_v the equations governing the different parameters can be adapted from B implantation but must be changed and expanded. The resulting equations are

$$\Delta E_m(P_i^+) = \Delta E_b(P_i^+),$$

$$\Delta E_m(P_i^0) = \Delta E_b(P_i^+) - \Delta e_0(P_i^+),$$

$$\Delta E_m(P_v^+) = \Delta E_b(P_v^+),$$

$$\Delta E_m(P_v^0) = \Delta E_b(P_v^+) - \Delta e_0(P_v^+),$$

$$\Delta E_m(P_v^-) = \Delta E_b(P_v^+) - \Delta e_0(P_v^+) - \Delta e_0(P_v^-).$$

We find that changing the binding energy of P_v^+ or the ionization energies of P_v^+ and P_v^- within reasonable limits only has a minor impact on the P profiles. The effects of changing the two energies for P_i are shown in Fig. 23, where the active P concentration profile is plotted as a function of depth. Here, in the top line the binding energy $E_b(P_i^+)$ is changed and in the bottom line, the ionization energy $e_0(P_i^+)$ is changed, in both cases for implant temperatures of 150 °C (left) and 500 °C (right). SRP data is shown as black dashed curves, and the different KMC datasets are shown as solid lines.

The most significant impact can be seen for an implant temperature of 500 °C, where the local minimum at ~ 15 nm depth becomes more severe by decreasing the binding energy and less severe when increasing the binding energy. Changing the ionization energy has the reverse effect. In addition, decreasing the binding energy slightly increases the depth of the profile at implant temperature 500 °C.

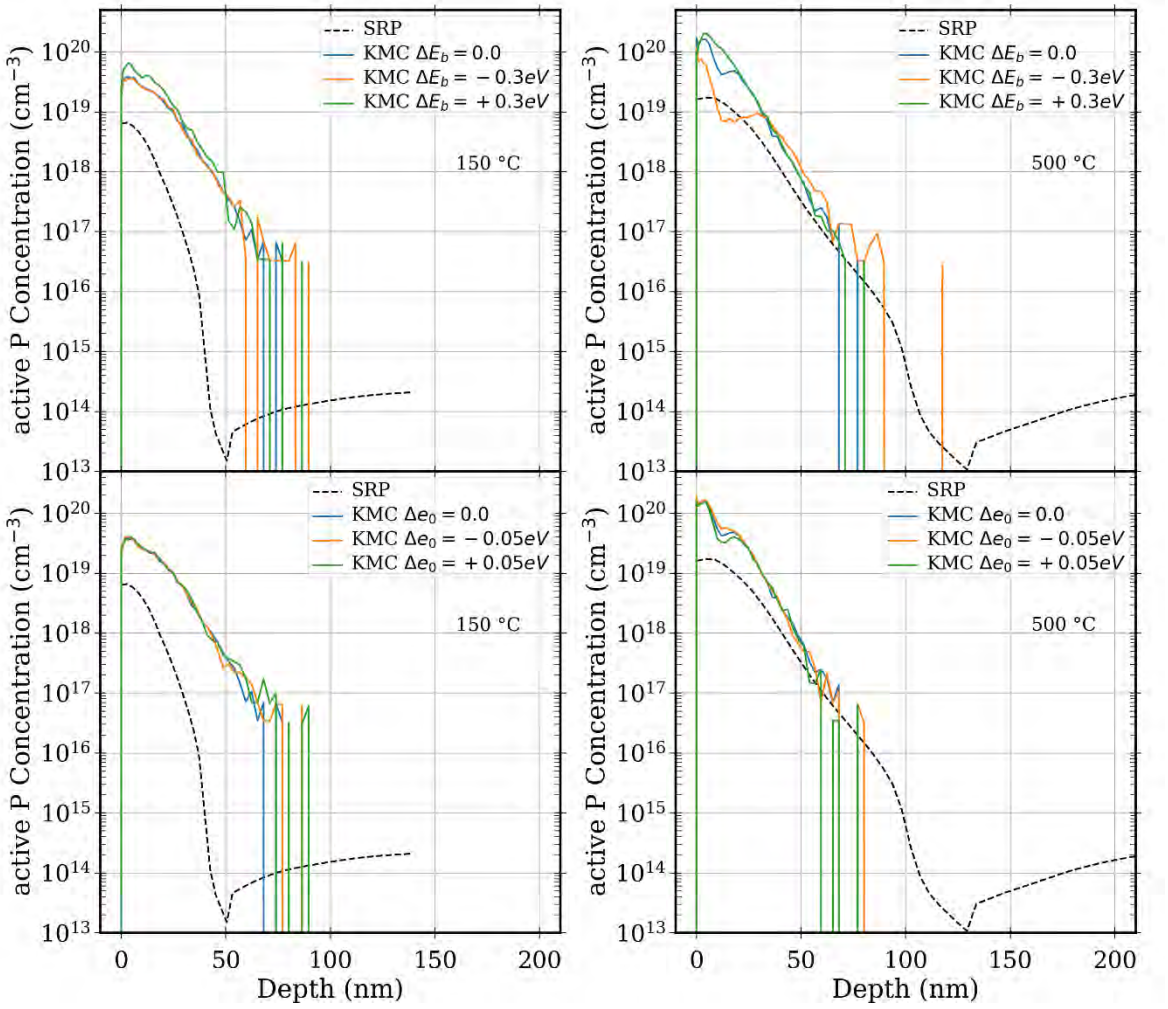

Figure 22: Variations of the P_i related parameters for the as-implanted P profiles at implantation temperatures 150 °C (left) and 500 °C (right). Energy parameters: (top) $E_b(P_i^+)$ and (bottom) $e_0(P_i^+)$.

The best qualitative fit to SRP data is achieved using the values from Tab. 13 for calibration:

Table 13: Parameters for the new calibration that deviate from AdvancedCalibration.

Parameter	Value
$E_b(P_i^+)$	2.03 eV
$e_0(P_i^+)$	0.15 eV
$E_m(P_i^+)$	1.510 eV
$E_m(P_i^0)$	2.055 eV

Note that the other parameters were not changed from the AdvancedCalibration. There are, however, two additional parts to tackle: First, simulation finds that the active profile at 150 °C is slightly deeper than at 500 °C. This indicates that at 500 °C there is less channeling than at 150 °C. This is however not observed in SRP measurements, where the depth increases with temperature. In addition, in Fig. 3 (a) it was demonstrated that implantation at a temperature of 150 °C leads to the formation of a 17.5 nm thick amorphous layer. This of course depends on the dose rate during implantation, which in experiment was set to 1.3×10^{14} $cm^{-2}s^{-1}$. In simulation, however, at this dose rate the amorphous layer is not well reproduced, where no continuous layer is formed. To increase the amorphization during simulation, we slightly increase the dose rate. To account for channeling we are able to tune the proportionality factor casc.amo for the switching probability between amorphous and crystalline model. The effects of changing these two parameters are shown in Fig. 24.

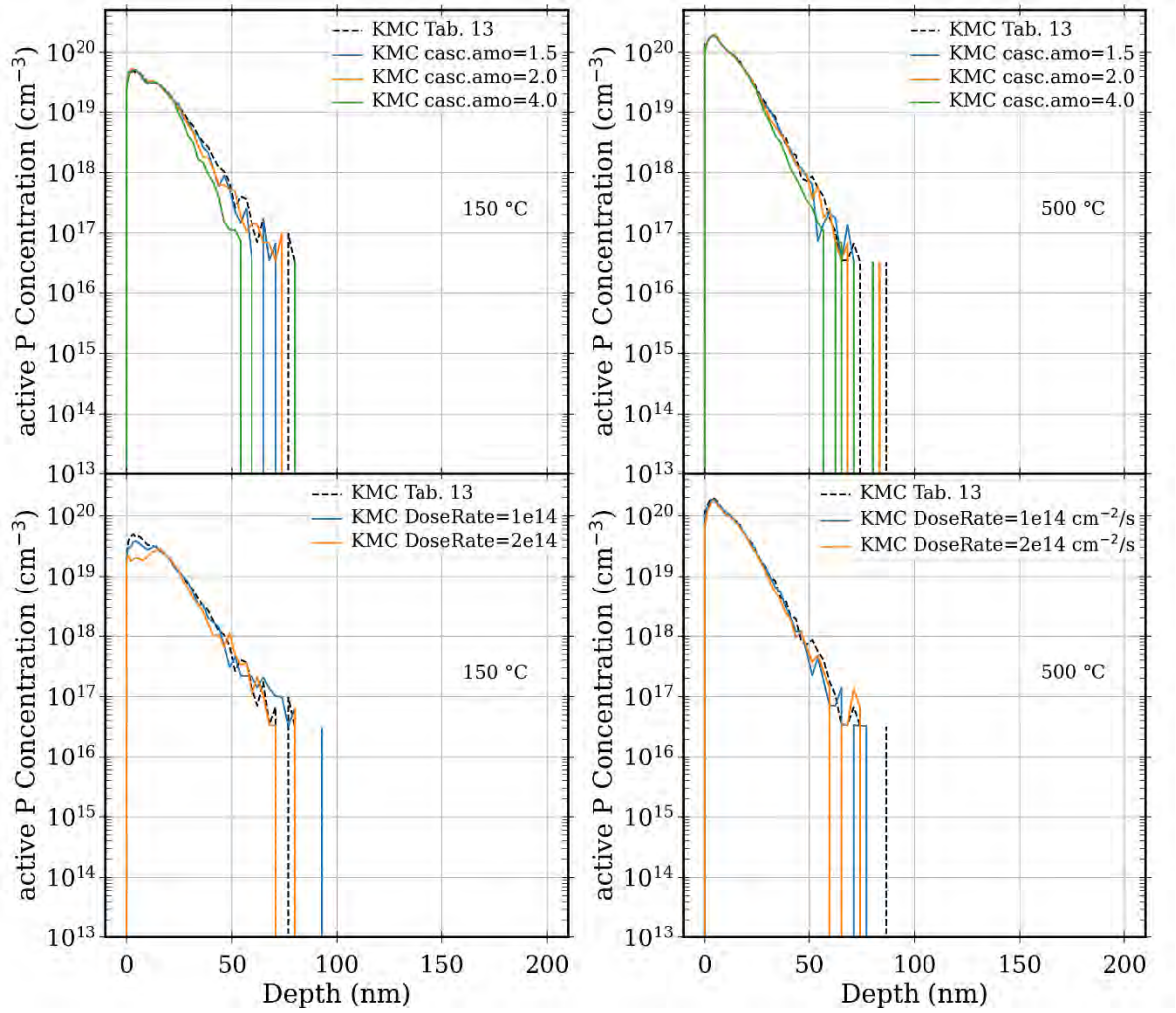

Figure 23: Variations of the proportionality factor casc.amo (top) and the dose rate (bottom) for the as-implanted active P profiles at implant temperatures (left) 150 °C and (right) 500 °C. The black dashed line denotes the values based on the calibration from Tab. 13, with a dose rate of 6 x 10^{13} cm^{-2}/s.

In the top line of Fig. 24, the effect of increasing the proportionality factor casc.amo is shown, while on the bottom line the effect of increasing the dose rate can be seen. Increasing casc.amo reduces the depth of the profile, by increasing the steepness of the decay starting from about 30 nm depth. This effect is stronger for the lower implant temperature. When changing the dose rate, the tails are not impacted, instead the position of the profile's peak is

shifted to larger depths for the implant temperature 150 °C, while for 500 °C the profile is essentially unchanged. This is due to an amorphous layer forming at 150 °C, as can be seen in TEM images. It should be noted that SRP profiles do show the peak at shallow depths as if there was no amorphous layer, meaning there is a clear disagreement in experimental data and more experimental investigations would be needed.

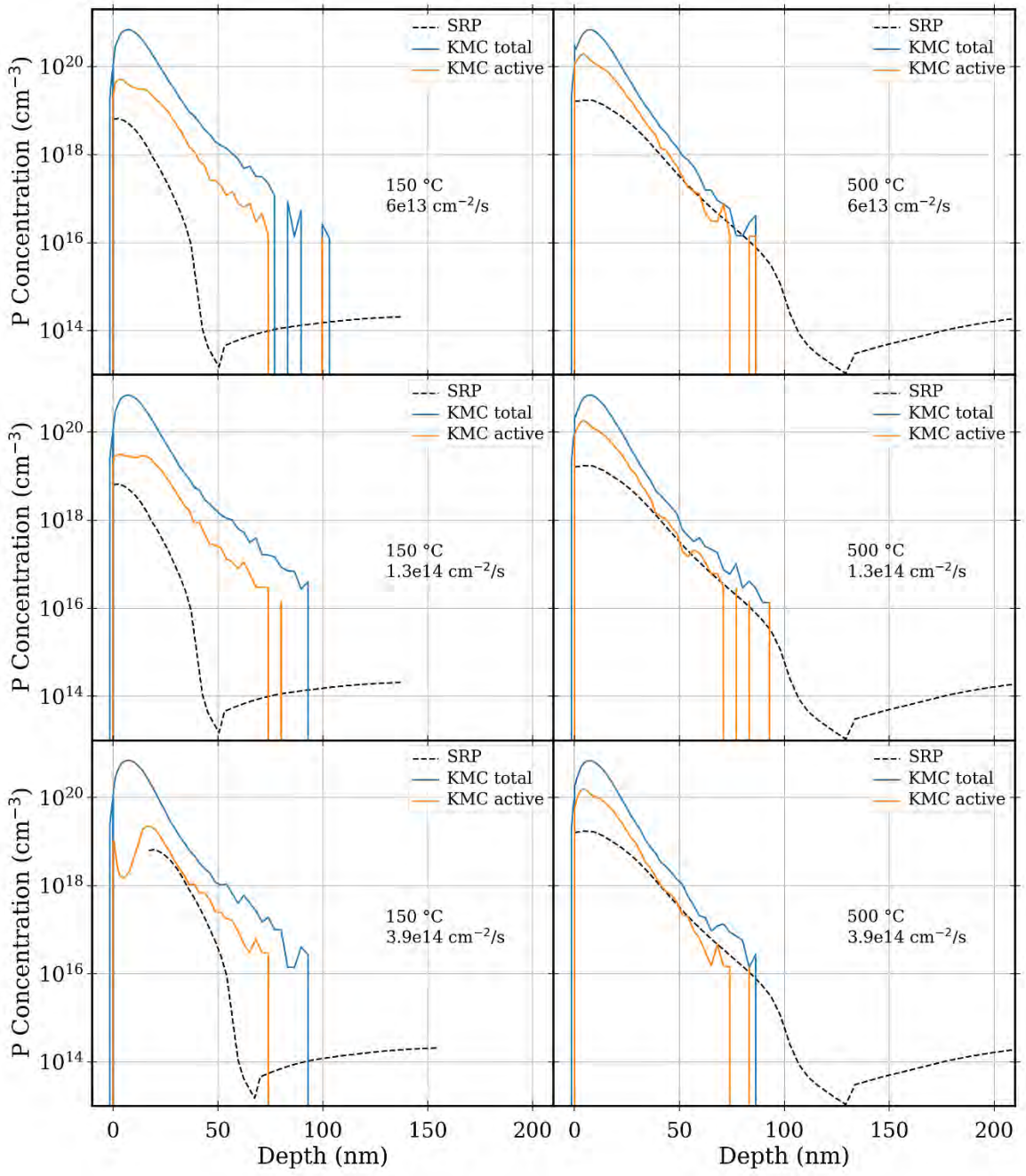

Figure 24: Comparison between SRP measurements and KMC simulations for the as-implanted chemical and electrical P profiles at implant temperatures (left) 150 °C and (right) 500 °C and simulated dose rates of (top) 6.5×10^{13} cm^{-2}s^{-1}, (middle) 1.3×10^{14} cm^{-2}s^{-1}, and (bottom) 3.9×10^{14} cm^{-2}s^{-1}. Note that the SRP profiles shown for the different dose rates are the same, taken from a sample that was implanted with an average dose rate of 1.3×10^{14} cm^{-2}s^{-1}. For the case of 150 °C and simulated dose rate of 3.9×10^{14} cm^{-2}s^{-1}, the SRP profile was shifted 17 nm to the right, to take into account the amorphous layer visible in the TEM picture, Fig. 3.

Nevertheless, we show a comparison between SRP results and three possible calibrations in Fig. 25. One is for the case where no amorphous layer is formed, the second shows the dose

rate that is used in experiment, where some amorphization is visible, but no complete layer is formed, and the third is for simulated dose rates where an amorphous layer is formed. In all cases the parameter casc.amo was set to 3.0, while for the case of no amorphous layer the dose rate was set to 6.5×10^{13} $cm^{-2}s^{-1}$ and a dose rate 3.9×10^{14} $cm^{-2}s^{-1}$ was used to reach an amorphous layer of comparable thickness to that found in the TEM image in Fig. 3.

It should be noted that the dose rate for the samples measured by SRP did not change, the dose rates given in Fig. 25 are only used as parameters within the KMC simulations. For the case of 150 °C and a simulated dose rate of 3.9×10^{14} $cm^{-2}s^{-1}$, the SRP profile was shifted 17 nm to the right to account for the amorphous layer and give better comparability between the SRP results and KMC simulations. For the case of the high dose rate, we find that also KMC predicts an amorphized layer at 150 °C leading to a shift in the active profile's peak. For this case we can also see, that both implant temperatures behave similarly, the peak is higher than measured with SRP, but the slope of the decay is then rather well reproduced, just as the profile's depth is rather well resolved. And, while there is not much difference between the profiles simulated at different dose rates for 500 °C, for 150 °C the simulation at lower dose rate predicts a significantly higher activation than what is measured in SRP. Finally, the case of a dose rate 1.3×10^{14} $cm^{-2}s^{-1}$, is an intermediate case, where a plateau in the active P profile is visible, for the first 20 nm. This is due to the existence of some amorphous areas, but the lack of a full amorphous layer.

3 SPER model in Sentaurus Process KMC

Sentaurus Process KMC implements three different models for the simulation of SPER controlled by the command "`pdbSet <material> KMC Damage SPER.Model <model>`":

- An off-lattice KMC model (`KMC`) which assigns a recrystallization rate of each amorphous element. This model features no orientation dependence; therefore, it is of limited interest for the simulation of low temperature processes.
- A basic on-lattice KMC model (`LKMC`) based on Ref. [22] which includes an orientation dependence to capture regrowth anisotropy.
- A more advanced on-lattice KMC (`Coordinations.Planes`) which takes into account local atomic configurations, similarly to the `Coordinations.Reactions` LKMC epitaxy model used in WP3.

For the simulation of low temperature processes, we typically use one of the two LKMC models available. These models take into account:

- Anisotropic growth and defects formation
- The Ge content dependence of the SPER rate
- The impact of stress (based on Ref. [23])
- Dopant activation during SPER and their impact on the regrowth velocity

3.1 SPER in undoped SiGe alloys

The calibration of orientation-dependent recrystallization LKMC events has been addressed in previous works (see Ref. [22, 24]). In the frame of WP2, we investigated the SPER LKMC model predictions of SiGe(001) alloys and we found that the advanced calibration is in

reasonable agreement with available experimental data (see deliverable D2.3). Unfortunately, no experimental data is available for other orientations.

3.2 SPER in doped SiGe alloys

The three SPER models implemented in Sentaurus Process KMC share the same description of dopant activation and their impact on SPER rate. The regrowth rate r is affected by the presence of dopants by introducing some corrections to the model for an undoped material:

$$r = r_{fermi} \times r_0 \times \exp\left(-\frac{E_a + c}{k_B T}\right),$$

where r_0 and E_a are the model-dependent prefactor and the activation energy for an undoped material, respectively, and:

$$r_{fermi} = 1 + |K \times Doping|$$

and c taking into account the local impurity concentration given by the empirical expression [1]:

$$c = \sum_{Impurities} \left(E_f(impurity) - E_a\right)\left(\frac{[impurity]}{5 \times 10^{22}}\right)^x,$$

where K, $E_f(impurity)$ and x are calibration parameters:

- K is set by the `V0.Recryst.ntype` and `V0.Recryst.ptype` parameters
- $E_f(impurity)$ is set by the `E.Recryst` parameter
- x is set by the `E.Recryst.Exponent` parameter

During SPER the dopants present in the amorphous phase can become active, form clusters or precipitates or move with the recrystallization front (snowplow effect). These effects are included in the SPER model using a phenomenological description (see Ref. [25]) which makes a general calibration of these parameters very challenging.

A more physical approach could be employed to include a dopant segregation model at the amorphous/crystalline interface, in the same spirit as in a phase field model but this is not possible in Sentaurus Process KMC at the moment. Thus, the development of specific models for the simulation of dopant effects has not been considered in WP2.

4 Silicidation

4.1 Silicide structures and thermodynamic phase diagram of the Si-X system, where X=Ni/Pt

According to thermodynamic phase diagrams at standard pressure, Si-X systems (with X=Ni or Pt) can be stabilized in different crystal phases on the basis of the temperature and the composition (see as an example the literature Ni-Si phase diagram and *ab-initio* assessed crystal structures in Fig. 26). We notice that for the solid compounds, apart from reduced regions of the temperature-composition variable (e.g., low Si weight % where the Ni-Si alloy phase is stable in Fig. 26), the phase diagram is dominated by the co-existence of phases, where the mixture of Si and metal should be separated in space domains (domain

decomposition phenomena) of phases/compounds present at the boundary of the co-existence region (e.g., a mixture of 20% Ni and 80% Si at T < 993 °C should form Si and $NiSi_2$ compounds conserving the composition at the mesoscopic/macroscopic level).

The crystal structures of the silicide phases can be characterized by a complex network of bonding which changes from one phase to another (see left panel of Fig. 26). In this condition, a limited number of phases (for example the Ni-Ni_3Si-Si system presented in the deliverable D2.2 or the $NiSi_2$-Si system whose crystals show a nice commensuration) can be modelled with the same fully atomistic Lattice Kinetic Monte Carlo scheme even using the super lattice formulation. However, in order to develop a flexible, stochastic kinetic simulation scheme able to potentially simulate all the silicide compounds, here we consider the Pott “in cell” lattice approach as a baseline which, as we will discuss in the following, after a suitable extension allows for the accommodation of all phase variables and local compositional changes.

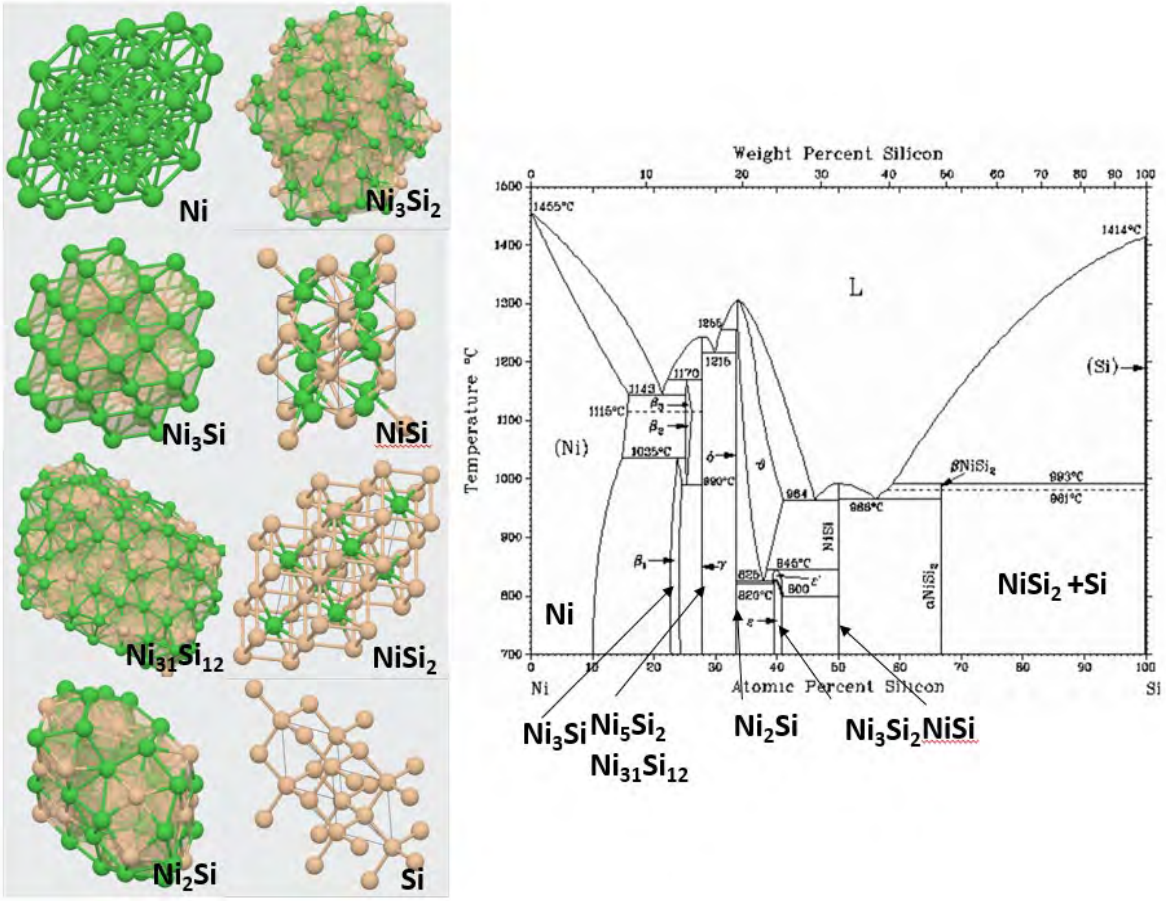

Figure 25: (left) Ab-initio assessed crystal structures for the Ni-Si silicide. Figures extracted by The Materials Project web page (https://materialsproject.org). (right) Thermodynamic phase diagram of the Ni-Si binary system at standard pressure form Ref. [26]. Boundaries in the co-existence region for the stability of different compounds are indicated.

4.2 Modified Pott model for silicide formation

4.2.1 From single-phase to multi-phases Pott-like models: role of the stoichiometry

The evolution of a nano- polycrystalline single-phase material during a thermal process can be efficiently simulated by means of cellular automata approaches (see e.g., Ref. [27] and references therein) allowing a realistic description of the crystal domains (grains) re-configuration kinetics through a stochastic sequence of local transitions of the volume "cells" in a three-dimensional lattice where the polycrystalline structure is mapped. The single cell represents a volume portion of the material and in the standard formulation it stores an integer value correlated to the orientation variable of the volume itself. Optionally a particular value of this variable could also be assigned to the monomers, when the volume is filled by monomers only.

The local event promoting the polycrystal evolution is the status change of the cells which can modify their orientation, at a given time t_0 of the evolution, to another one among the total number N_{orien} of possible orientations; it is characterized by a transition probability (rate) which is ruled by the local energy barrier ΔE according to the transition state theory.

The "potential" transition rate is

$$R = \begin{cases} \omega \; if \; \Delta E \leq 0 \\ \omega \exp\left[-\dfrac{\Delta E}{kT}\right] \; if \; \Delta E \geq 0 \end{cases} \tag{4}$$

The energy barrier for the volume reconfiguration is calculated by the following (Pott-like [28]) lattice energy model

$$E(\theta_i) = J(\theta_i) \sum_{nn} [1 - \delta(\theta_i, \theta_{nn})] \tag{5}$$

where $\theta_i = \alpha, \beta, \gamma \ldots$ is the "orientation" of the volume in the i-th cell, $J(\theta_i)$ the grain boundary (or the monomer-grain) energy cost, θ_{nn} is the orientation of the next neighbor cell in the lattice and δ is the usual discrete delta function. We note that the energy in the bulk of the grain is the reference energy since $E(\theta_i) = 0$ for a cell which has all the neighbors with the same orientation. $J(\theta_i)$ is a calibration function which for homogenous materials is chosen in a way that the model recovers the correct melting transition at the melting temperature T_m. Moreover, by means of a fine tuning of $J(\theta_i)$, orientation penalty, epitaxial or similar interface dependent energy modification could also be effectively included in the model. We notice that all the Pott-like models are integrated in a version of MulSKIPS under development (not yet the official one).

The melting transition for the homogeneous Pott model $J(\theta_i) = J = cost$ and which does not allow the transition to isolated cells with 0 coordination is obtained for $J/kT_m = 0.5$ in the large orientation variable limit (convergency to this value is obtained for few tens of orientations). For the extension which we will discuss in the following the transition to isolated cells must be allowed in order to account for the nucleation of different silicide compounds. Moreover, a reduced number of orientations variable is considered to effectively model nano-crystalline materials. In this case a different value of J/kT_m is obtained also for the pure Pott model.

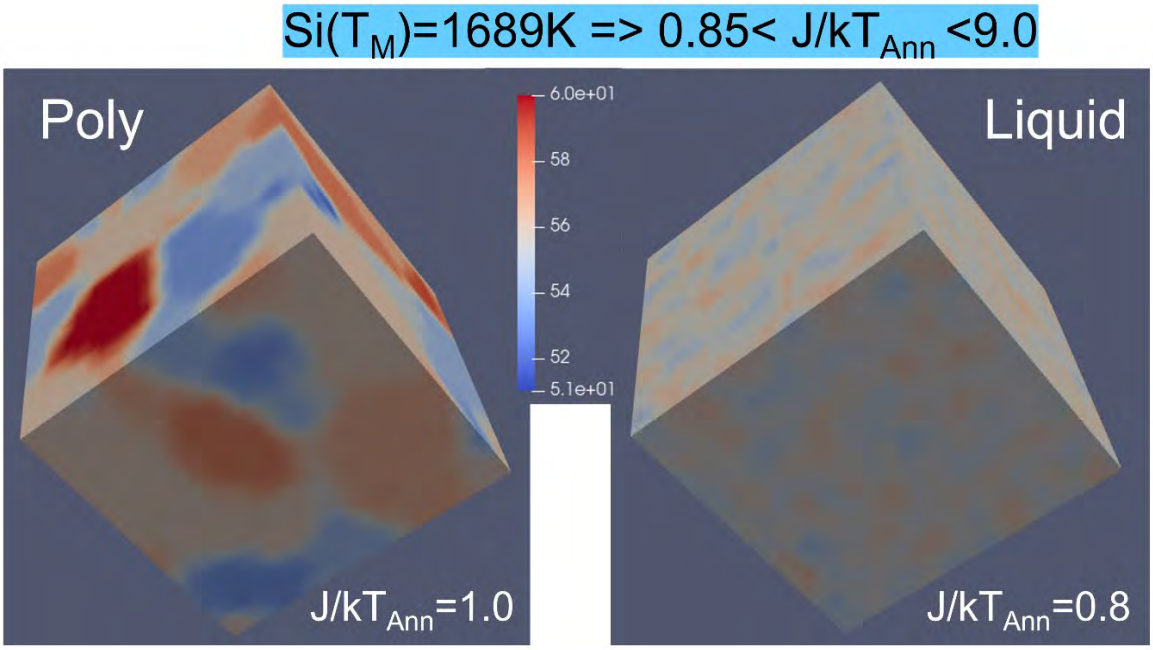

Figure 26: Snapshots of grain densification (left) and melting (right) for a q-10 Pott model (modelling e.g., pure Si poly-material with orientation indexes 51-60; see color scale). The evolution occurs in a bulk volume prepared as an initial "ideal" nano-crystalline material (cubic and equal sized nanograins with volume ≈ (2.7x2.7x2.7) nm^3). The system size is a cube of about 33x33x33 nm^3 with periodic boundary conditions. The poly case evolves to a single grain (bulk) for large times, while the cells' orientations fluctuate with time in the liquid case.

For example, a sharp transition is simulated in the interval $0.85 < J/kT_{ann} < 0.9$ for a q=10 Pott model allowing isolated cell transitions (see Fig. 27).

The generalization of the in-cell single phase model to a multi-phase system can be obtained introducing blocks of q-states for each phase of the system. For example, for the Ni-Si system we can consider the following 8 phases: Ni, Ni_3Si, $Ni_{31}Si_{12}(Ni_5Si_2)$, $Ni_2Si, Ni_3Si_2, NiSi$, $NiSi_2$, Si and the related orientation variables

$$\{\theta_i(Ni)\} = \alpha(Ni), \beta(Ni), \gamma(Ni) \dots$$

$$\{\theta_i(Ni_3Si)\} = \alpha(Ni_3Si), \beta(Ni_3Si), \gamma(Ni_3Si) \dots$$

$$\{\theta_i(Ni_{31}Si_{12})\} = \alpha(Ni_{31}Si_{12}), \beta(Ni_{31}Si_{12}), \gamma(Ni_{31}Si_{12}) \dots$$

$$\{\theta_i(Ni_2Si)\} = \alpha(Ni_2Si), \beta(Ni_2Si), \gamma(Ni_2Si) \dots$$

$$\{\theta_i(Ni_3Si_2)\} = \alpha(Ni_3Si_2), \beta(Ni_3Si_2), \gamma(Ni_3Si_2) \dots$$

$$\{\theta_i(NiSi)\} = \alpha(NiSi), \beta(NiSi), \gamma(NiSi) \dots$$

$$\{\theta_i(NiSi_2)\} = \alpha(NiSi_2), \beta(NiSi_2), \gamma(NiSi_2) \dots$$

$$\{\theta_i(Si)\} = \alpha(Si), \beta(Si), \gamma(Si) \dots$$

While for the Pt-Si system, the following 6 phases: Pt, Pt_2Si, $Pt_6Si_5, PtSi$, Pt_2Si_3, Si and the related orientation variables can be reliably integrated in the model

$$\{\theta_i(Pt)\} = \alpha(Pt), \beta(Pt), \gamma(Pt) \dots$$

$$\{\theta_i(Pt_2Si)\} = \alpha(Pt_2Si), \beta(Pt_2Si), \gamma(Pt_2Si) \dots$$

$$\{\theta_i(Pt_6Si_5)\} = \alpha(Pt_6Si_5), \beta(Pt_6Si_5), \gamma(Pt_6Si_5) \dots$$

$$\{\theta_i(PtSi\,)\} = \alpha(PtSi), \beta(PtSi),\ \gamma(PtSi)\ \ldots$$

$$\{\theta_i(Pt_2Si_3\,)\} = \alpha(Pt_2Si_3), \beta(Pt_2Si_3),\ \gamma(Pt_2Si_3)\ \ldots$$

$$\{\theta_i(Pt\,)\} = \alpha(Pt), \beta(Pt),\ \gamma(Pt)\ \ldots$$

We notice that the sole inclusion of the phase dependency in the Pott-like energetic dependency (5) is not sufficient to recover the composition dependency of the silicidation reaction path. Indeed, for any possible model calibration, the time dependent simulations in the canonical ensemble (at a suitable fixed temperature T that is lower than the decomposition/melting temperature) will result in the emergence of phases/orientations with the highest value of $\theta_i(X)$.

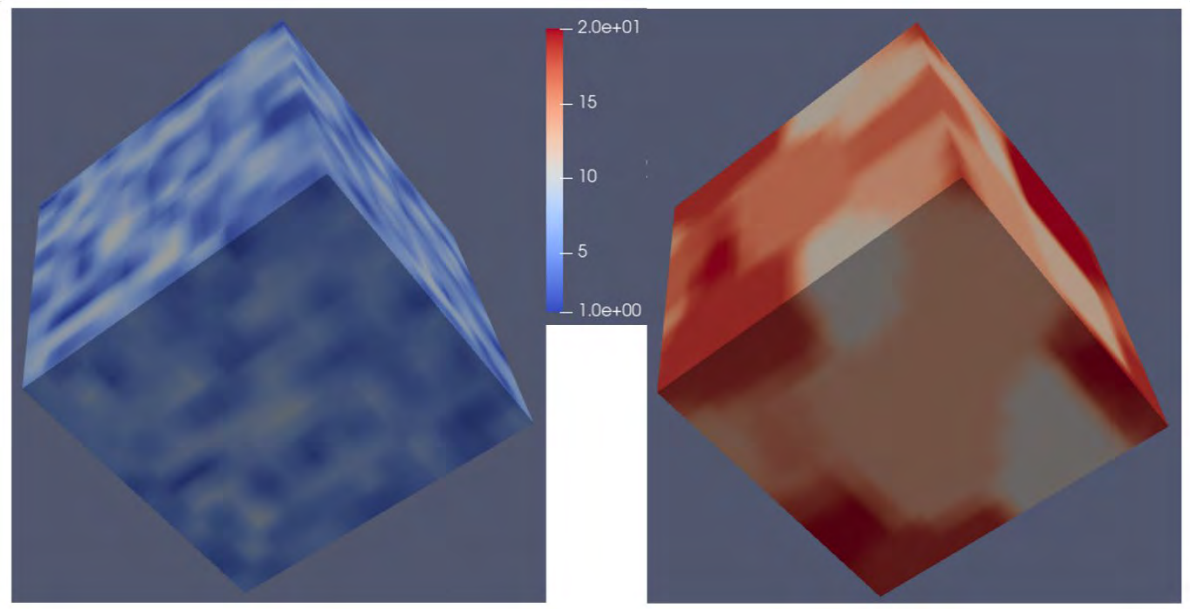

Figure 27: Snapshots of a Pt to Pt₂Si volume transition: (left) initial Pt state and (right) Pt₂Si state. The simulation is performed with a stoichiometry corrected Pott model for the 6 Pt-Si silicide phases with 10 orientation variables for each phase (1-10 indexes Pt, 11-20 indexes Pt₂Si; see color scale) parameters are reported in Tab. 14. The evolution is simulated in a bulk volume prepared as an initial "ideal" Pt nano-crystalline material (cubic and equal sized nanograins with volume ≈(2.7x2.7x2.7)nm³), with the "wrong" cell stoichiometry for the Pt₂Si phase (with Si insertion). The system size is a cube of about 33x33x33 nm³ with periodic boundary conditions and the temperature is $J/kT_{ann} = 1.0$. After a transition in a nano-crystalline configuration, the Pt₂Si case evolves to a single grain (bulk) for large times.

We should first extend this generalized Pott model to consider the impact of local stoichiometry in the KMC transition rate. In order to include the stoichiometry dependency, we introduce for a binary system a probability weigh matrix $P_{st}(-s1_{max}{:}s1_{max}; -s2_{max}{:}s2_{max})$ (with $P(0;0) = 1$) which is related to the deviation with respect to the ideal stoichiometry of the 1st-atom $s1 \in [-s1_{max}{:}s1_{max}]$ and the 2nd-atom $s2 \in [-s2_{max}{:}s2_{max}]$ of the phase θ_{nn} achievable with a transition. The stoichiometry corrected transition rate is:

$$R = \begin{cases} \omega P_{st}(s1;s2)\ \ if\ \Delta E \le 0 \\ \omega P_{st}(s1;s2)\ \ exp\left[-\dfrac{\Delta E}{kT}\right]\ \ if\ \Delta E \ge 0 \end{cases} \qquad (6)$$

where $\Delta \boldsymbol{E}$ is calculated again with expression (5). In the preliminary calibration we fix the following expression for $P_{st}(s1;s2)$

$$P_{st}(s1;s2) = exp\left[-\frac{|s1|E_{s1} + |s2|E_{s2}}{kT}\right] \quad (7)$$

which hinders both over-stoichiometry and under-stoichiometry in the cell for the two atoms. In Figs. 28 and 29 we can observe the impact of the corrected Pott model in the stoichiometry (through phase transitions and grain densification) of two limiting cases, where the initial state is assumed as a Pt (Pt_2Si) ideal nanocrystalline material with the stoichiometry of Pt_2Si (Pt) phase. Of course, we notice that thanks to the stoichiometry penalty in the Pt_2Si => Pt case the transition takes place despite the larger value of $J[\theta_i(Pt_2Si)]$ considered in the calibration.

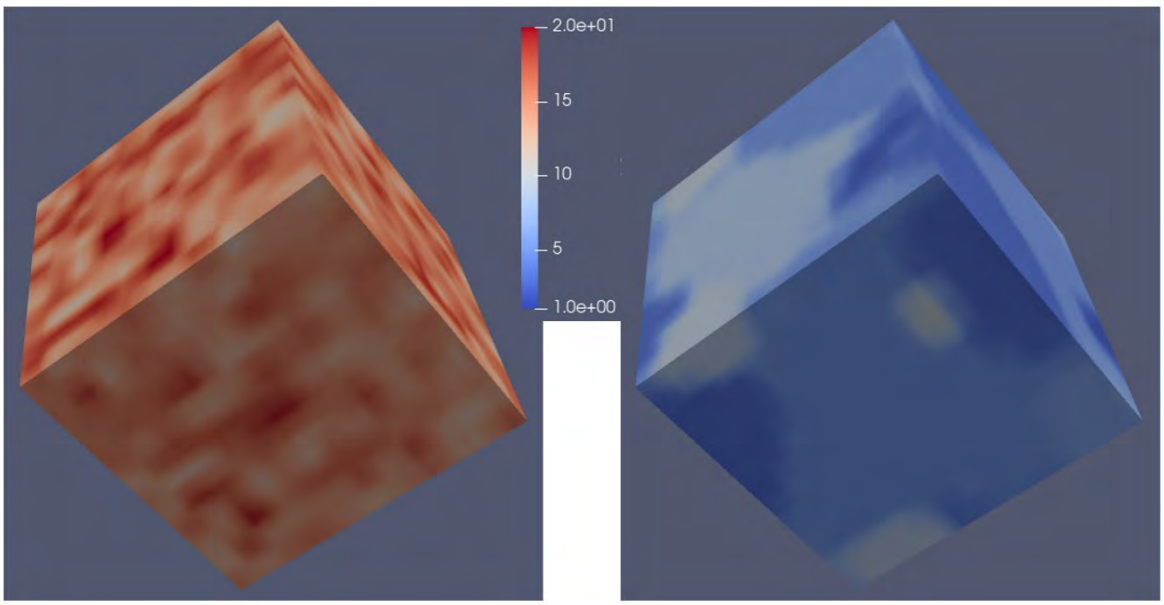

Figure 28: Snapshots of a Pt_2Si to Pt volume transition: (left) initial Pt_2Si state and (right) Pt state. The simulation is performed with a stoichiometry corrected Pott model for the 6 Pt-Si silicide phases with 10 orientation variables for each phase (1-10 indexes Pt, 11-20 indexes Pt_2Si; see color scale). Parameters are reported in Tab. 14. The evolution is simulated in a bulk volume prepared as an initial "ideal" Pt_2Si nano-crystalline material (cubic and equal sized nanograins with volume ≈(2.7x2.7x2.7)nm^3), with the "wrong" cell stoichiometry of the Pt phase (no Si). The system size is a cube of about 33x33x33 nm^3 with periodic boundary conditions and the temperature is $J/kT_{ann} = 1.0$. After a transition in a nano-crystalline configuration, the Pt case evolves to a single grain (bulk) for large times.

4.2.2 Reactive boundaries, diffusing atoms and intermixing

Although a fully atomistic picture of the silicidation processes has not been achieved it is clear (see D2.2, D2.4, D2.5) that the transformations from one phase to another are driven by (successive) intermixing stages with reactive boundary regions lacking a clear phase character (e.g., high deviation of pristine stoichiometry and/or pseudo amorphous phase) between two bulk phases. Therefore, dynamic modification of the local stoichiometry and the possibility to model atomic diffusion (including the interstitial – vacancy components in the bulk phases) should be considered in the model formulation.

We further extend the Pott scheme with additional cell variables which can be also linked to a full atomistic description as the one obtained in the super-lattice formalism (D2.3) or with Molecular Dynamics simulations. These additional in-cell variables are

- n_{diff} = number of weakly bonded atoms in the cell, which can diffuse by random jumps to neighbours' cells

- n_{crys}= number of strongly bonded atoms which are in correct bonding configuration with respect to the cell phase θ

The variable n_{crys} is related to the stoichiometry deviation $sX = n_{crys}X - s_{ideal}X(\theta)$ of the $X = 1,2$ atom where the ideal stoichiometry $s_{ideal}X(\theta)$ depends on the phase θ of the cell. With these cell variables we consider two additional evolution steps with respect to traditional Pott transition rates

- Activation of strongly bonded atoms to diffusing components $R_{X-Cry-Diff}\ (sX; nn)$
- Next neighbor random jumps (diffusion) of weakly bonded (diffusing) atoms $R_{jump}\ (ni_{diff}, nj_{diff}; nni, nnj)$ and deactivation of the diffusing component
- Intermixing (one atom exchange between next neighbor i,j cell) with a species dependent rate $R_{intermix}(\theta_i(X))$ for $ni_{crys} > nj_{crys} + 1$ and $R_{intemix}(\theta_i(X))\exp(-k_{mix}\theta_i(X)J/kT_{ann})$ for $ni_{crys} = nj_{crys} + 1$

In the preliminary calibration we fix the following expression for $P_{X-Cry-Diff}(sX; nn)$

$$R_{X-Cry-Diff}(sX; nn) = \begin{cases} 0 \quad \text{if } nn = 6 \text{ and } sX \leq 0 \\ R_{Cry-Diff-bulk}\left(\theta_i(X)\right) \quad \text{if } nn = 6 \text{ and } sX > 1 \\ R_{Cry-Diff}\left(\theta_i(X)\right) exp\left[-\dfrac{nn \times E_{coor} - (sX - 1) \times E_{CD_X}}{kT}\right] \quad \text{otherwise} \end{cases} \tag{7}$$

which allows for the transition off cells in the grain boundary region with coordination dependent exponential weight, favoring the achievement of the ideal stoichiometry of the phase in the cell. The following expression is used for $R_{jump}\ (sXi, sXj; nni, nnj)$

$$R_{jump}\ (sXi, sXj; nni, nnj) = R_{jump}(\theta_i(X)) exp\left[-\frac{(sXj - sXi) \times E_{diff1} + (nnj - nni) \times E_{diff2}}{kT}\right] \tag{8}$$

and

$$R_{jump}\ (sXi, sXj; nni, 6) = 10^{-3} \times R_{jump}\ (sXi, sXj; nni, nnj) \tag{9}$$

This hinders the diffusion toward cells with larger stoichiometric deviation or higher coordination with a further penalty for jumps toward bulk cells. A Metropolis-type algorithm [29] governs the acceptance of the diffusion jumps. A fixed portion of the diffusing atoms are promoted to crystal atoms increasing the n_{crys} variable in the cell; therefore, the stoichiometry control is only ruled by $R_{X-Cry-Diff}$.

The monomer inclusion and the removal of the diffusing atoms from the cells' stoichiometry evaluation alter further the Pott model behavior with respect to the analysis discussed in the previous subsection. As an example, in Fig. 30 we show a snapshot of the grain densification of a pure Si nano-crystalline system starting from a similar ideal one (see Fig. 27) with the same parameter value $J/kT_{ann} = 1$ on the left panel in the same figure ("High C=>D" parameter choice in Tab. 16). In this case the densification occurs in the presence of monomer evolution and local stoichiometry variation in the cells (see bottom row of snapshots in Fig. 30). For the temperature and the calibration parameters here considered (see Tab. 14) we can

notice an over stoichiometry in the grain boundary region and a fluctuating stoichiometry which tends to zero on average in the bulk of the grains. Anyhow, the impact of these model features in terms of the melting transition is minor. Indeed, we simulate for the pure Si material a sharp modification of the model behavior (namely a Pott-like solid-liquid transition) in the interval $0.9 < J/kT_{ann} < 0.95$ instead of the $0.85 < J/kT_{ann} < 0.9$ interval estimated with the Pott model (see Fig. 31).

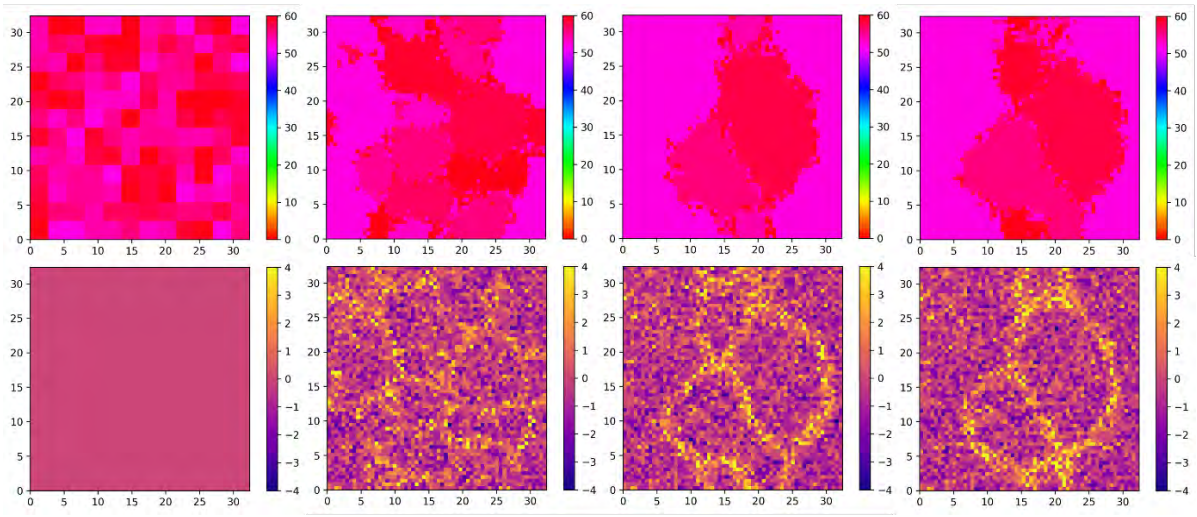

Figure 29: Snapshots of a grain densification of Si material simulated with the full Pt-Si silicide model with 6 Pt-Si silicide phases and 10 orientation variables for each phase (51-60 indexes Si). Parameters are reported in Tab. 14. The evolution is simulated in a bulk volume prepared as an initial "ideal" Si nano-crystalline material (cubic and equal sized nanograins with volume ≈(2.7x2.7x2.7)nm^3). The system size is a cube of about 33x33x33 nm^3 with periodic boundary conditions and the temperature is $J/kT_{ann} = 1.0$. The nano-crystalline configuration evolves to a single grain (bulk) for large times. (bottom) Deviation of the local correct stoichiometry of the Si element in a section along the (010) direction at the simulation box center. This parameter is evaluated as the atomic deviation of the Si element atoms with respect the number of atoms (8) present in the conventional crystal cell of the corresponding phase (see corresponding color scale in the middle row sequence). ±4 atoms deviation is allowed in the calibration used here. We notice that this parameter tends to achieve the 0 average value in the bulk of the grains although fluctuations are possible from cell to cell, while a clear average positive deviation is observed in the grain boundaries' regions.

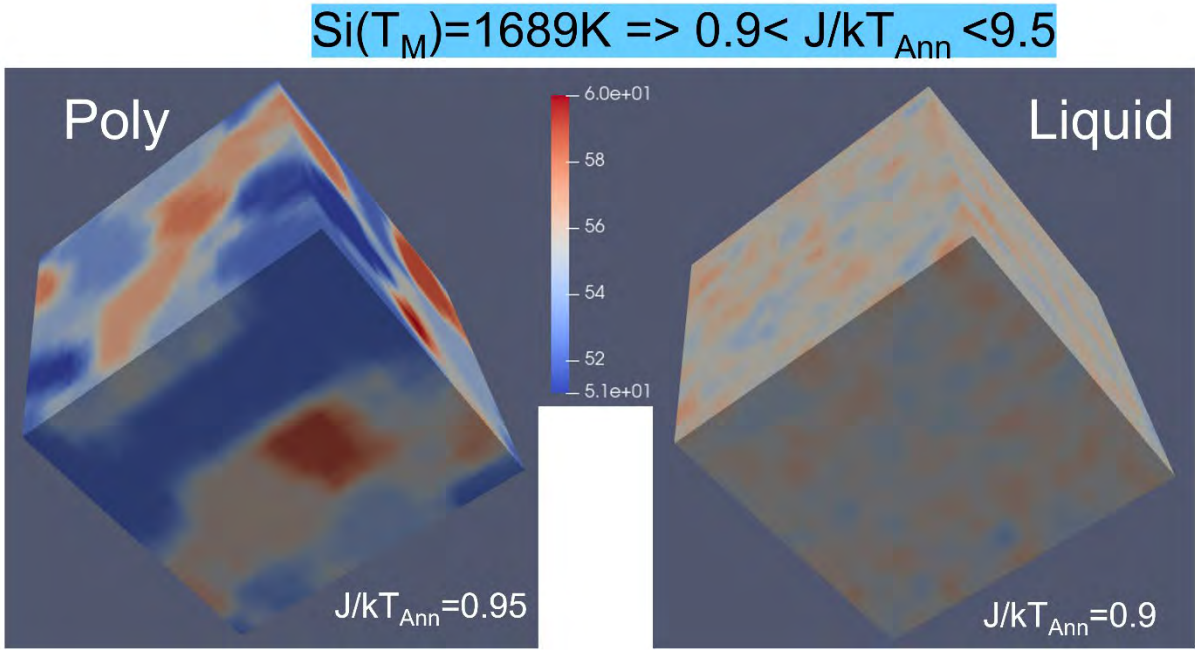

Figure 30: Snapshots of grain densification (left) and melting (right) for the full model for a pure Si poly-material with orientation indexes 51-60 (see color scale). The evolution occurs in a bulk volume prepared as an initial "ideal" nano-crystalline material (cubic and equal sized nanograins with volume ≈(2.7x2.7x2.7)nm^3). The system size is a cube of about 33x33x33 nm^3 with periodic boundary conditions. The poly case evolves to a single grain (bulk) for large times, while the cells' orientations fluctuate with time in the liquid case.

We finally notice that the melting evaluation of a single phase is important as consistency check of the Pott model extensions implemented. Indeed, for the full model experimental melting point of the phases cannot be used to derive the different $J\{\theta_i(X)\}$ Pott constants for the X phases. This derivation is hindered by the equal entropic contribution for the phases in the Pott scheme, whilst entropy differently impacts the solid-liquid equilibration in elements and compounds (see discussion in the next sections).

4.3 Calibration from the *ab-initio* energetics and simulation results

The behavior of the extension of the Pott model presented in the previous section depends critically on the parameter settings. The model calibration is particularly difficult sincedespite the abundancy of the experimental literature in the field, there are not sufficient dedicated ad-hoc studies to address the kinetic evolution in simplified conditions that allow access to the separate interactions and phenomena controlling the silicidation.

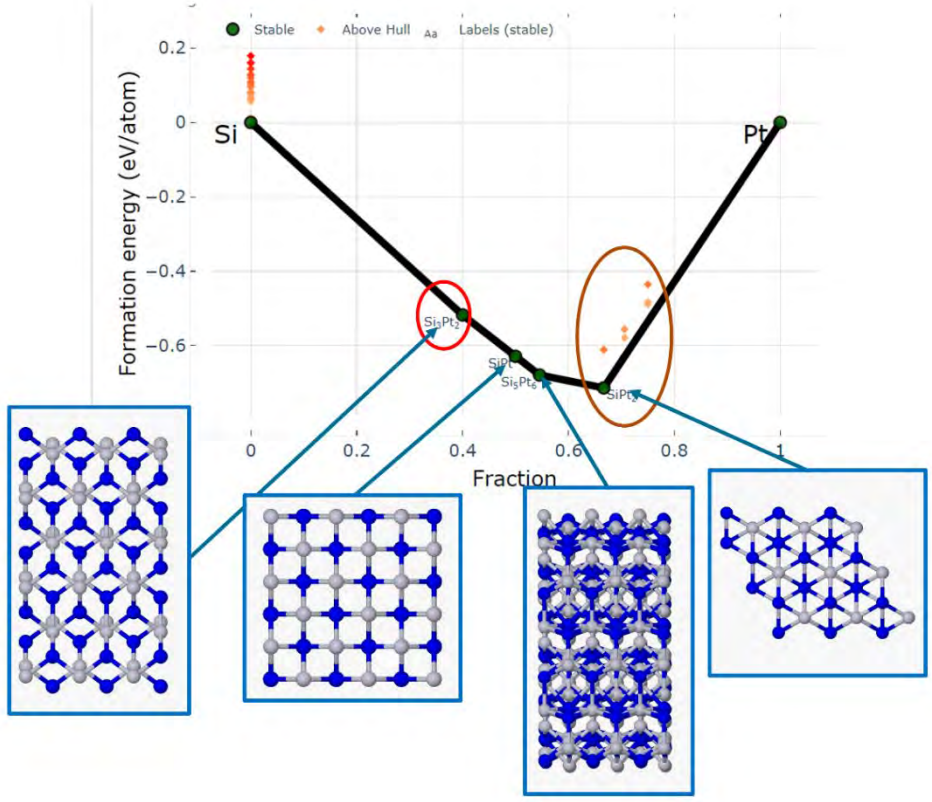

Figure 31: Formation energy for relevant Pt-Si crystal structures as a function of the Pt fraction extracted by The Materials Project web page (https://materialsproject.org) and correlated with the silicide crystal atomic arrangement. We notice that several structures (brown line) in the Pt rich region are above the Hull stability level but are present in the Pt-Si experimental phase diagram at standard pressure, while the Pt_2Si_3 (red line), which is within the Hull stability rule, is not reported in the Pt-Si experimental phase diagram.

However, a preliminary assessment of the Pott constants $J\{\theta_i(X)\}$ can be attempted noticing that they are related to the relative bulk stability of the different phases. As a consequence, we can use the computed formation energy of the silicide phases to get a first estimate of the $J\{\theta_i(X)\}$ parameters. The formation energy in the neutral state of a silicide compound X_nSi_m is evaluated by means of first principles methods with the expression:

$$E_{form}\ (X_mSi_n)\ = E_{tot}\ (X_mSi_n) - N_{units}\ (m\ \mu_X + n\ \mu_{Si}) \qquad (10)$$

where $E_{tot}\ (X_nSi_m)$ is the total energy of the computation (super)cell, N_{units} the number of $X_n{+}Si_m$ atoms groups necessary to reproduce the crystal structure, μ_X the chemical potential of the metal in its reference state (usually crystal state), μ_{Si} the chemical potential of the metal in its reference state (diamond lattice). The chemical potential in the standard states thus coincide with the cohesion energy. The average formation energy per atom is then

$$E_{av}\ (X_nSi_m) = \frac{E_{form}\ (X_nSi_m)}{N_{units}(m+n)} \qquad (11)$$

In Fig. 32 the average formation energy for relevant Pt-Si phases extracted by The Materials Project (web page https://materialsproject.org) is shown and correlated with the relative crystal structures.

We then derive the first choice for the $J\{\theta_i(X)\}$ constants relative to the Si one with the following expression:

$$\frac{J\{\theta_i(X_nSi_m)\}}{J\{\theta_i(Si)\}} = \frac{\frac{m\,\mu_X + n\,\mu_{Si}}{m+n} + |E_{av}\,(X_nSi_m)|}{\mu_{Si}} \qquad (12)$$

These parameters are reported in Tabs. 14 and 15 for selected Pt-Si and Ni-Si phases, respectively.

Table 14: Phase dependent model parameters for the Pt-Si system. Ideal Si and Ideal Pt are the number of Si and Pt atoms in the cell in ideal conditions.

Phase	Ideal Si	Ideal Pt	$J\{\theta_i(X)\}$
Pt	0	12	1.0
Pt_2Si	4	8	1.2092
Pt_6Si_5	5	6	1.1886
PtSi	6	6	1.1771
Pt_2Si_3	6	4	1.1420
Si	8	0	1.0

Table 15: Phase dependent model parameters for the Ni-Si system. Ideal-Si and Ideal-Ni are the number of Si and Ni atoms in the cell in ideal conditions.

Phase	Ideal Si	Ideal Ni	$J\{\theta_i(X)\}/J\{\theta_i(Si)\}$
Ni	0	12	1.0
Ni_3Si	3	9	1.115
Ni_5Si_2	4	10	1.123
Ni_2Si	3	6	1.136
Ni_3Si_2	4	6	1.129
NiSi	6	6	1.124
$NiSi_2$	8	4	1.109
Si	8	0	1.0

We note that the approximation $J\{\theta_i(Ni,Pt)\} = J\{\theta_i(Si)\}$ is also assumed consistently with the choice of the use of the atomic formation energy $E_{av}\,(X_nSi_m)$ in Eq. 12.

In addition to the phase dependent parameters, the formalized model depends also on coordination and stoichiometry related parameters. To estimate these parameters, which strongly impact the (long) time evolution of the phase transformation, accurate *ab-initio* simulations are not feasible. In principle, they can be estimated with the aid of ad-hoc semi-empirical molecular dynamics simulations which could reproduce equivalent KMC settings in small systems and for a suitable (high) temperature range. However, the development of a semiempirical potential sufficiently accurate for all the phases of these complex binary system needs additional research effort beyond the scope of the MUNDFAB project. Modern Molecular

Dynamics methods based on Machine Learning potentials could be appropriate for such investigations and a preliminary activity has been initiated in this sense within the project. Anyhow, considering the current state of the research in this field only the experimental data can be used to validate the model. Here we will demonstrate the model feature using a standardized choice for the parameters while a result obtained with an experimentally validated choice of parameters will be reported in the next coming deliverables of WP6.

The key feature of the model is the stoichiometry control of the phase transition as clearly demonstrated by the sequence of Fig. 33 obtained with the "High C=>D" choice of the parameters in Tab. 16 and already reported in the D6.3.

Here, the simulation starts from a Ni nano-crystalline material, presenting ideal "cubic" grains of Ni with different orientations (indexes from 1 to 10) and a random distribution of diffusing Si atoms with the correct average density to reproduce the 3:1 (Ni:Si) stoichiometry. Fully periodic boundary conditions are imposed to simulate the bulk material. The system evolves toward the formation of a nanocrystalline stable phase with an averaged stoichiometry of 3:1, i.e., the Ni_3Si (orientation indexes from 11 to 20). This occurs after an initial reconfiguration of the Ni grains and the formation of a "quasi-amorphous" matrix around the nanograins described in the model by a mixing of different silicides.

Table 16: Two different extreme choices of stoichiometry and coordination related model parameters.

Parameter	Low C=>D	High C=>D
$R_{Cry-Diff}(\theta_i(X))$	$10^{-5}\omega$	$10^{-1}\omega$
$R_{Cry-Diff-bulk}(\theta_i(X))$	$10^{-4}\omega$	$10^{-1}\omega$
$R_{jump}(\theta_i(X))$	ω	ω
$R_{intermix}(\theta_i(X))$	ω	$10^{-4}\omega$
$k_{mix}(\theta_i(X))$	5.0	5.0
E_{s1}	$2.0 \times J/kT_{ann}$	$2.0 \times J/kT_{ann}$
E_{s1}	$2.0 \times J/kT_{ann}$	$2.0 \times J/kT_{ann}$
E_{coor}	$1.0 \times J/kT_{ann}$	$1.0 \times J/kT_{ann}$
$E_{CD_{Si}}$	$2.0 \times J/kT_{ann}$	$2.0 \times J/kT_{ann}$
$E_{CD_{Ni,Si}}$	$1.0 \times J/kT_{ann}$	$1.0 \times J/kT_{ann}$
E_{diff1}	$0.5 \times J/kT_{ann}$	$0.5 \times J/kT_{ann}$
E_{diff2}	$0.5 \times J/kT_{ann}$	$0.5 \times J/kT_{ann}$

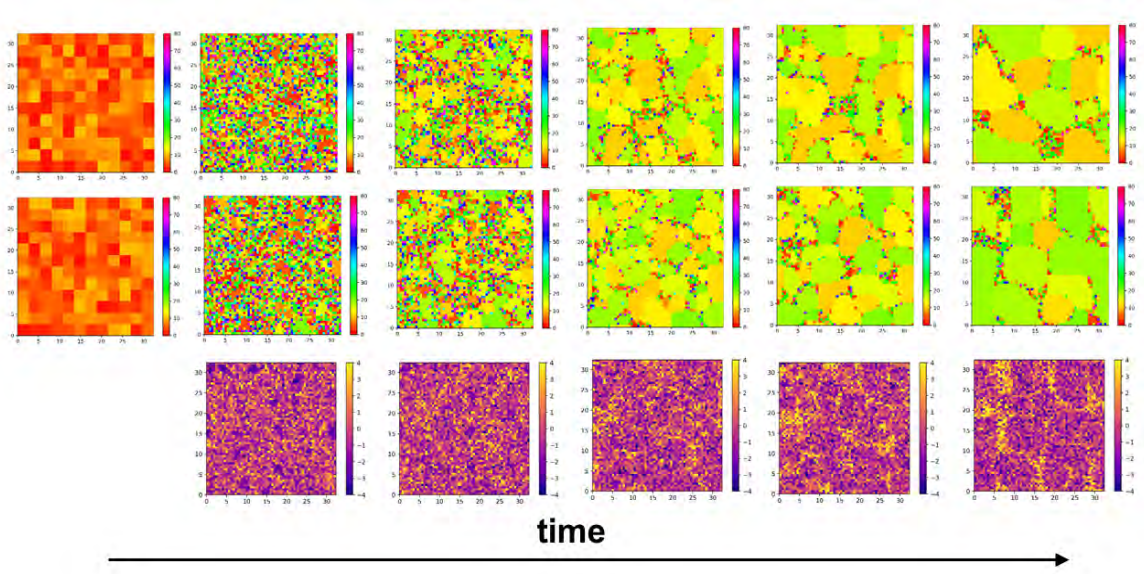

Figure 32: Snapshots of the Ni to Ni_3Si transition ("high C=>D" parameter choice in Tab. 16 and $J/kT_{ann} = 1.7$).The reaction occurs in a bulk volume prepared as an initial "ideal" nano-crystalline Ni material (cubic and equal sized nanograins) in a "wrong" 3:1 average stoichiometry (i.e., Ni_3Si) where all Si atoms are considered as diffusing. The system size is a cube of ~33x33x33 nm^3 with periodic boundary conditions. In the top and middle sequences, the grains cross sections along (100) and (010) directions at the simulation box center are shown. The phase transition from the Ni ideal grains (phase indexes 1-10) and $NiSi_3$ ones (phases indexes 11-20) is indicated by the color scale. The bottom row represents a deviation of the local correct stoichiometry of the Ni element in a section along the (010) direction at the simulation box center. This parameter is evaluated as the atomic deviation of the Ni element atoms with respect the number of atoms present in the conventional crystal cell of the corresponding phase (see corresponding color scale in the middle row sequence). ±4 atoms deviation is allowed in this calibration. We notice that this parameter tends to reach the 0 average value in the bulk of the grains although fluctuations are possible from cell to cell, while a clear average positive deviation is observed in the grain boundaries' regions.

This evolution mechanism is common to all the simulated phase transitions but of course the details depend on the parameter choice. The simulations obtained for the same setting of Fig. 33 but for "low C=>D" choice of the parameters is shown in Fig. 34. Apart from the general observation that the phase transition has the same qualitative trend for the two choices, we notice that in the "low C=>D" the intermediate stage shows a significant lower presence of the Si rich phases and a reduced level of the stoichiometry fluctuations in the nano grains bulk which tend to zero also locally for large evolution time.

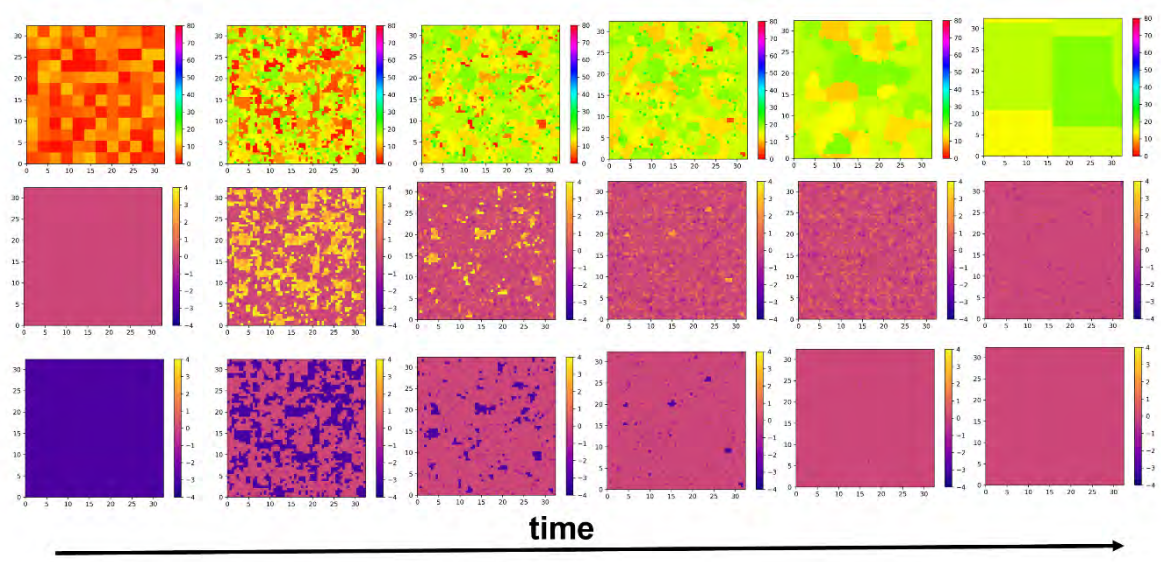

Figure 33: Snapshots of the Ni to Ni_3Si transition ("low C=>D" parameter choice in Tab. 16 and $J/kT_{ann} = 1.5$). The reaction occurs in a bulk volume prepared as an initial "ideal" nano-crystalline Ni material (cubic and equal sized nanograins) in a "wrong" 3:1 average stoichiometry (i.e., the Ni_3Si one) where all the Si atoms are considered as diffusing. The system size is a cube of about 33x33x33 nm^3 with periodic boundary conditions. In the top sequences the grains cross sections along (010) directions at the simulation box center are shown. The phase transition from the Ni ideal grains (phase indexes 1-10) and Ni_3Si ones (phases indexes 11-20) is indicated by the color scale. The middle and bottom row represent the deviation of the local correct stoichiometry of the Si and Ni element respectively in a section along the (010) direction at the simulation box center. This parameter is evaluated as the atomic deviation of the Si (Ni) element atoms with respect the number of atoms present in the conventional crystal cell of the corresponding phase (see corresponding color scale in the middle row sequence). ±4 atoms deviation is allowed in the calibration here used. We notice that this parameter tends to achieve the 0 local value at large time in the bulk of the grains for large time while deviations are observed in the grain boundaries' regions.

Of course, also the Si rich and other intermediate phases show similar evolution mechanism and as an example in Fig. 35 snapshots of the simulation for the Ni to $NiSi_2$ transition are shows for the "low C=>D" parameters set of Tab. 16. We have verified similar simulation features for all the transitions between phases with "adjacent" stoichiometries for the Ni-Si and Pt-Si binary system (results not shown).

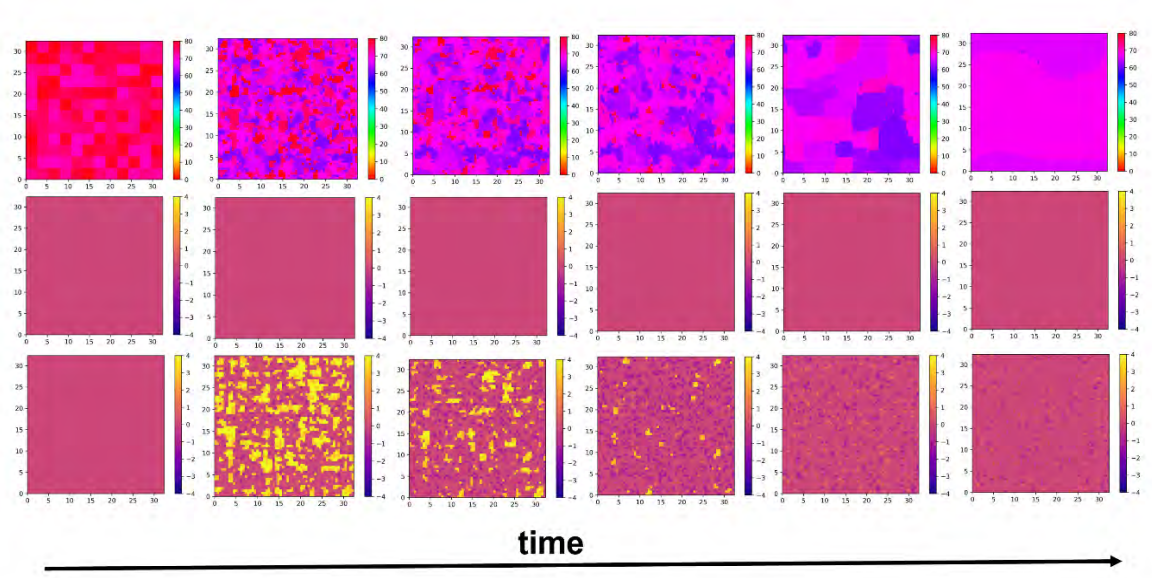

Figure 34: Snapshots of the Si to $NiSi_2$ transition ("low C=>D" parameter choice in Tab. 16 and $J/kT_{ann} = 1.5$). The reaction occurs in a bulk volume prepared as an initial "ideal" nano-crystalline Si material (cubic and equal sized nanograins) in a "wrong" 2:1 average stoichiometry (i.e., the Si one) where all the Ni atoms are considered as diffusing. The system size is a cube of about 33x33x33 nm^3 with periodic boundary conditions. In the top sequences the grains cross sections along the (010) directions at the simulation box center are shown. The phase transition from the Si ideal grains (phase indexes 71-80) and $NiSi_2$ ones (phases indexes 61-70) is indicated by the color scale. The middle and bottom row represent the deviation of the local correct stoichiometry of the Si and Ni element respectively in a section along the (010) direction at the simulation box center. This parameter is evaluated as the atomic deviation of the Si (Ni) element atoms with respect the number of atoms present in the conventional crystal cell of the corresponding phase (see corresponding color scale in the middle row sequence). ±4 atoms deviation is allowed in the calibration here used. We notice that this parameter tends to achieve the 0 local value at large time in the bulk of the grains for large time while deviations are observed in the grain boundaries' regions.

A remarkable model feature is the possibility to simulate the kinetics of the domain decomposition setting the simulation in a coexistence region of the phase diagram. In this sense the model represents an important upgrade with respect to the current state of the art in the field nucleation theory since these features have never been modelled within a Pott like framework and, more importantly, in a complex many phases system. An example of this kinetics is reported in the sequence of Fig. 36 where the initial system has been set as a Si material with a uniform density of diffusing Ni atoms for an intermediate average stoichiometry of 4:1 between the 2:1 of the Ni_2Si and the 1:0 of Si.

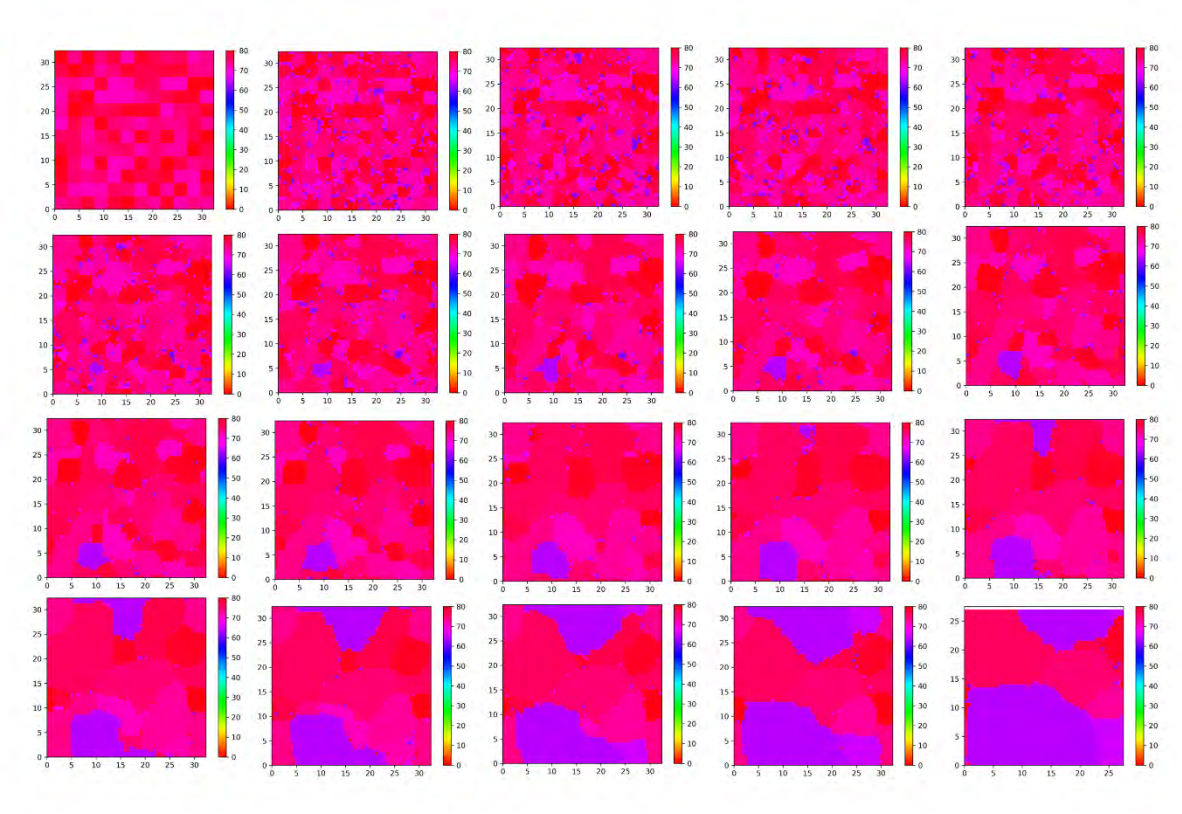

Figure 35: Snapshots of a domain decomposition evolution in the coexistence Si / $NiSi_2$ region ("low C=>D" parameter choice in Tab. 16 and $J/kT_{ann} = 1.5$). The reaction occurs in a bulk volume prepared as an initial "ideal" nano-crystalline Si material (cubic and equal sized nanograins) where Ni atoms are considered as diffusing. The system size is a cube of about 33 x 33 x 33 nm^3 with periodic boundary conditions. In sequence, the grains cross sections along (010) directions at the simulation box center are shown. The domain decomposition transition from the Si ideal grains (phase indexes 71-80) and a mix of Si and $NiSi_2$ ones (phases indexes 61-70) is indicated by the color scale. An average 50% - 50% of the two phases is expected.

4.3.1 Blanket systems

A deposited metal film on a Si substrate as an initial system is the conventional experimental setting for silicidation studies. The metal film structure assumes a nanocrystalline character after the deposition. Consequently, we decide to study the model features for ideal film/substrate configurations where the metal nano-crystalline material is initialized as ideal "cubic" grains with different orientations (indexes from 1 to 10 both for Ni and for Pt) on the Si substrate and the initial stoichiometries are the perfect ones for both Si and the metals. In Fig. 37 a snapshot of the simulation after about $9 \times 10^5 \omega^{-1} s$ for the Low C=>D setting and starting from ~10 nm Ni film on a Si substrate with a simulation box of about 86.5 x 86.5 x 86.5 nm^3 is shown as 3D view of the compound's layers and as (010) cross-sections of the compound and orientation indexes. Cross-sections of the Si and Ni stoichiometry deviation along the same direction are also shown.

A residual Ni film is present at this stage of the simulated evolution for the used calibration. Moreover, we also observe a mixture of different silicide phases from the Ni rich Ni_3Si to the NiSi and $NiSi_2$ ones at the Si interface. The intermixing role in the silicide formation is evident from analysis of the Ni and Si stoichiometry deviation shown in the same figure: the deviation is strong at the interface between the phases while it tends to zero in the inner region of the different layers.

In Fig. 38 snapshots of the evolution from the same initial system are shown for a high temperature case $J/kT_{ann} = 1.3$. In this case the absence of a residual Ni layer is evident at the later evolution stage, while the same considerations, already reported, are valid for the intermixing driven phase transformation kinetics.

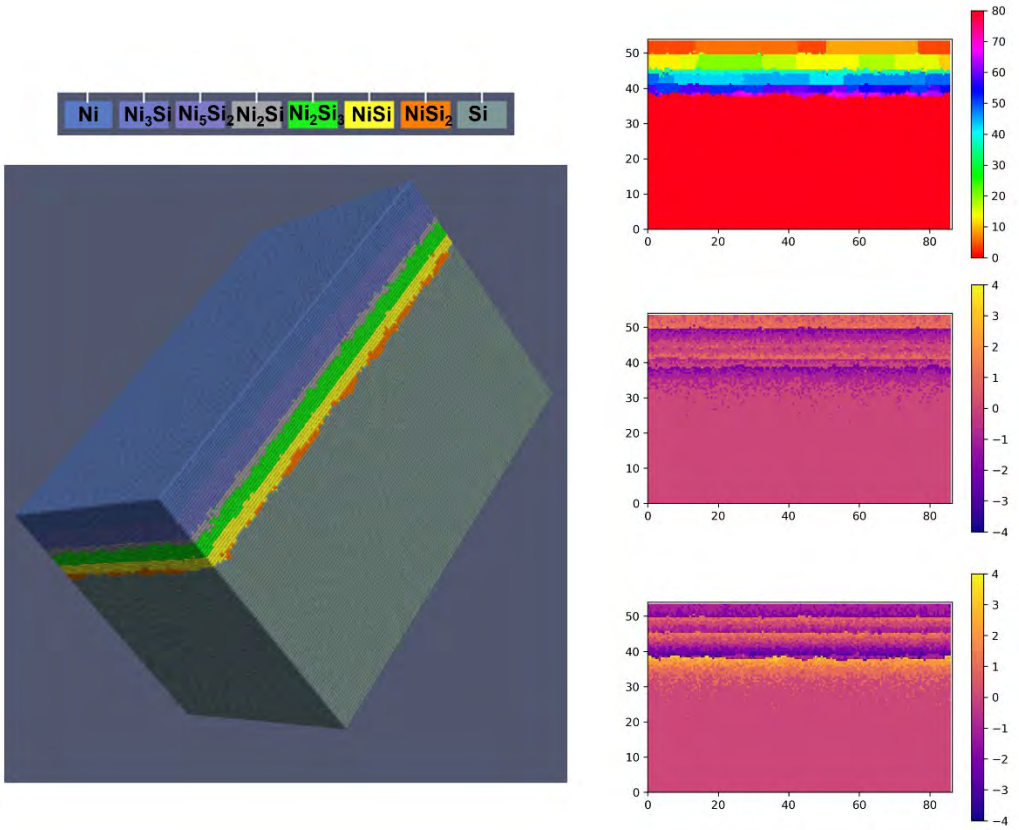

Figure 36: Left panel snapshot after about $9 \times 10^5 \omega^{-1} s$ ("low C=>D" parameter choice in Tab. 16 and $J/kT_{ann} = 1.5$) starting from ~10 nm "ideal" Ni nanocrystalline film on a Si substrate with a simulation box of about 86.5 x 86.5 x 54 nm^3 and lateral periodic boundary conditions. Compounds are indicated by the color scale Right column (010) cross section of the orientation index (top graph) and of the Si (middle graph) and Ni (bottom graph) deviation of the local correct stoichiometry.

As expected, the temperature has a huge impact in the silicidation speed, and the simulation comparisons (see snapshots at Fig. 39 for the increasing temperature $\mathrm{J/T_{ann}} = 2.0, 1.7, 1.5, 1.3$ at $\sim 1.1 \times 10^6\ \omega^{-1} s$) of isochronal annealing at different temperature in an approximate variation range of about 300 °C: very initial stage of the silicidation is obtained for the lowest temperature ($\mathrm{J/T_{ann}} = 2.0$) where only the Ni richest phase is visible at the interface with the Si substrate, while complete consumption of the metal layer is simulated for highest temperatures at the same time ($\mathrm{J/T_{ann}} = 1.3$) and intermediate situation for the intermediate temperature cases.

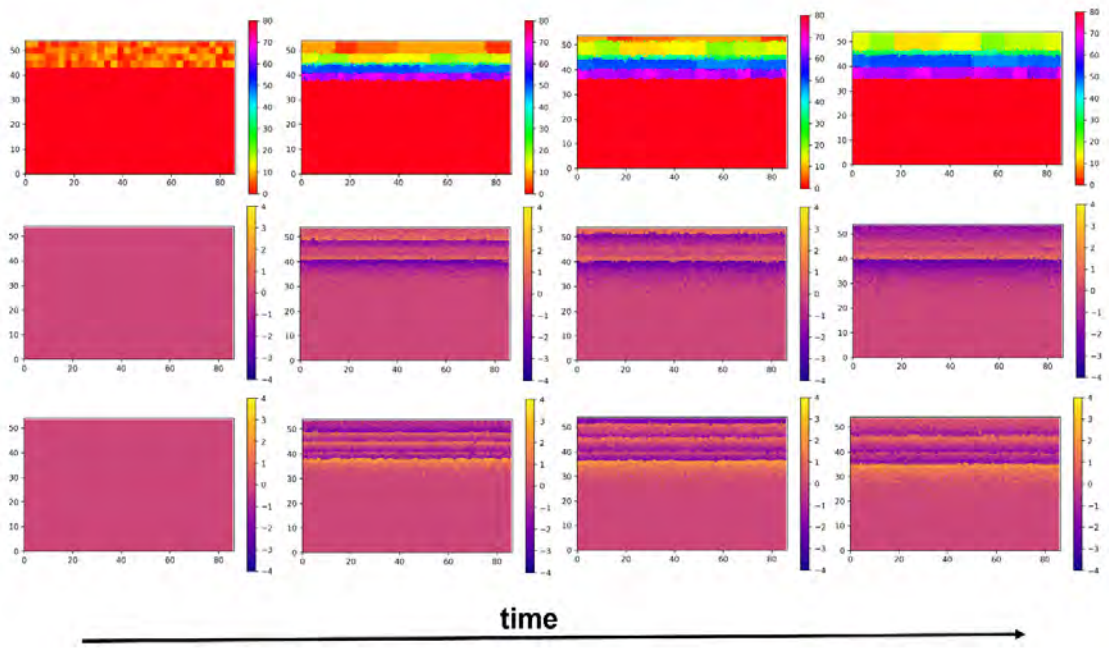

Figure 37: Snapshots in (010) cross section of the simulated evolution for the times $0. - 2.1 \times 10^5 -\ 4.1 \times 10^5\ and\ 6.6 \times 10^5\ \omega^{-1}s$ *("low C=>D" parameter choice in Tab. 16 and* $J/kT_{ann} = 1.3$*). The simulation starts from ~10 nm "ideal" Ni nanocrystalline film on a Si substrate with a simulation box of about 86.5 x 86.5 x 54 nm³ and lateral periodic boundary conditions. Orientation indexes are indicated by the color scale (top graphs). Moreover, the Si (middle graphs) and Ni (bottom graphs) deviations of the local correct stoichiometry are shown.*

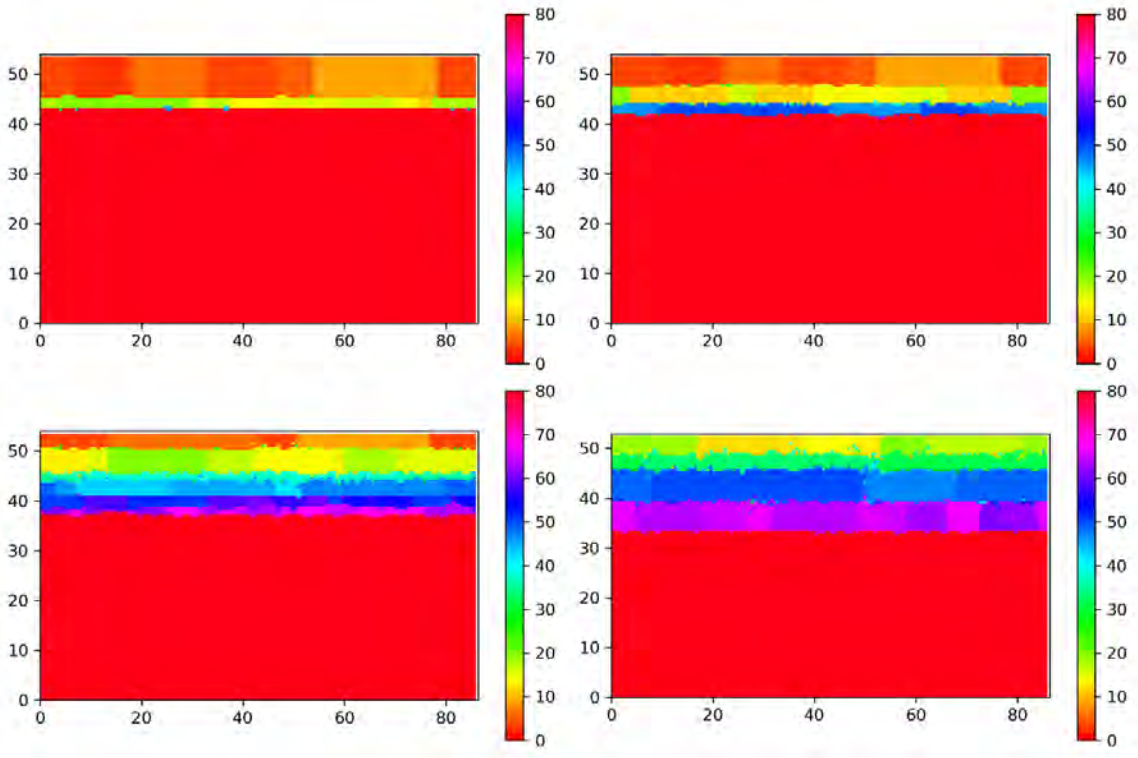

Figure 38: Snapshots in (010) cross section of the simulated evolution at different annealing temperature (increasing from left to right and from top to bottom) for similar simulated time $\sim 1.1 \times 10^6\ \omega^{-1}s$ *("low C=>D" parameter choice in Tab. 16 and* $J/T_{ann} = 2.0, 1.7, 1.5, 1.3$*). The simulation starts from ~10 nm "ideal" Ni nanocrystalline film on a Si substrate with a simulation box of about 86.5x86.5x54 nm³ and lateral periodic boundary conditions. Orientation indexes: 0-10 Ni, 11-20 Ni_3Si, 21-30 Ni_5Si_2, 31-40, Ni_2Si, 41-50 Ni_3Si_2, 51-60, NiSi, 61-70 $NiSi_2$, 71-80 Si.*

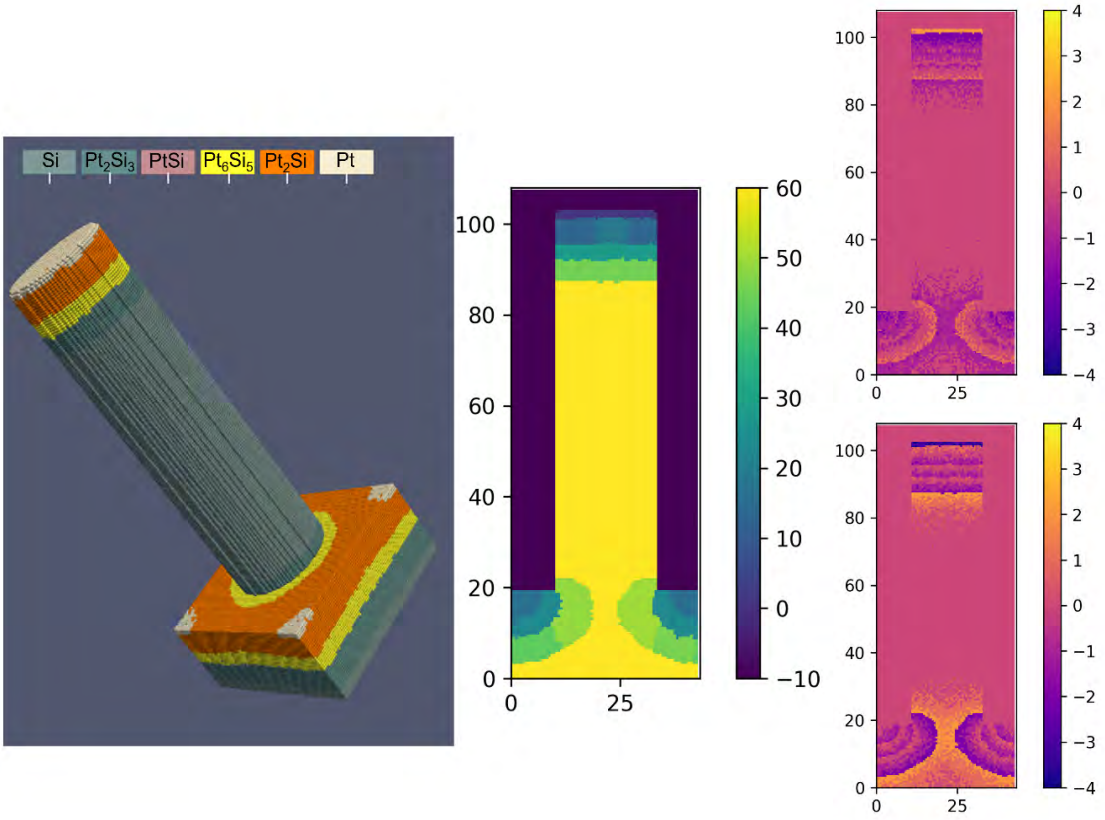

Figure 39: (left) Snapshot of the of Pt silicide (left hand graph where phases are indicated in the color-bar) process transition in a nanowire structure for a simulated where a limited residual of the Pt is observed $\sim 1.2 \times 10^6\ \omega^{-1} s$ *("low C=>D" parameter choice in Tab. 16 and* $J/T_{ann} = 1.5$*). The simulation box size is a cube of about 40x40x110 nm³ and lateral periodic boundary condition are assumed (i.e., the simulation reproduces a 2D distribution of nanowire with 40nm pitch). The blue region is air in the (010) cross section (central graph) and the orientation resolved phases distribution is show. Phases are indicated by indexes (0-10 Pt, 11-20 Pt_2Si, 21-30 Pt_6Si_5, 31-40, PtSi, 41-50 Pt_2Si_3, 51-60 Si). The right-hand graphs are cross-sectional planes of the deviations with respect to the local correct stoichiometry of the Si and Pt elements (Si top in (010) cross sections, Pt bottom in (010) cross sections).*

4.3.2 Nanowire systems

The implemented code can simulate 3D geometries, like the nanowire structure based on gate all around devices for which silicidation has a direct impact on the device characteristics. 3D simulation results for Ni silicide processing in nanowire geometry. A simulation example for the Pt silicide system is reported in Fig. 40 for $J/T_{ann} = 1.5$ "low C=>D" parameter choice and a time $\sim 1.2 \times 10^6\ \omega^{-1} s$ corresponding to an evolution stage characterized by a small residual layer of Pt on the top of the nanowire. The intermixing role in silicidation is qualitatively similar to the blanket sample geometry but the particular geometry constrains lead to the possibility of a different

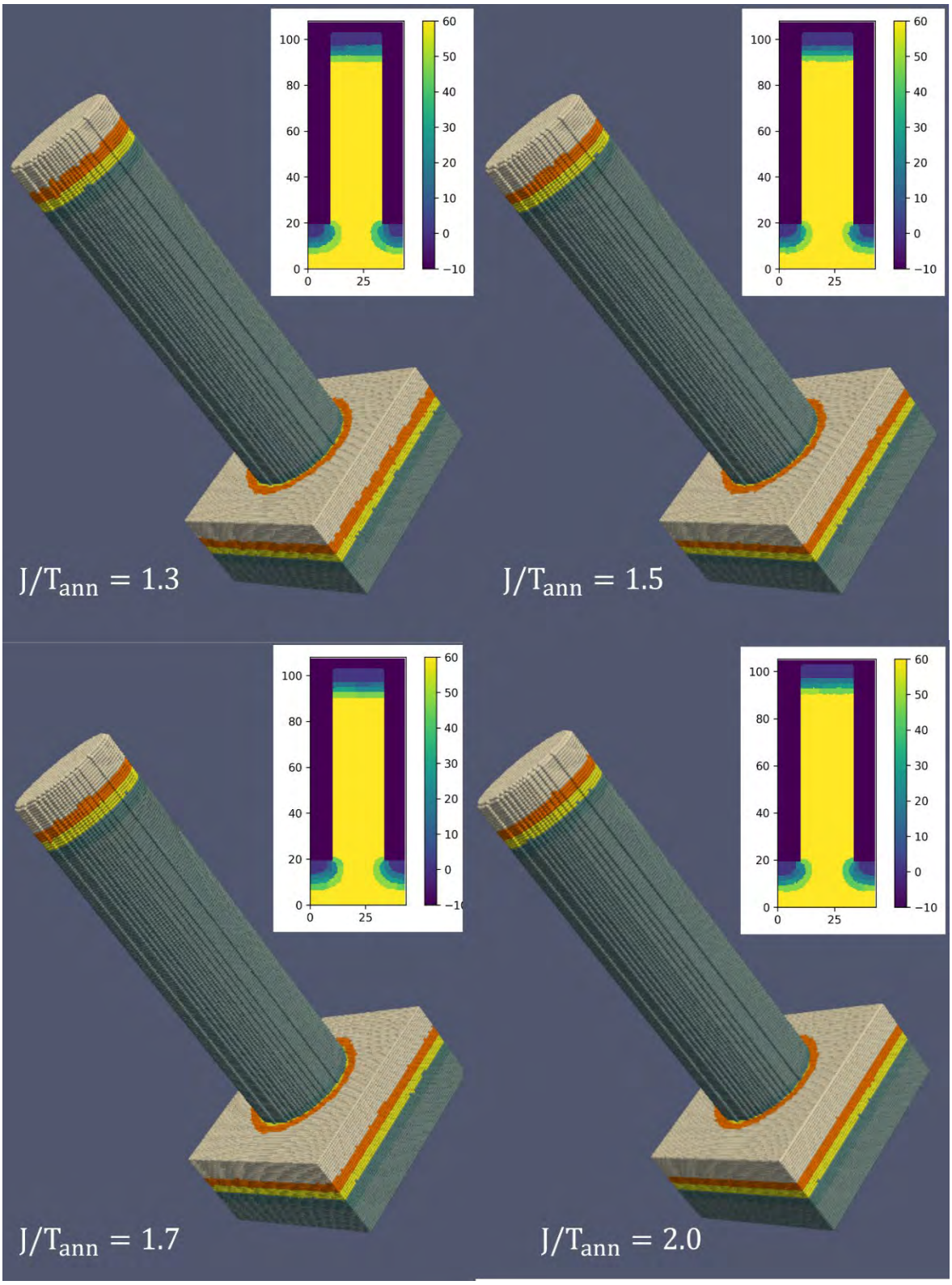

Figure 40: Snapshots of the of Pt silicide (phases are indicated in the color-bar) process transition for similar states of the silicidation obtained at different temperatures/times in a nanowire structure ("low C=>D" parameter choice in Tab. 16). They correspond to the temperature/time couples: $J/T_{ann} = 1.3$ - $t \sim 9.4 \times 10^4\ \omega^{-1}s$, $J/T_{ann} = 1.5$ - $t \sim 2.46 \times 10^5\ \omega^{-1}s$, $J/T_{ann} = 1.7$ - $t \sim 7.79 \times 10^5\ \omega^{-1}s$, $J/T_{ann} = 2.0$ - $t \sim 3.13 \times 10^6\ \omega^{-1}s$ *The simulation box size is a cube of about 40x40x110 nm³ and lateral periodic boundary conditions are assumed (i.e., the simulation reproduces a 2D distribution of nanowire with 40nm pitch). The blue region is air in the (010) cross section reported for each case and the orientation resolved phases distribution is shown. Phases are indicated by indexes (0-10 Pt, 11-20 Pt_2Si, 21-30 Pt_6Si_5, 31-40, PtSi, 41-50 Pt_2Si_3, 51-60 Si).*

effective stage of the silicidation (see e.g., the clearly different materials' distribution in the nanowire top region and the close to the substrate region). The analysis of the stoichiometry distribution indicates that these differences depend on the intermixing and diffusion evolution in constrained systems.

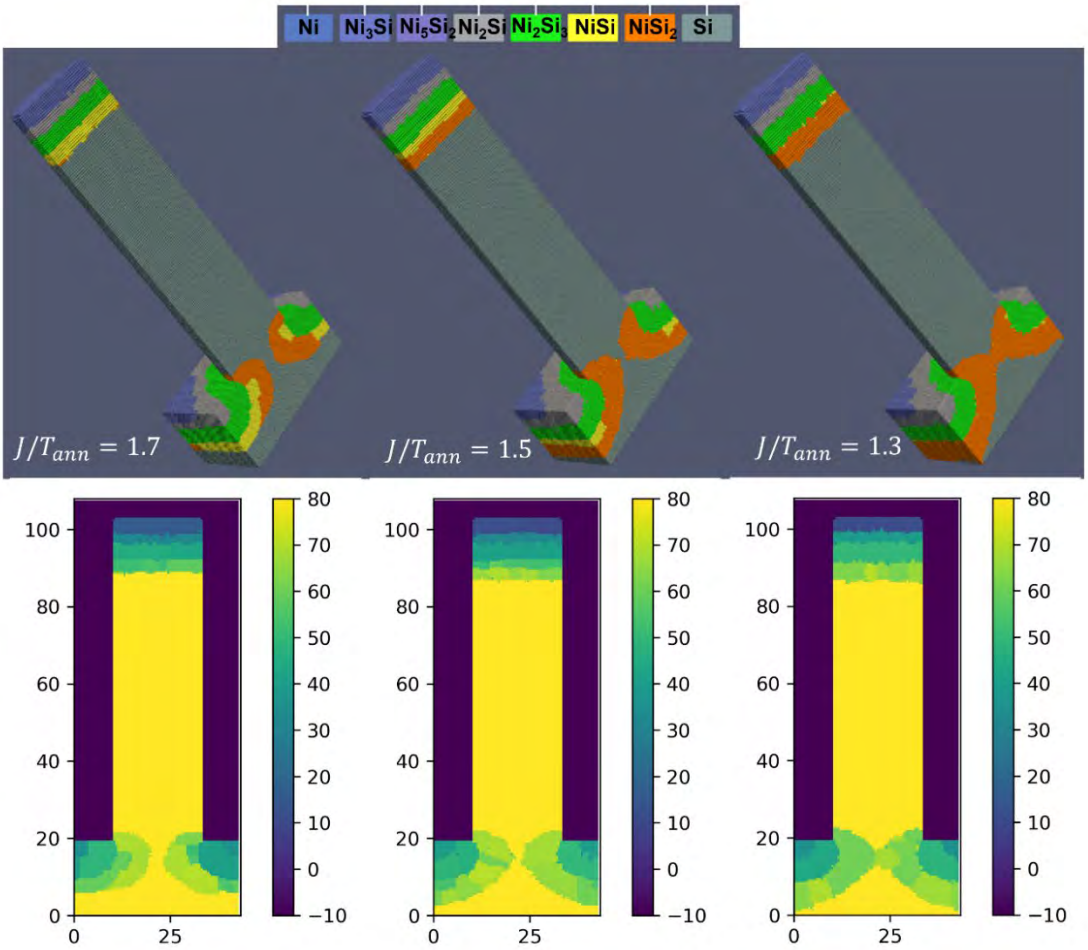

Figure 41: Snapshots of the of Ni silicide (phases are indicated in the color-bar) process transition for similar very advanced state of the silicidation obtained at different temperatures/times in a nanowire structure ("low C=>D" parameter choice in Tab. 16). They correspond to the temperature/time couples: $J/T_{ann} = 1.3$ - $t \sim 6.5 \times 10^5\ \omega^{-1}s$, $J/T_{ann} = 1.5$ - $t \sim 1.74 \times 10^6\ \omega^{-1}s$, $J/T_{ann} = 1.7$ - $t \sim 4.92 \times 10^6\ \omega^{-1}s$. The simulation box size is a cube of about 40x40x110 nm³ and lateral periodic boundary conditions are assumed (i.e., the simulation reproduces a 2D distribution of nanowire with 40nm pitch). The blue region is air in the (010) cross sections reported in the bottom row for each case and the orientation resolved phases distribution is shown. Phases are indicated by indexes (0-10 Ni, 11-20 Ni_3Si, 21-30 Ni_5Si_2, 31-40, Ni_2Si, 41-50 Ni_3Si_2, 51-60, NiSi, 61-70 $NiSi_2$, 71-80 Si)

An interesting analysis for the quantification of the temperature budget (temperature vs time relationship) can be inferred by means of the comparisons in Fig. 41 where a similar (intermediate) evolution stage is obtained for Pt kind of silicidation at different temperature/time couples where time spans almost two orders of magnitude for a temperature variation of about 300 °C range. A similar analysis is shown in Fig. 42. for the Ni silicide compounds for an advanced stage of the silicidation, where due to the formation of the Si rich phase and the relatively small size of the nanowire with respect to the initial film the silicide regions in the substrate merge. For these cases significant changes in the silicide/silicon interface profiles can be observed as dependent on temperature. Moreover, the compound distribution is also

strongly dependent on the reactive region (top nanowire versus substrate) and the temperature.

Conclusions

In this deliverable of WP2, the final models for heated implantation and silicidation were described in detail. We started with introducing several complementary measurements for heated implantations, including ultra-shallow depth profiling via the SIMS technique, SRP measurements for as-implanted samples, and Hall measurements for the P implanted samples. Here, we studied the laser annealing as an activation process on three different implantation conditions with different chuck temperature: room temperature, 150 °C, and 500 °C. For P implantation, as-implanted layers were amorphized for samples implanted at room temperature (P10) and 150 °C (P11), contrary to layers implanted at 500 °C (P12). Subsequent laser annealing, for all three layers, improved electrical properties in terms of activation when increasing the number of laser pulses (for a given energy density). In terms of reached maximum concentrations and activation rates, laser annealing on P10 and P11 layers show a clear advantage over P12, thanks to well-known SPER process, usually achieved by standard furnace annealing. In addition, SPER allows to generate low surface roughness, contrary to laser annealing on P12, which increasingly degrades the surface roughness. Also, for high thermal budget on P12, the formation of micrometer-long bracket-shaped defects occurs. To finalize our conclusion and push this study forward, further analysis is required for all three implantation conditions, either by extending actual laser annealing design of experiment, or by doing additional characterizations, particularly to identify found defects and evaluate their impact on each characteristic.

The results from these measurements were used to assess the accuracy of the AdvancedCalibration of the KMC method implemented in Sentaurus Process for simulation of heated implantations at implantation temperatures of 500 °C and below. For the dopants As, B, and P improvements on the existing models and calibrations were shown, that significantly increase the predictability of the KMC simulations. For As implantation, the UnsetAtomistic function had to be changed and a calibration regarding the interstitial clusters was performed. For B implantation, the relevant energies of B-I pairs had to be recalibrated, including their binding energy, migration energy and ionization energy to ensure that the effective diffusivity is conserved. Finally, for P implantation the procedure was similar as for B, but due to the importance of P-V pairs additional energies also had to be taken into account.

In the sections dedicated to the silicidation model we have presented the developed and implemented in-cell KMC model which can be generically applied to simulate the kinetics of binary metal-silicon nano systems. The application to the Pt and Ni silicide system is discussed as application example. The model implements in a suitable formalism all the physical features characterizing the silicidation evolution (namely domain decomposition character, intermixing and diffusion of element species, local stoichiometry variations). The results here presented should be considered as representative of the model intrinsic features and they can only be qualitatively related to the real system behavior. They are based on ad-hoc calibrations choices partially derived by ab-initio bulk energy calculations and two extreme cases for additional diffusion and intermixing related parameters. The simulated microstructural evolutions must be validated by experimental comparisons to assess further the calibration. As a general comment for the presented results, we can notice the excessive relevance of Si rich phases in the predicted silicide distribution. For the Pt silicides, this can be due to the inclusion of the

Pt_3Si_2 which is not present in the experimental phase diagram and for the Ni silicide, it can be due to an over-relative stability of the $NiSi_2$ with respect the NiSi one. In the future work in the evaluation of the model in the tool chain (D6.4) a calibration assessment will be considered.

References

[1] *Sentaurus Process User Guide, Version U-2022.12.*

[2] *Advanced Calibration for Process Simulation User Guide, Version U-2022.12.*

[3] K. Wittmaack, "High-sensitivity depth profiling of arsenic and phosphorus in silicon by means of SIMS," *Appl. Phys. Lett,* vol. 29, p. 552, 1976.

[4] H. Gnaser, "SIMS detection in the 10^12 atoms cm-3 range," *Surf. Interface Anal.,* vol. 25, pp. 173-176, 1997.

[5] K. Wittmaack and W. Wach, "Profile distortions and atomic mixing in SIMS analysis using oxygen primary ions," *Nucl. Instrum. Methods Phys. Res.,* vol. 191, pp. 327-334, 1981.

[6] W. Vandervorst, F. R. Shepherd and D. R. G., "High resolution SIMS and neutron depth profiling of boron through oxide–silicon interfaces," *J. Vac. Sci. Technol. A,* vol. 3, pp. 1318-1321, 1985.

[7] B. Gautier, J. Dupuy, B. Semmache and G. Prudon, "SIMS depth profile correction for the study of the first step of the diffusion of boron in silicon," *Nucl. Instrum. Methods Phys. Res. B,* vol. 142, pp. 361-376, 1998.

[8] J. B. Clegg, A. E. Morgan, H. A. M. d. Grefte, F. Simondet, A. Huber, G. Blackmore, M. G. Dowsett, D. E. Sykes, C. W. Magee and V. R. Deline, "A comparative study of SIMS depth profiling of boron in silicon," *Surf. Interface Anal.,* vol. 6, pp. 162-166, 1984.

[9] L. Shao, J. Liu, C. Wang, K. B. Ma, J. Zhang, J. Chen, D. Tang, S. Patel and W. K. Chu, "Response function during oxygen sputter profiling and its application to deconvolution of ultrashallow b depth profiles in Si," *Appl. Phys. Lett.,* vol. 83, pp. 5467-5469, 2003.

[10] A. Merkulov, P. Peres, S. Choi, F. Desse and M. Schuhmacher, "Advanced SIMS quantification in the first few nm of B, P and As ultrashallow implants," *Surf. Interface Anal.,* vol. 43, pp. 522-524, 2011.

[11] H. U. Ehrke, "Ultra Shallow Depth Profiling with SIMS," *Mater. Sci. Forum,* Vols. 573-574, pp. 197-205, 2008.

[12] A. Merkulov, P. Peres, K. Soulard, D. Larson and K. Sivaramakrishnan, "Improvement of extra low impact energy SIMS data reduction algorithm for process control," *J. Vac. Sci. Technol. B,* vol. 38, p. 053201, 2020.

[13] J. A. del Alamo and R. M. Swanson, "Measurement of Hall scattering factor in phosphorus-doped silicon," *J. Appl. Phys.,* vol. 57, p. 2314–2317, 1985.

[14] N. Zographos, C. Zechner and I. & Avci, "Efficient TCAD model for the evolution of interstitial clusters,{311} defects, and dislocation loops in silicon," *MRS Online Proceedings Library (OPL),* vol. 994, pp. 0994-F10, 2007.

[15] N. E. B. Cowern, G. Mannino, P. A. Stolk, F. Roozeboom, H. G. A. Huizing, J. G. M. van Berkum, F. Cristiano, A. Claverie and M. Jaraíz, "Energetics of self-interstitial clusters in Si," *Phys. Rev. Lett.,* vol. 82, p. 4460, 1999.

[16] I. Martin-Bragado, I. Avci, N. Zographos, M. Jaraiz and P. Castrillo, "From point defects to dislocation loops: A comprehensive modelling framework for self-interstitial defects in silicon," *Solid-state electronics,* vol. 52, pp. 1430-1436, 2008.

[17] N. Arai, S. Takeda and M. Kohyama, "Self-interstitial clustering in crystalline silicon," *Phys. Rev. Lett. ,* vol. 78, p. 4265, 1997.

[18] L. A. Marques, M. Aboy, M. Ruiz, I. Santos, P. Lopez and L. Pelaz, "{001} loops in silicon unraveled," *Acta Materialia,* vol. 166, pp. 192-201, 2019.

[19] S. Lee and G. S. Hwang, "Growth and shape transition of small silicon self-interstitial clusters," *Phys. Rev. B,* vol. 78, p. 045204, 2008.

[20] I. Martin-Bragado, P. Castrillo, M. Jaraiz, R. Pinacho, J. E. Rubio and J. Barbolla, "Physical atomistic kinetic Monte Carlo modeling," *Phys. Rev. B,* vol. 72, p. 035202, 2005.

[21] G. Fisicaro, L. Pelaz, A. M. P. Lopez, M. Italia, K. Huet, F. Cristiano, Z. Essa, Q. Yang, E. Bedel-Pereira, M. Quillec and A. La Magna, "Kinetic Monte Carlo simulations of boron activation in implanted Si under laser thermal annealing," *Appl. Phys. Express,* vol. 7, p. 021301, 2014.

[22] I. Martin-Bragado and V. Moroz, "Facet Formation during Solid Phase Epitaxy Regrowth: A Lattice Kinetic Monte Carlo Model," *Appl. Phys. Lett.,* vol. 95, p. 123123, 2009.

[23] B. Sklenard, B. J.-C., P. Batude, P. Rivallin, C. Tavernier, S. Cristoloveanu and I. Martin-Bragado, " An Atomistic Investigation of the Impact of In-Plane Uniaxial Stress during Solid Phase Epitaxial Regrowth," *Appl. Phys. Lett. ,* vol. 102, p. 151907, 2013.

[24] I. Martin-Bragado and B. Sklenard, "Understanding Si(111) Solid Phase Epitaxial Regrowth Using Monte Carlo Modeling: Bi-Modal Growth, Defect Formation, and Interface Topology," *J. Appl. Phys.,* vol. 112, p. 024327, 2012.

[25] N. Zographos and I. Martin-Bragado, "A Comprehensive Atomistic Kinetic Monte Carlo Model for Amorphization/Recrystallization and Its Effects on Dopants," *MRS Online Proceedings Library,* vol. 1070, p. 10700301, 2008.

[26] Y. Du and J. Schuster, "Experimental Investigations and Thermodynamic Descriptions of the Ni-Si and C-Ni-Si Systems," *Metallurgical and Materials Transactions A,* vol. 30, p. 2409, 1999.

[27] A. Ullah, Ubaidullah, M. Khan, X. Weihua, S. Hussain, M. ur Rahman, S. N. and F. Haq, "Simulations of grain growth in realistic 3D polycrystalline microstructures and the MacPherson–Srolovitz equation," *Mater. Res. Express,* vol. 4, p. 066502, 2017.

[28] Y. J. Kim, S. K. Hwang, M. H. Kim, S. I. Kwun and S. W. Chae, "Three-dimensional Monte-Carlo simulation of grain growth using triangular lattice," *Materials Science and Engineering A,* vol. 408, p. 110, 2005.

[29] M. N. Rosenbluth, "Genesis of the Monte Carlo Algorithm for Statistical Mechanics," *AIP Conference Proceedings,* vol. 690, pp. 22-30, 2003.